

QUANTIFYING AND REDUCING UNCERTAINTY IN LARGE VOLUME  
REMOTE SENSING MEASUREMENTS OF ATMOSPHERIC BOUNDARY  
LAYER FLOWS

A Dissertation

Presented to the Faculty of the Graduate School  
of Cornell University

In Partial Fulfillment of the Requirements for the Degree of  
Doctor of Philosophy

by

Hui Wang

May 2016

© 2016 Hui Wang

QUANTIFYING AND REDUCING UNCERTAINTY IN LARGE VOLUME  
REMOTE SENSING MEASUREMENTS OF ATMOSPHERIC BOUNDARY  
LAYER FLOWS

Hui Wang, Ph.D.

Cornell University 2016

Doppler wind lidars are capable of measuring multi-scale turbulent flows in the atmospheric boundary layer. With proper scanning geometries and wind retrieval algorithms, lidar measurements provide robust estimates of time-evolving three-dimensional mean flow and turbulence fields. This dissertation focuses on uncertainty quantification and reduction of (i) mean wind velocity, (ii) turbulence statistics and (iii) wind turbine wake characteristics derived from lidar measurements. To reduce the uncertainty in mean wind velocity measurements from lidar arc scans, a model is developed and verified for uncertainty prediction. Both observations and model predictions show that the uncertainty is proportional to turbulence intensity and is reduced by aligning arc scans with wind directions and using large arc spans with large azimuth intervals. The limitations of lidar turbulence measurements are evaluated through a field experiment and statistical simulations, both of which show that the volumetric averaging of lidar measurements inflates the autocorrelation of lidar radial velocity and consequently causes large errors in the estimated radial velocity variance. It is further shown that, given atmospheric flows are commonly stationary for no more than one hour, the systematic error is negligible but the random error has about 8%

uncertainty, imposing a limit on the accuracy of current lidar turbulence measurements. Uncertainties in lidar wake characterization are evaluated through a field experiment. A wake detection algorithm is developed to retrieve wake characteristics from small sector scans. Because the wake moves as the wind turbine yaws, lidar measurement locations relative to the wake change with wind direction. This change introduces large uncertainties in the retrieved wake characteristics, especially when vertical wind shear is large or wind directions are nearly orthogonal to the laser beams. By focusing on uncertainty reduction in three aspects of lidar applications of wind measurements, this dissertation demonstrates that with careful scan design and data processing and by accounting for site conditions, it is possible to model, quantify and minimize both the systematic and random errors in lidar-derived wind velocities.

## BIOGRAPHICAL SKETCH

Hui Wang was born on April 17, 1981 in Huangyan, China. He graduated from Northwestern Polytechnical University with a B.S. in Environmental Science in 2003 and a M.S. in Environmental Engineering in 2006. In 2010, he joined Prof. Barthelmie's lab to pursue research in wind energy at Indiana University from where he received a M.S. in Atmospheric Science. He transferred to Cornell University in 2014. Prior to beginning graduate school he worked as a mechanical engineer and sales engineer in the emerging Chinese wind energy industry.

*To my wife Erin and my family for their constant support and unconditional love*

## ACKNOWLEDGMENTS

First and foremost, I would like to express my deepest gratitude to my academic advisor, Prof. Rebecca Barthelmie, for her six years of guidance, patience and encouragement. Thank you for giving intellectual freedom in my work, supporting my attendance of various conferences and training programs, engaging me in field experiments, and arranging my summer internships. For everything you have done for me, Prof. Barthelmie, thank you. I am also indebted to Prof. Sara Pryor for her contribution of time and ideas that has made this dissertation possible. I would also like to thank Prof. Zellman Warhaft for serving as my committee member and sharing his knowledge with me.

My sincere appreciation also goes to my collaborators Dr. Andy Clifton at National Renewable Energy Laboratory who helped complete my first field experiment and Gareth Brown at SgurrEnergy who allowed me to access industrial data for my research. I am grateful to all of my lab mates over the years, including Paula Doubrava, Ryan Sullivan, Mark Belding, Tim Wright, Dr. Paola Crippa, and Dr. Craig Smith. Thanks for bringing fun and encouragement, especially during the tough times.

I would like to thank the Sibley School of Mechanical Engineering at Cornell University and the Department of Geological Sciences at Indiana University for their immeasurable support. In particular, I would like to thank Prof. Kaj Johnson at Indiana University for his time and advice when serving as my committee member.

Funding for this research was provided by the National Science Foundation (award No. 1464383) and the Department of Energy (award No. DE-EE0005379).

## TABLE OF CONTENT

CHAPTER 1	MOTIVATION AND INTRODUCTION .....	1
1.1	Doppler Wind Lidar.....	2
1.2	Lidar Applications to Flow Characterization in the Atmosphere .....	7
1.3	Lidar Applications in Wind Energy.....	9
1.4	Research Questions.....	11
1.5	Outline .....	13
CHAPTER 2	WIND MEASUREMENTS FROM ARC SCANS WITH DOPPLER WIND LIDAR	16
2.1	Introduction.....	16
2.2	Experimental Setup.....	20
2.3	Wind Retrieval Method .....	24
2.4	Results and Discussion .....	32
2.5	Mean Wind Direction .....	42
2.6	Vertical Profile of the Horizontal Wind Speed.....	42
2.7	Practical Issues and Guidelines for Arc Scans.....	44
2.8	Conclusions.....	48
2.9	Appendix.....	49
CHAPTER 3	LIDAR ARC SCAN UNCERTAINTY REDUCTION THROUGH SCANNING GEOMETRY OPTIMIZATION.....	55
3.1	Introduction.....	55
3.2	Uncertainty in the Lidar Radial Velocity.....	57
3.3	Uncertainty in Wind Speeds Derived from Lidar Arc Scan Measurements ..	60
3.4	Uncertainty Computed from an Isotropic Turbulence Model .....	64
3.5	Observed Arc Scan Uncertainty .....	70
3.6	Discussion.....	79
3.7	Implication for Applications in Wind Energy .....	81
3.8	Conclusions.....	83
3.9	Appendix A: Atmospheric Boundary Layer Turbulence Characteristics .....	84
3.10	Appendix B: Wind Speed and Direction Probability Distributions.....	87
CHAPTER 4	ERRORS IN RADIAL VELOCITY VARIANCE FROM DOPPLER WIND LIDAR	88
4.1	Motivations and approach.....	88
4.2	Preliminaries .....	89

4.3	Errors in radial velocity variance.....	92
4.4	Errors from observations .....	98
4.5	Discussions .....	107
4.6	Conclusion remarks .....	113
<b>CHAPTER 5 WIND TURBINE WAKE DETECTION WITH A SINGLE DOPPLER WIND LIDAR .....</b>		<b>115</b>
5.1	Introduction.....	115
5.2	Lidar basics .....	116
5.3	Experiment setup .....	117
5.4	Wake profile estimation algorithm .....	118
5.5	Results and discussions.....	123
5.6	Conclusions.....	130
<b>CHAPTER 6 SUMMARY AND FUTURE WORK .....</b>		<b>132</b>
6.1	Summary.....	132
6.2	Future work.....	135
<b>BIBLIOGRAPHY .....</b>		<b>138</b>

## LIST OF FIGURES

Figure 1.1 Schematic of lidar Range Height Indicator (RHI) scan geometry .....	4
Figure 1.2 Schematic of lidar Plan Position Indicator (PPI) scan geometry .....	5
Figure 1.3 Schematic of lidar Velocity Azimuth Display (VAD) scan geometry .....	5
Figure 2.1 Flow diagram of lidar scanning geometries and their applications in studying flow characteristics in the Atmospheric Boundary Layer (ABL) and facilitating wind energy development. ....	17
Figure 2.2 (a) Layout of the test site at the NWTC. The Galion lidar location is denoted by the red square, and the M5 is denoted by the red circle. The distance between the lidar and M5 is approximately 150 m. The location of the lidar range gates are depicted by the circular grids between M5 and the Galion. (b) The inset shows the topography surrounding the site. The interval of the overlaid elevation contour lines (white) is 50 m. The radius of the dark circle is 3.7 km, within which uniform terrain is required for horizontally homogeneous flow (Wyngaard 2010). (c) The inset shows the wind speed spatial distribution simulated by WASP Engineering and the elevation contour lines (white lines and 10-m interval) derived from Shuttle Radar Topography Mission elevation data. This WASP Engineering simulation is based on a wind speed of 9 m s <sup>-1</sup> and a wind direction of 272° at a height of 74 m at the location of M5. ....	21
Figure 2.3 (a) The modeled root mean square error (RMSE) of the retrieved wind velocity with and without vertical wind speed according to Eq. (2.A12) in the Appendix, and (b) the expected value of bias $\beta$ in $u_0$ and $v_0$ introduced by assuming $w_0 = 1.0 \text{ m s}^{-1}$ and elevation angle = 12.7° according to (2.14). In (a), wind components $u$ , $v$ and $w$ are assumed to be independent and have the same variance $1.0 \text{ m}^2 \text{ s}^{-2}$ . The first line of sight of the azimuth range was at $\theta = 0^\circ$ . ....	27
Figure 2.4 Outlier detection of lidar radial velocity ( $v_R$ ) based on Eq. (2.17) for a 10-minute time series measured at range gate 11 and azimuth angle 75.8°. The dashed lines are the outlier bounds beyond which measurements are treated as outliers. In this case, the outlier (the 3rd measurement) has a high SNR, but is identified as an outlier per Eq. (2.17). ....	29
Figure 2.5 Spike detection of lidar radial velocity ( $v_R$ ) based on the radial velocity difference between the two neighboring measurements ( $v_{R,i+1} - v_{R,i}$ ) for a 10-minute time series. Measurements were taken at range gate 11 and an azimuth angle of 75.8°. As defined in Eq. (2.18), a spike is detected if $ v_{R,i+1} - v_{R,i}  > 2\text{IQR}\Delta$ as shown by the dashed lines. Also, different signs for two adjacent points are required to confirm a spike. In this case, the difference between data point 8 and 9 and the difference between data point 9 and 10 were outside of the dashed lines, and they have different signs. Therefore, data point 9 was identified as a spike. ....	29

- Figure 2.6 Relationship between the 10-min mean wind speed from the sonic anemometer ( $V_{sonic}$ ) at 74 m height on M5 in the free stream sector ( $210^{\circ}$ – $360^{\circ}$ ) and lidar range gate 11 ( $V_{lidar}$ ). Lidar data with high cond numbers of the model matrix  $[K(\mathbf{G})]$  are marked with red dots, low  $R^2$  of the WLS fits are shown by the blue squares, and estimates derived using data with a high number of missing measurements at some azimuth angles are shown as dark diamonds. .... 34
- Figure 2.7 Relationship between the squared lidar wind speed error  $[(e_{abs})^2]$  at range gate 11 and the TKE derived from the sonic anemometer at 74 m height on M5. The medians and 25<sup>th</sup> and 75<sup>th</sup> percentiles were calculated for 12 TKE bins that had the same sample number in each bin. .... 35
- Figure 2.8 Boxplots of relative errors ( $e_{rv}$ ) of all retrieved lidar wind speeds grouped according to the number ( $N_d$ ) of measured mean radial velocity that was significantly different from the radial velocity estimated from sonic measurements. If the difference between the mean radial velocity from the lidar and the sonic showed a significant linear relationship with the azimuth angle, the respective data point was marked by a dark circle. The linear relationship was significant if the fitted slope was significantly nonzero ( $p$ -value  $\leq 0.01$ ) and larger than the 90<sup>th</sup> percentile of all the fitted slopes. .... 38
- Figure 2.9 A case study showing a comparison between the 10-min mean radial velocities ( $v_R$ ) measured by the lidar (solid circles) and estimated from the sonic measurements (thick gray line) for a range of azimuth angles with an elevation angle =  $12.7^{\circ}$ . The sonic mean wind speed =  $7.13 \text{ m s}^{-1}$ , and the wind direction =  $257^{\circ}$ . The gray dashed lines show the 95% confidence interval for the radial velocity estimated from the sonic based on the turbulence statistics derived from sonic measurements. Lidar measurements fit Eq. (2.5) very well (as shown by the dark line), but the estimated wind speed ( $8.69 \text{ m s}^{-1}$ ) overestimates the sonic wind speed by 22%. .... 38
- Figure 2.10 Relationship between 10-min mean values of TKE derived from the sonic measurements and the radial velocity variance ( $\langle v_R'^2 \rangle$ ) from the lidar measurements. Also shown are linear fits to these data with and without intercept. .... 40
- Figure 2.11 Relationship between the sonic mean wind speed ( $V_{sonic}$ ) and the lidar mean wind speed ( $V_{lidar}$ ) for the data from Figure 2.6 with (a)  $\langle v_R'^2 \rangle \leq 2.3 \text{ m}^2 \text{ s}^{-2}$  and (b)  $\sigma_v \leq 0.38 \text{ m s}^{-1}$ , which excluded data with the top 30% of high  $\langle v_R'^2 \rangle$  and  $\sigma_v$ , respectively. .... 40
- Figure 2.12 Comparison of the lidar mean wind speed ( $V_{lidar}$ ) and the sonic mean wind speed ( $V_{sonic}$ ) in four wind direction sectors:  $210^{\circ}$ – $270^{\circ}$ ,  $270^{\circ}$ – $300^{\circ}$ ,  $300^{\circ}$ – $330^{\circ}$ , and  $330^{\circ}$ – $360^{\circ}$ . Data presented here are the same as those presented in Figure 2.6. The wind speed measurements are shown in rank order of the lidar mean wind speed. The 95% confidence interval of the lidar mean wind speed is based on the standard error ( $\sigma_v$ ) calculated using Eq. (2.19). .... 41

- Figure 2.13 Relationship between the 10-min mean wind direction from the lidar range gate 11 ( $D_{lidar}$ ) and sonic anemometer ( $D_{sonic}$ ) at 74 m height on M5 in the free stream sector ( $210^\circ$ – $360^\circ$ ). A value of  $360^\circ$  was added to wind directions from the lidar that are lower than  $90^\circ$  to avoid direction ambiguity around  $0^\circ/360^\circ$ . ..... 42
- Figure 2.14 Mean vertical profiles of the 10-min mean wind speed retrieved from the lidar and measured by the cup anemometers on M5 for wind direction sector (a)  $210^\circ$ – $330^\circ$  and (b)  $330^\circ$ – $360^\circ$ . Only wind speeds of 4–12 m s<sup>-1</sup> as measured by the cup anemometer at 80 m height were included. Wind direction was defined by measurements from the sonic measurement at 74 m height. Standard errors of the mean values for the lidar profiles and the cup profiles are plotted as error bars and shaded areas, respectively. .... 44
- Figure 2.15 Uncertainty in the retrieved wind speed from arc scans as a function of the arc scan azimuth range ( $\theta_s$ ) and the azimuth interval ( $\Delta\theta$ ). The number of beams  $N_\theta = 1 + \theta_s/\Delta\theta$ . Uncertainty is measured by  $\sigma_{se}/\sigma_h$ , where  $\sigma_{se}^2 = \sigma_{u_0}^2 + \sigma_{v_0}^2$  as defined in Eq. (2.19) and  $\sigma_h^2 = \langle u'^2 \rangle + \langle v'^2 \rangle$ . The method used in this analysis is from Banakh et al. (1995) and is described in Eq. (2.A3). Turbulence was assumed to be isotropic, and the turbulence spatial correlation was assumed to decay exponentially. The error in the radial velocity was set to zero by assuming a high return intensity. Wind speed = 8 m s<sup>-1</sup>. Wind direction =  $270^\circ$ . The horizontal wind speed standard deviation = 1.414 m s<sup>-1</sup> as  $\langle u'^2 \rangle = \langle v'^2 \rangle = 1 \text{ m}^2 \text{ s}^{-2}$ . The turbulence length scale = 400 m. .... 47
- Figure 3.1 The relationship between the signal-to-noise ratio (SNR) and the radial velocity random error variance ( $\sigma_e^2$ ). The gray dots show the observed radial velocity variance approximated by the difference between the variance and the autocovariance at one time lag of the radial velocities collected in an experiment in which the lidar was operated with a staring mode at the US National Renewable Energy Laboratory (Wang et al. 2015b), and the observed Cramer–Rao Bound (CRB) (filled dark circles) is approximated by the mean of the lowest 5% of the gray dots (Frehlich 2001). The empirical relationship between the SNR and the CRB is denoted by the dark solid line and is based on Eq. (5) in Pearson and Collier (1999). ..... 59
- Figure 3.2 An example of the spatial distribution of air parcels sampled in two consecutive arc scans by a lidar at range distance  $s = 315 \text{ m}$  for four different wind directions (westerly, easterly, northerly, and easterly) under the following assumptions: (1) frozen turbulence, (2) the lidar is located at the origin (the dark triangle) scanning from  $\theta = 75^\circ$  to  $105^\circ$  with  $5^\circ$  increments with elevation angle  $\phi = 17^\circ$ , (3) the mean wind speed is 7 m s<sup>-1</sup> and (4) the sampling interval is 3 sec. .... 62
- Figure 3.3 Dependence of the relative standard error ( $\epsilon_l$ ) of wind speed estimated from arc scans on (a) turbulence intensity (TI) and (b) wind speed ( $V_0$ ) and direction (expressed as the relative direction ( $\beta$ )) based on the isotropic turbulence model given in Eq. (3.10) for the following scan geometry:  $\phi = 16.7^\circ$ ,  $\Delta\theta = 30^\circ$ ,  $\delta\theta = 6^\circ$

and  $r = 313$  m. The Coriolis parameter  $f_0 = 0.0001 \text{ m s}^{-1}$ . ..... 69

Figure 3.4 Dependence of relative standard error ( $\epsilon_l$ ) of wind speed ( $V_0$ ) on arc span ( $\Delta\theta$ ) and beam number per arc scan for relative directions (a)  $\beta = 0^\circ$ , (b)  $\beta = +45^\circ$ , (c)  $\beta = +90^\circ$ , and (d)  $\beta = -90^\circ$  with  $\phi = 16.7^\circ$  and  $r = 313$  m. The results are calculated for  $V_0 = 7 \text{ m s}^{-1}$  and  $\text{TI} = 12\%$  over a 10 minute period. The Coriolis parameter  $f_0 = 0.0001 \text{ s}^{-1}$ . The contour interval is 0.2%. ..... 70

Figure 3.5 Plan views of the scanning geometries used at (a) site A, (b) site B and (c) Site C. The dark squares indicate the lidar locations, and the hatched areas indicate the wind direction sectors without flow distortions. Locations of meteorological masts are denoted by the solid gray circles. The elevation angle ( $\phi$ ) and the arc span ( $\Delta\theta$ ) used at each of the sites are also given. .... 72

Figure 3.6 Variation of the standard error (RSE) with the relative direction ( $\beta$ ) at Site A at 80 m height in (a, c and e) and 60 m height in (b, d and f). The RSE is given in (e and f) for the 95% confidence interval of the observed difference between the cup and lidar measurements ( $\hat{\epsilon}_d$ ), the predicted difference between the cup and lidar measurements ( $\epsilon_d$ ), the predicted cup error ( $\epsilon_c$ ), and the predicted lidar error ( $\epsilon_l$ ). The input for the RSE predictions include the mean wind speed ( $V_0$ ) shown in (c and d) and the mean wind speed variance ( $\sigma_u^2$ ) shown in (a and b) for 80 m height and 60 m height, respectively. .... 75

Figure 3.7 Variation of the standard error (RSE) with the relative direction ( $\beta$ ) at Site B for the wind speed bin 8–12  $\text{m s}^{-1}$  in (a, c and e) and the wind speed bin 12–16  $\text{m s}^{-1}$  in (b, d and f). The RSE is given in (e and f) for the 95% confidence interval of the observed difference between the cup and lidar measurements ( $\hat{\epsilon}_d$ ), the predicted difference between the cup and lidar measurements ( $\epsilon_d$ ), the predicted cup error ( $\epsilon_c$ ), and the predicted lidar error ( $\epsilon_l$ ). The input for the RSE predictions include the mean wind speed ( $V_0$ ) shown in (c and d) and the mean wind speed variance ( $\sigma_u^2$ ) shown in (a and b) for the wind speed bin 8–12  $\text{m s}^{-1}$  and 12–16  $\text{m s}^{-1}$ , respectively. .... 77

Figure 3.8 Variation of the standard error (RSE) with the relative direction ( $\beta$ ) at Site C at 80 m height. The RSE is given in (c) for the 95% confidence interval of the observed difference between the cup and lidar measurements ( $\hat{\epsilon}_d$ ), the predicted difference between the cup and lidar measurements ( $\epsilon_d$ ), the predicted cup error ( $\epsilon_c$ ), and the predicted lidar error ( $\epsilon_l$ ). The input for the RSE predictions include the mean wind speed ( $V_0$ ) shown in (b) and the mean wind speed variance ( $\sigma_u^2$ ) shown in (a). ..... 78

Figure 3.9 The relationship between the RSE of the relative difference between lidar and cup measurements ( $\epsilon_d$ ) and the turbulence intensity (TI) at the three sites. The 95% confidence interval for each observed RSE ( $\hat{\epsilon}_d$ ) is denoted by the marker size. The solid lines with matching colors are the predicted relationships at the sites. Prediction at Site A uses wind speed 8  $\text{m s}^{-1}$  and wind direction  $150^\circ$ , at Site B wind speed 10  $\text{m s}^{-1}$  and wind direction  $323^\circ$ , and at Site C wind speed 10  $\text{m s}^{-1}$  and wind

direction  $270^\circ$ . Values of  $\varepsilon_d$  here are derived from the cup errors related to turbulence ( $\varepsilon_c$ ) and instrument ( $\varepsilon_{cup}$ ), and the predicted lidar RSE ( $\varepsilon_l$ ) according to Eq. (3.16) and Table 3.2. .... 80

Figure 3.10 The relative standard error (RSE) in annual energy production (AEP) arising from arc scan velocity retrieval uncertainty as a function of turbulence intensity (TI) and surface roughness length ( $z_0$ ), assuming that wind speed follows a Rayleigh distribution with a mean of  $7 \text{ m s}^{-1}$ , and wind direction follows the von Mises distribution with a mean of  $90^\circ$  and standard deviation ( $SD_{dir}$ ) of  $57.3^\circ$  in (a) and  $9.1^\circ$  in (b). Four arc spans and a full azimuth conical scan (see the legend) are used for AEP prediction with six beams,  $\phi = 15^\circ$  and  $r = 315 \text{ m}$ . The normalized AEP RSE, which is the ratio of predicted RSE from arc scans to that from the conical scan, is shown in (c) for  $SD_{dir} = 57.3^\circ$  and in (d) for  $SD_{dir} = 9.1^\circ$ . .... 82

Figure 4.1 Examples of turbulence statistics of point radial velocity ( $v_r$ ) and averaged radial velocity ( $v_R$ ) derived from from Eqs. (4.6) and (4.7) with the isotropic turbulence model (Pope 2000) with streamwise velocity  $U_1 = 8 \text{ m s}^{-1}$ , turbulence intensity = 12.5%, and lidar elevation angle =  $10^\circ$ . The covariance and autocorrelation functions for  $v_r$  ( $R_r$  and  $\rho_r$ ) and  $v_R$  ( $R_R$  and  $\rho_R$ ) for azimuth angle  $\theta = 30^\circ$  are shown in (a) and (b), respectively, as functions of  $r_1/L_1$  where  $r_1$  is the spatial lag in streamwise direction and  $L_1$  is the integral length scale of streamwise velocity.  $R_R$  and  $\rho_R$  are presented in terms of  $\sigma_Q/L_1$  where  $\sigma_Q$  represents the size of volumetric averaging (see Eq. (4.5)). The effect of volumetric averaging on the integral length scale of radial velocity is presented in (c) in terms of the relationship between  $L_r/L_r$  and  $\sigma_Q/L_1$  for different  $\theta$  values where  $L_r$  and  $L_R$  are the integral length scales of  $v_r$  and  $v_R$ . .... 93

Figure 4.2 Covariance ( $R_r$  and  $R_R$  on the left) and autocorrelation functions ( $\rho_r$  and  $\rho_R$  on the right) of the point radial velocity ( $v_r$ ) and averaged radial velocity ( $v_R$ ) derived from statistically simulated time series using TurbSim with the SMOOTH model (TurbSim 2016). Parameters are set to the default values. Covariance and autocorrelation functions are presented for four different LOS orientations here as indicated by the angle of LOS relative to the mean wind direction ( $\beta$ ). The time lag ( $\tau$ ) is normalized by  $\tau_0$  which is the first time when  $\rho_r = 1/e$  at  $\beta = 0^\circ$ . A fixed elevation angle of  $10^\circ$  is used. .... 97

Figure 4.3 The relative systematic error ( $e_s$ ) and random error variance ( $e_r^2$ ) derived from the autocorrelation functions of the simulated point radial velocity ( $\rho_r$ ) and averaged radial velocity ( $\rho_R$ ) from the SMOOTH model in (a) and (c) and from the IECKAI model in (b) and (d) (TurbSim 2016) as functions of the angle between the LOS and mean wind direction ( $\beta$ ). The sampling duration is  $100\tau_0$  where  $\tau_0$  is the first time when the point radial velocity autocorrelation crosses  $1/e$  at  $\beta = 0^\circ$ . .... 98

Figure 4.4 The Time series of (a) hourly mean and (b) variance of radial velocity ( $v_R$ ) from the lidar (markers) and the sonic anemometers (lines) and time series of (c) hourly mean wind speed and (d) direction from the sonic anemometers at three

different heights. The mean and variance of radial velocity from the hourly time series classified as stationary using the method of Foken and Wichura (1996) are shown by the filled markers. The dash line in (d) gives the wind direction under which the sonic anemometers are in the center of the wind turbine wake. .... 100

Figure 4.5 An example of the autocorrelation and errors in radial velocity variance estimate using data from the hour starting at 2015-05-19 04:00 at 40 m height. The autocorrelation functions derived from the lidar and sonic measurements are presented in (a). Systematic errors ( $e_s$ ) and random errors ( $e_r^2$ ) are presented in (b) and (c), respectively. Errors associated with both lidar and sonic anemometer data are estimated using the autocorrelation function from measurements (denoted by  $M_\rho$ ) and the stationary bootstrap method (denote by  $M_b$ ) described in section 4.4.2. The red squares in (a) denote the autocorrelation function fitted with the isotropic turbulence model from Pope (2000). .... 103

Figure 4.6 Comparison of the values of radial velocity autocorrelation function from the sonic data ( $\rho_{sonic}$ ) and the lidar data ( $\rho_{lidar}$ ) at the first time lag  $\delta t = 7.5$  sec. The 95% confidence interval of  $\rho_{lidar}$  is indicated by the error bar. .... 104

Figure 4.7 Comparison of the systematic error estimated from the sonic data ( $e_{s,sonic}$ ) and from the lidar data ( $e_{s,lidar}$ ) in (a) for a sampling duration of 30 minutes and (c) a sampling duration of 55 minutes, and comparison of the random error estimated from the sonic data ( $e_{r,sonic}^2$ ) and from the lidar data ( $e_{r,lidar}^2$ ) in (b) for a sampling duration of 30 minutes and (d) a sampling duration of 55 minutes. The method used to estimate the errors is indicated by the subscript in the legend where  $\rho$  denotes the  $M_\rho$  method using the autocorrelation function and  $b$  denotes the  $M_b$  method using the stationary bootstrap method. The dark lines are the 1:1 lines. .... 105

Figure 4.8 Comparison of the lidar radial velocity systematic errors  $e_{s,\rho}$  and  $e_{s,b}$  estimated using the autocorrelation ( $M_\rho$ ) method and the stationary bootstrap ( $M_b$ ) method, respectively, for (a) a sampling duration of 30 minutes and (c) a sampling duration of 55 minutes, and comparison of the lidar radial velocity random errors  $e_{r,\rho}^2$  and  $e_{r,b}^2$  estimated using the  $M_\rho$  method and the  $M_b$  method, respectively, for (b) a sampling duration of 30 minutes and (d) a sampling duration of 55 minutes. The measurement heights can be found in the legend. .... 106

Figure 4.9 Relationships between (a) the systematic error ( $e_s$ ) and the sampling duration and (b) the random error ( $e_r^2$ ) and the sampling duration for radial velocity variance estimated from the lidar data using the autocorrelation method (gray lines) and the stationary bootstrap method (boxplots). The errors are normalized by the respective errors estimated from the autocorrelation method with the sampling duration of 55 minutes. .... 107

Figure 4.10 Contours of the relative variance ( $e_r^2$ ) of random errors of radial velocity variance from lidar measurements estimated from the isotropic turbulence model (Pope 2000) and the von Kármán spectrum model (Burton et al. 2011) as a function

of the sampling duration ( $T$ ) and the sampling interval ( $\delta t$ ) normalized by the integral time scale ( $\tau_0$ ) for four different  $\beta$  values where  $\beta$  is the angle between the LOS and the wind direction. The weighting function (Eq. (4.5)) representing the volumetric averaging has a standard deviation  $\sigma_Q = 0.2L_1$  where  $L_1$  is the streamwise integral length scale. The other input parameters include the elevation angle  $\phi = 10^\circ$  and the mean wind speed  $U_1 = 8 \text{ m s}^{-1}$ . ..... 110

Figure 4.11 Contours of the relative variance ( $e_r^2$ ) of random errors of radial velocity variance from lidar measurements estimated from the isotropic turbulence model (Pope 2000) and the von Kármán spectrum model (Burton et al. 2011) as a function of the sampling duration ( $T$ ) normalized by the integral time scale ( $\tau_0$ ) and the volumetric averaging size ( $\sigma_Q$ ) normalized by the streamwise integral length scale ( $L_1$ ) for four different  $\beta$  values in where  $\beta$  is the angle between the LOS and the wind direction. The other input parameters include the sampling interval  $\delta t = 0.5\tau_0$ , the elevation angle  $\phi = 10^\circ$  and the mean wind speed  $U_1 = 8 \text{ m s}^{-1}$ . ..... 111

Figure 4.12 Variation of the relative systematic error ( $e_s$ ) and variance of random error ( $e_r^2$ ) with respect to the sampling duration ( $T$ ) in (a) and (b), respectively, predicted from the isotropic turbulence model (Pope 2000) and the von Kármán spectrum model (Burton et al. 2011) at 80 m height under neutral conditions for surface roughness lengths ( $z_0$ ) from  $10^{-3} \text{ m}$  to  $10^0 \text{ m}$  and LOS orientations  $\beta$  from  $0^\circ$  to where  $\beta$  is the angle between the LOS and the wind direction. The blue lines with squares and the dark lines are the mean error values from the entire range of  $z_0$  and  $\beta$  for the averaged and point radial velocity variance, respectively. The red shaded areas denote the range of errors of the averaged radial variance. The equation used to estimate the integral length scale can be found in Wang et al. (2015a) with the mean wind speed  $7 \text{ m s}^{-1}$  and the Coriolis parameter  $10^{-4} \text{ s}^{-1}$ . The elevation angle  $\phi = 45^\circ$ . ..... 112

Figure 5.1 Schematics of (a) the orientation of the lidar line of sight in terms of the elevation angle ( $\beta$ ) and the azimuth angle ( $\alpha$ ), and (b) the relationship between the radial velocity ( $v_R$ ) and the wind velocity ( $\mathbf{v} = [u, v, w]$ ), and the relationship between the radial velocity and the horizontal wind speed and wind direction ( $\theta_w$ ). ..... 116

Figure 5.2 Top view of the locations of the Galion and the two wind turbines (WT1 and WT2), the scanning geometry used to probe the wake of WT2, and the two coordinate systems denoted as  $x'-y'$  and  $x-y$  (details see section 5.4.2). The azimuth angles ( $\alpha$ ) and elevation angles ( $\beta$ ) used are listed on the upper-left corner. The range gate locations are denoted by the dashed white lines. The underlying wind farm map is from the Google Earth. ..... 118

Figure 5.3 Wake profile estimation algorithm flow chart. The term  $\hat{V}$  is the wind speed estimated using the lidar data. ..... 119

Figure 5.4 Contours of the wind speed relative error as a function of the wind direction ( $\theta_w$ ) error and the angle between the LOS and the wind direction ( $\alpha - \theta_w$ ), when Eq.

- (5.5) is used to estimate the wind speed. .... 121
- Figure 5.5 Contours of the weight used to calculate the wind speed at a point (dark cross) two rotor diameters ( $2.0D$ ) downwind of WT2 using Eq. (5.6). The gray circles are the Galion range gate locations, and the range gates are indexed by the numbers at the bottom. .... 122
- Figure 5.6 An example of wind speed retrieved for one stack of PPI scan. The wind speed over the entire scanned area is shown in (a). The wind turbine rotor orientation is denoted by the dark bar with a white circle indicating the location of WT2. The dark line is the wake center and the dashed lines denote the wake width. The estimated wind speed profile across the line that is parallel to the rotor plane at  $2.0D$  downwind of WT2 is shown in (b). The definitions of wake center ( $y_{wc}$ ), the FWHM ( $S$ ), wake center wind speed ( $V_{wc}$ ) and freestream wind speed ( $V_0$ ) are also shown in (b). The wake deficit ( $\delta$  in Eq. (5.7)) as a function of the downwind distance normalized by the rotor diameter ( $D$ ) is shown in (c). .... 123
- Figure 5.7 Time series for wind speed observed at 80 m on the meteorological mast and at 40 m, 80 m and 120 m heights by the ZephIR lidar. The two red lines are the time series of the freestream wind speed ( $V_0$  in Eq. (5.7)) derived from the estimated wake profiles. .... 124
- Figure 5.8 Wake deficit observed during the wake1 period as a function of the downwind distance in (a). The detected wake center height is given in (b) and the error bars denote the range. The red line in (b) denotes the rotor bottom tip. .... 126
- Figure 5.9 Wake deficit observed during the wake2 period as a function of the downwind distance in (a). The detected wake center height is given in (b) and the error bars denote the range. The red line in (b) denotes the rotor bottom tip. ....126
- Figure 5.10 Wind shear measured by the ZephIR lidar in (a) and the wake profile derived from a PPI stack at  $2D$  downwind of WT2 in (b) during the same 10-minute period. In (b), the dark line is the wake profile and the red line is the linearly interpolated from the ZephIR measurements at 40 m and 80 m in (a). The shaped area shows height variation across the wake profile. .... 126
- Figure 5.11 The equivalent hub height wake width as a function of the downwind distance normalized by the rotor diameter ( $D$ ) for (a) the wake1 period and (b) the wake2 period. The gray and purple lines represent wake width estimates from individual PPI stacks for low and high wind speed cases, respectively. Error bars show the mean with plus/minus one standard deviation. The dark error bars are based on the equivalent hub height wake width and the red error bars are derived from the original wake width estimated directly from the Galion measurements. The purple lines the wake2 period are not included in calculating the error bars. .... 127
- Figure 5.12 Time series of the estimated wake center during the wake2 period from PPI

stacks with elevation angle  $8.0^\circ$ ,  $8.5^\circ$  and  $9.5^\circ$ , respectively. The dashed red line is the time series of wind direction. .... 129

Figure 5.13 Locations of wake centers (circles) and wind directions (lines) observed between 22:40 and 23:59 on May 17, 2012 local time. The numbers denotes the time sequence of the wake centers and wind directions. .... 130

## LIST OF TABLES

Table 2.1 Specification of Galion G4000 three-dimensional scanning Doppler wind lidar (provided by SgurrEnergy) .....	23
Table 2.2 Specifications of anemometers and wind vanes installed on M5 .....	23
Table 3.1 Galion G4000 Doppler wind lidar specification .....	66
Table 3.2 Uncertainty classification of the cup anemometers used at the three sites .....	73

## CHAPTER 1 MOTIVATION AND INTRODUCTION

Wind energy is an important renewable energy source for electricity generation (Barthelmie and Pryor 2014). Wind measurements play a central role in all aspects of wind energy applications. Wind measurements are mandatory for wind resource assessment and site suitability studies for developing new wind farms (Barthelmie et al. 2005; Sempreviva et al. 2009); they are also necessary for verifying numerical models used for wind turbine design, wind farm optimization and wind power integration into the electric grid (Barthelmie et al. 2009; Peña et al. 2015). The cubic relationship between wind speed and energy density of the wind leads to the demand for high accuracy and precision in wind measurements. Until about 2010, the standard instruments for wind measurements were cup anemometers and wind vanes mounted on meteorological (met) towers that provide (i) mean wind speed, (ii) mean wind direction, and (iii) turbulence intensity for every 10-minute period, which are the three most fundamental quantities required by any wind energy applications (IEC 2005a). As the sizes of both wind turbines and wind farms have grown, measurements are now required for a layer that extends from 30 m to 300 m above the surface and spans tens of kilometers horizontally in the atmospheric boundary layer (ABL) (Banta et al. 2013). However, measurements are difficult to obtain in these heights with the standard instruments due to the expense of installing tall met towers. Extrapolating wind speeds to these heights from lower measurement heights while using models that were developed for the surface layer (i.e., roughly the bottom 100 m of the ABL) may yield erroneous estimates (Kettle 2014). Numerical models suitable for the heights above the surface layer are not accurate enough for wind energy applications because of the lack

of knowledge of wind characteristics above the surface layer. Observations are needed above the surface layer to facilitate numerical model development, and meanwhile models being developed need measurements for verification (Peña et al. 2009a). Hence, there is a demand for new instruments that can provide high quality wind measurements over a large volume of the atmosphere in the ABL to assist wind project development and facilitate research endeavors. Remote sensing technologies provide solutions and the Doppler wind lidar is the most promising instrument because of its precision, accuracy and reliability.

### 1.1 Doppler Wind Lidar

A Doppler wind lidar (hereafter called lidar) measures winds by emitting a laser beam that is backscattered by aerosols carried by winds in the atmosphere. Motions of aerosols along the beam propagation path induce the Doppler frequency shift in the backscattered radiation. Using the aerosols as wind tracers, the lidar receives and processes the backscattered signal to detect the Doppler frequency shift ( $f_d$ ) and provide an estimate of the radial velocity ( $v_r$ ) using the following equation:

$$v_r = \frac{f_d \lambda}{2} \quad (1.1)$$

where  $\lambda$  is the laser pulse wavelength. The radial velocity is the projection of wind velocity on the line of sight (LOS) and defined as the dot product of the wind velocity vector ( $\mathbf{u}$ ) and the unit directional vector of the LOS ( $\mathbf{n}$ ):

$$v_r(s) = \mathbf{u}(s) \cdot \mathbf{d} \quad (1.2)$$

where  $s$  is the range distance on the LOS. Using the meteorological coordinates system, the velocity vector  $\mathbf{u}$  consists of the west-east ( $u$ ), south-north ( $v$ ) and vertical ( $w$ ) components and  $\mathbf{d} = (\cos \phi \sin \theta, \cos \phi \cos \theta, \sin \phi)$  where  $\theta$  is the azimuth angle

relative to the north and  $\phi$  is the elevation angle. Because the signal used for Doppler frequency shift detection is from a collection of aerosols illuminated by the laser pulse, a lidar-measured radial velocity ( $v_R$ ) at one location is a volumetric average of radial velocities within a probe volume centered at that location. The size of the probe volume varies with lidar designs.

Lidar wind measurements involve scanning geometries and wind retrieval algorithms. A scanning geometry consists of a sequence of azimuth and elevation angles with which radial velocities are measured from different directions to construct the following system of equations:

$$g(\boldsymbol{\theta}, \phi, \mathbf{s}, \mathbf{v}) = \mathbf{v}_R \quad (1.3)$$

where  $g$  denotes a functional form and  $\mathbf{v}_R$  is a vector consisting of radial velocities measured at locations corresponding to the polar coordinates  $\boldsymbol{\theta}$ ,  $\phi$  and  $\mathbf{s}$ . The values of  $\mathbf{v}_R$  are related to  $\boldsymbol{\theta}$  and  $\phi$  according to Eq. (1.2). The vector  $\mathbf{v}$  are the wind velocities that need to be measured at locations of interest. All scanning geometries are built upon the two basic scanning geometries: (i) range height indicator (RHI) and (ii) plan position indicator (PPI). An RHI scan varies the elevation angle with a fixed azimuth angle (Figure 1-1), making observations on a vertical slice in the atmosphere. RHI scans are suitable for investigating flow characteristics on a vertical plane, such as the structures of low level jets (Banta et al. 2002) and evolutions of vortices in the wake of an aircraft (Köpp et al. 2004) and in the lee of a mountain (Weissmann et al. 2009). A PPI scan varies the azimuth angle with a fixed elevation angle (Figure 1-2). Measurements from PPI scans are taken on a conical surface, but are commonly used to study horizontal flow structure by setting a low elevation angle. They are useful for flow visualization

over complex terrain (Choukulkar et al. 2012) and wind turbine wake characterization (Aitken et al. 2014; Wang and Barthelmie 2015). The arc scan is a single-stack PPI scan. A lidar in the arc scan mode scans across a small sector with a fixed elevation angle. The radial velocities acquired over an arc are then used to estimate the wind velocity that represents the mean wind condition over the area spanned by the arc. Arc scans are suitable for wind measurements over a homogeneous wind field in a small area (Schwiesow et al. 1985). The Velocity Azimuth Display (VAD) technique that uses PPI scans with 360 ° azimuth span (Figure 1-3) was first applied to radar for vertical profiling (Browning and Wexler 1968) and has been extensively used by lidar to measure vertical wind shear (Emeis et al. 2008; Peña et al. 2015). A compound scanning geometry that consists of the scanning geometries mentioned above is often used to take advantages of each scanning geometry to meet special measurement purposes. For example, Banta et al. (2002) use the wind direction from VAD scans to determine the azimuth angle of RHI scans for measuring the vertical structure of wind speed.

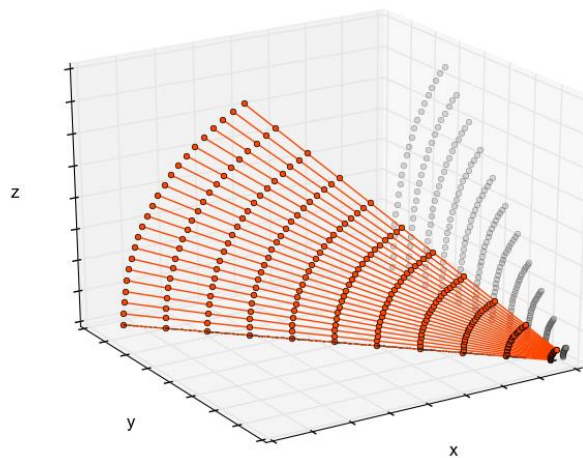


Figure 1-1 Schematic of lidar Range Height Indicator (RHI) scan geometry

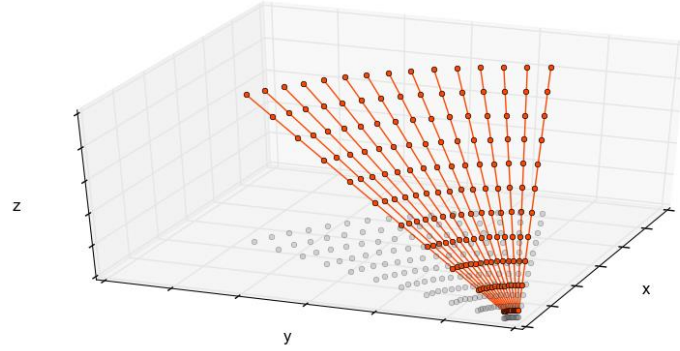


Figure 1-2 Schematic of lidar Plan Position Indicator (PPI) scan geometry

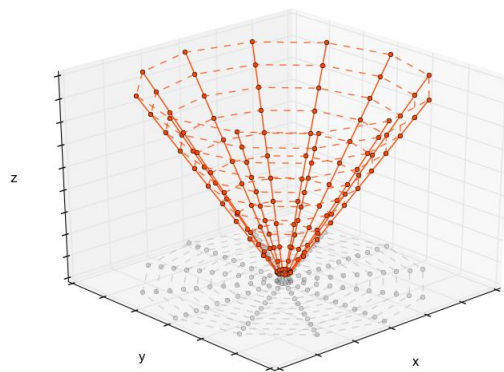


Figure 1-3 Schematic of lidar Velocity Azimuth Display (VAD) scan geometry

Wind retrieval algorithms are designed to estimate the velocity vector  $\mathbf{v}$  in Eq. (1.3) using radial velocities obtained from a scanning geometry. For a single lidar, the simplest algorithm assumes a horizontally homogeneous or linear wind field. Then Eq. (1.3) can be simplified to a linear form:

$$\mathbf{D}\mathbf{v} = \mathbf{v}_R \quad (1.4)$$

where  $\mathbf{D}$  is a matrix formed by the unit directional vector  $\mathbf{d}$  at different azimuth angles and the unknown wind velocity  $\mathbf{v}$  can be easily solved with the least squares method. This algorithm is suitable for measuring vertical profiles of wind speed with VAD scans

over flat terrain. The estimated wind velocity represents the mean wind field of the measurement volume covered by the scanning geometry. If flow is not homogeneous, the continuity equation can be imposed for wind velocity retrieval, but it requires knowledge or assumptions of boundary conditions (e.g., zero vertical wind velocity at the surface) (Weissmann et al. 2009). Advanced methods estimate three dimensional velocity fields by running numerical simulations coupled with the measured radial velocities (Chai et al. 2004). Note that a single lidar can only measure one (radial) velocity component from one direction at one location. The estimated wind velocity usually has a low spatial resolution because of the necessary assumptions of spatial homogeneity of wind velocity. The dual Doppler technique can improve the spatial resolution by providing two (radial) velocity components at one location. With two lidars scanning from different locations, radial velocities from two directions are available at each location over an overlapped two-dimensional plane (i.e., coplanar) or on an intersecting line (“virtual tower”), and wind velocity retrieval algorithms can estimate either horizontal wind velocities by assuming zero vertical wind velocity (Collier et al. 2005) or three-dimensional wind velocities by imposing the continuity equation (Drechsel et al. 2009). No assumption is needed for the spatial distribution of wind velocity; therefore, dual Doppler can provide more spatial details of wind velocity than a single lidar. The fact that measurements from both single and dual Doppler lidars are taken at different times with a scanning geometry leads to the necessary assumption of stationarity for wind retrieval. The retrieved wind velocity can only be a mean quantity. The triple Doppler technique allows instantaneous measurements of the three-

dimensional wind velocity by pointing the laser beams from three lidars at one location (Simley et al. 2016).

Lidars can use either pulsed or continuous wave (CW) laser beam. A pulsed lidar emits a laser pulse of high power. Samples of the backscattered radiation are blocked/gated to estimate the radial velocity at each range gate. Hence, a pulsed lidar can measure radial velocities at multiple range gates simultaneously. However, the measurement quality deteriorates with increasing range because of the weakening of the returned radiation. Each radial velocity measurement has the same probe volume that is the sum of the range gate length and the pulse duration. A CW lidar measures radial velocity by detecting the Doppler frequency shift in the backscattered radiation from a continuously emitted laser pulse. It can measure radial velocity at a fast rate but only at the focus of the laser beam. The probe volume increases quadratically with the focal length, which limits the maximum range of a CW lidar to, for example, about 200 m for a laser beam with 1.5  $\mu\text{m}$  wavelength when it is used from vertical profiling with the VAD scans.

## **1.2 Lidar Applications to Flow Characterization in the Atmosphere**

Lidars can remotely measure wind velocities over large areas with high spatial (10~100 m) and temporal (1~10 sec) resolutions; therefore, they are suitable for studying flow characteristics in the ABL. Although the use of lidars was limited by the availability of the instrument in the last few decades, lidars made great contributions to our knowledge of the ABL. They have made it possible to observe atmospheric phenomena to a spatial extent and a level of detail that cannot be achieved with other instruments. For example, great details of low level jets were observed through lidar

RHI scans, including the vertical structure of the mean wind speed and turbulence kinetic energy (Banta et al. 2002; Banta et al. 2006), shear flow instability within these jets (Newsom and Banta 2003) and boundary height of stable ABL (Pichugina and Banta 2010). Lidar observations have also been made over complex terrain to study features of topographically induced flows, such as wind gust structures in downslope windstorms (Neiman et al. 1988), dynamics of mountain wave rotor interaction (Weissmann et al. 2009), convergence of local drainage flows and nocturnal low-level jets in a basin (Banta et al. 2004), and the horizontal and vertical extent of flow distortion over an escarpment (Barthelmie et al. 2016). Lidars are also valuable tools for improving numerical model performance in the ABL. For example, Peña et al. (2009a) developed and verified the diabatic wind profile over homogeneous terrain for the entire ABL using lidar measurements. Both Floors et al. (2013) and Draxl et al. (2014) used the lidar measured wind profiles to evaluate the performance of the Weather Research Forecasting (WRF) model in predicting wind speed profiles under different atmospheric conditions. High resolution measurements from lidars can greatly improve the accuracy of the initial conditions and consequently the performance of numerical weather prediction models (Horányi et al. 2015).

An emerging field of interest in lidar applications in the ABL is to measure instantaneous wind velocities with multiple lidars and apply advanced wind retrieval algorithms to study the dynamics of complex flows. For example, Simley et al. (2016) made the first observations of quasi-instantaneous velocity field in front of a wind turbine with three synchronized fast scanning continuous wave lidars. Towers and Jones (2016) developed a method to retrieve the real-time wind fields for wind turbine control

from a single lidar. Another ongoing research topic is the use of lidar for turbulence measurements with the focus on the improvement and verification of existing methods that are based on radial velocity variance (Newman et al. 2015; Sathe et al. 2015), but without accounting for the volumetric averaging effect.

### **1.3 Lidar Applications in Wind Energy**

The idea of using lidar for wind energy dates back to 1970s (Bilbro 1980), but its actual adoption in the wind energy industry happened in the last ten years as the result of the rapid growth in wind turbine sizes and the availability of two fiber-based commercial lidars: ZephIR (continuous wave lidar) and WindCube (pulsed lidar). These two lidars, often referred as lidar profilers, are specifically designed with the VAD technique to measure the vertical profiles of wind velocity up to 200 m with a vertical resolution of 20-40 m to provide wind measurements across the rotor area of wind turbines (Hasager et al. 2013). These lidar profilers, in terms of accuracy and reliability, are more suitable for wind energy applications than other remote sensing technologies, such as sodar profilers which are sensitive to background noise and have low data availability under neutral conditions due to lack of temperature contrast (Bradley 2007). Therefore, lidar has become the best complement or replacement for the standard cup anemometers for wind energy applications.

Wind measurements in wind energy are used for quantitative applications that require high accuracy. Hence, before their acceptance by the wind energy industry, lidar profilers have undergone iterations of test and improvement and eventually the process of standardization. Lidars cannot fit in wind tunnels or labs; thus, performance tests can only be done through field experiments, which are difficult because of the

uncontrollable atmospheric conditions. Numerous field experiments have been conducted to evaluate the performance of lidar relative to in-situ instruments and other remote sensing technologies (Smith et al. 2006; Kelley et al. 2007; Sanz Rodrigo et al. 2013). Several error sources have been identified (Lindelöw 2009). Instrument-related errors can be eliminated or minimized by upgrading the lidar hardware and software and implementing the best practice for lidar operation. Errors associated with atmospheric conditions are well understood and methods are available to quantify these errors in the measured wind velocity (Bingöl et al. 2009; Gottschall et al. 2012). In general, vertical profilers can accurately measure wind velocity over flat terrain, but not over complex terrain where flows are not horizontally homogeneous and the conditions assumed for the VAD technique are not valid (Bingöl et al. 2009). As of today, lidar profilers have been accepted as wind measurement instruments for wind energy applications over flat terrain, and are recommended for wind turbine performance tests because wind speeds based on lidar-measured vertical profiles are more representative of the inflow conditions than a single point measurement at hub height (Wagner et al. 2011).

The success of lidar profilers has promoted the development of other types of lidars for wind energy applications. Nacelle-mounted lidars that measure wind turbine inflow conditions on top of the nacelle have been tested for both wind turbine control (Simley et al. 2014) and wind turbine power curve measurement (Wagner et al. 2014). Recent development and improvement of floating lidars are intended to ease the difficulty of offshore wind resource assessment (Gottschall et al. 2014). Scanning lidars that are considered to be the best existing wind measurement technology for wind energy (Banta

et al. 2013) have become commercially available and research has been conducted to test its potential for wind farm characterization (Krishnamurthy et al. 2013; Barthelmie et al. 2014) and offshore wind resource assessment (Pichugina et al. 2012; Wang et al. 2014). Scanning lidars have also made successful observations for wind turbine wake characterization (Aitken and Lundquist 2014; Iungo and Porté-Agel 2014; Wang and Barthelmie 2015). How to utilize scanning lidars in terms of scanning geometries, wind retrieval algorithms and uncertainty reduction and quantification is an ongoing research topic for both the industry and academia. It is also the subject of this dissertation.

#### **1.4 Research Questions**

Scanning lidars can do more than VAD scans. Mean wind speed and turbulence intensity can be estimated respectively from the mean and variance of radial velocities acquired from different scanning geometries. The best scanning geometry or sampling strategy is the one that can meet the measurement purpose with the minimum uncertainty in the estimated wind speed and turbulence intensity. Hence, knowledge of the suitability of a scanning geometry for a measurement purpose and the relationship between the scanning geometry and the uncertainty in the retrieved wind velocity is beneficial to best utilize scanning lidars for wind energy applications. This dissertation contributes to this knowledge with focus on the following three applications: (i) mean wind speed measurements from lidar arc scans, (ii) radial velocity variance estimates from lidar measurements for turbulence intensity retrieval and (iii) wind turbine wake characterization using a single lidar.

There are several potential wind energy applications of arc scans. For example, arc scans can measure wind turbine inflow conditions with lidars positioned at the base of

wind turbine, which may greatly ease the difficulty of offshore wind turbine power performance tests by eliminating the need to install support structures for wind measurement instruments (Henke and Clive 2015). However, there is only one reported application of arc scans in which the authors estimated wind speed from each half of VAD scans to study cross-mountain wind gradient (Ralph and Neiman 1997). The fact that the performance of arc scans is simply unknown raises the question of whether measurements from arc scans are accurate enough in the context of wind energy and how to quantify and reduce uncertainty through scan geometry optimization. These questions will be answered in Chapter 2 and Chapter 3 of this dissertation.

Turbulence intensity plays a key role in determining loading on wind turbines, and in principle can also be obtained using Doppler lidars. Radial velocity variance is the input parameter for majority of lidar turbulence measurement techniques being developed (Newman et al. 2015). As a second-order moment of a velocity component of the turbulent wind field, the radial velocity variance estimated from measurements is subject to both the systematic and random errors (Lenschow et al. 1994). These errors are likely to have complicated relationships with the scanning geometry and the size of volumetric averaging (Sathe and Mann 2013). Thus, in order to develop accurate methods for turbulence intensity measurements, there is a need to understand and be able to predict the uncertainty in radial velocity variance estimates, giving rise to the question about how to minimize the uncertainty by optimizing sampling strategies in terms of sampling duration, sampling rate and lidar scanning geometry. This question will be answered in Chapter 4 of this dissertation.

Lidars are ideal instruments for wind turbine wake characterization because of their

large spatial coverage. Key characteristics are wake deficit, wake center and wake width (Barthelmie et al. 2009) can be obtained from lidar measurements. Recent research further suggests that lidars could provide measurements for full scale wake model verification (Aitken et al. 2014; Iungo and Porté-Agel 2014). However, there are challenges to fully utilize lidar for wake characterization. One of the challenges is that lidar locations are always fixed while wake orientations vary with wind direction and wind turbine orientation. Thus, there are questions about how big the scanning domain should be in order to cover the moving wakes while maintaining sufficient temporal and spatial resolutions to capture the wake characteristics and how to automatically detect wakes when they enter the scanning domain. These questions will be answered in Chapter 5 of this dissertation.

The research questions mentioned above will be answered in the framework of an inverse problem (from radial velocity to wind velocity). Atmospheric turbulence introduces uncertainty in radial velocity measurements, which propagates into the estimated wind velocity through the wind retrieval method determined by the scanning geometry and the assumptions of the wind field. Hence, I postulate that the uncertainty in lidar measurements can be quantified by the following three factors: (i) the atmospheric turbulence structure, (ii) the sampling strategy including the scanning geometry and sampling duration and rate and (iii) the wind retrieval algorithm, and minimization of uncertainty can be achieved by optimizing the sampling strategy with the knowledge of atmospheric turbulence structure.

## **1.5 Outline**

Chapter 2 presents the findings from an experiment designed to assess the

performance of lidar arc scans for wind measurements. Algorithms were developed and tested for quality control, wind velocity retrieval and uncertainty quantification from arc scans. It is shown that the retrieved wind velocities at a single range gate exhibited good correlation with concurrent measurements from sonic anemometers. The vertical profiles of wind speed estimated from a conical surface also agreed well with those derived from cup anemometer measurements. The limitations of arc scans were also investigated, and the results suggest that both non-uniform wind field and non-zero vertical wind speed cause large errors in the wind velocities retrieved from arc scans. In the absence of these effects atmospheric turbulence is the major source of uncertainty in wind speeds retrieved from lidar arc scans.

Chapter 3 describes the development of a method for quantitative evaluation of the dependence of uncertainty in the horizontal wind speed retrieved from arc scans on the atmospheric turbulence and scan geometry. This method models the atmospheric turbulence using the isotropic turbulence model and the surface roughness length, and accounts for the effect of scanning geometry using the frozen turbulence hypothesis. The performance of this model was validated by arc scan measurements from three sites with different scan geometries. Both model predictions and observations indicate that the uncertainty in arc scan measurements is proportional to turbulence intensity and varies with wind direction. The minimum uncertainty is achieved by a large arc span with a low number of azimuth angles aligned with wind direction. Applying this model to common wind energy applications shows that turbulence-induced uncertainty of wind speeds retrieved from arc scans introduces negligible errors for wind resource assessment but about 10% uncertainty in wind turbine power performance test.

Chapter 4 presents the characteristics of errors in radial velocity variance estimate from lidar measurements using the analytic solutions from the isotropic turbulence model, statistically simulated data and observational data. The errors in the estimated variance depend on three factors: (i) autocorrelation function, (ii) sampling rate, and (iii) sampling duration. It was found that the volumetric averaging of lidar measurement increases values of the autocorrelation function, and, as a result, increase the errors in the radial velocity variance estimated from lidar measurements. The sensitivity of errors on the three factors was tested with the isotropic turbulence model, indicating that the most effective error reduction method is to increase sampling duration. Given that stationarity can only be valid within about one hour in the ABL, radial velocity variance estimated from lidar measurements has negligible systematic errors but will be subject to random errors with 10% standard deviation.

Chapter 5 describes the development and evaluation of an automated wake detection algorithm for application to lidar measurements. The algorithm is based on a statistical smoothing technique and requires *a priori* wind direction information. When applied to the data collected by a scanning lidar configured to measure wind speed in the wake of a continuously yawing wind turbine in the Midwest, the algorithm was able to automatically capture wakes in lidar data from PPI scans and the resultant wake statistics were consistent with previous experiment's results. However, because wakes move with wind direction and wind turbine orientation, large wind shear can introduce large errors in the retrieved wake characteristics.

Chapter 6 concludes this dissertation by summarizing the research findings of this dissertation and making recommendations for future work.

## CHAPTER 2 WIND MEASUREMENTS FROM ARC SCANS WITH DOPPLER WIND LIDAR<sup>1</sup>

### 2.1 Introduction

During the last few decades, both airborne and ground-based lidar have been developed and applied to remotely measure wind velocity (Menzies and Hardesty 1989; Rye and Hardesty 1997; Werner et al. 2001). Among the most versatile and useful of these remote sensing technologies in the atmosphere boundary layer is the coherent Doppler wind lidar (herein called *lidar*), which uses the coherent heterodyne technique to detect a Doppler frequency shift in the laser light backscattered from aerosols carried by winds and to estimate wind velocity along the line of sight or radial velocity (Hardesty et al. 1997; Werner 2005). Measurements of radial velocity from more than three different locations are required to reconstruct the three-dimensional wind vector; hence, a lidar needs to operate with a preconfigured scanning geometry that guides it to scan at different combinations of azimuth and elevation angles. Choosing an appropriate scanning geometry is based on measurement needs (see Figure 2-1). Two basic types of scanning geometries are the plan position indicator (PPI) and the range-height indicator (RHI). A PPI scan holds the elevation angles constant but varies the azimuth angle, providing wind data on a conical surface. As a result, PPI scan has large coverage in the horizontal plane and is often used to investigate horizontal flow structures and dynamics over a large spatial domain (Choukulkar et al. 2012). Spatial statistics of turbulence can

---

<sup>1</sup> Wang, H., R. J. Barthelmie, A. Clifton, and S. C. Pryor, 2015: Wind Measurements from Arc Scans with Doppler Wind Lidar, *Journal of Atmospheric and Oceanic Technology*, **32**, 2024-2040. doi: 10.1175/JTECH-D-14-00059.1

also be derived from PPI scans using radial velocity structure functions and the von Kármán model (Frehlich and Cornman 2002). An RHI scan keeps the azimuth angle constant but varies the elevation angle, collecting radial velocities for a vertical slice in the atmosphere. RHI scans can be used to observe vertical profiles of the mean and standard deviations of wind speed as well as momentum fluxes by assuming homogeneous wind fields in multiple elevations (Gal-Chen et al. 1992; Banta et al. 2006). A velocity-azimuth display (VAD) scan uses a full 360 azimuth PPI scan, usually with a large elevation angle, is suitable for measuring vertical wind shear above a given “point” in space (Werner 2005). Lidars can also operate in a staring mode (non-scanning) by fixing the azimuth and elevation angles. This mode is suitable for deriving turbulence statistics and measuring vertical wind speeds (Frehlich et al. 1998; Lothon et al. 2006).

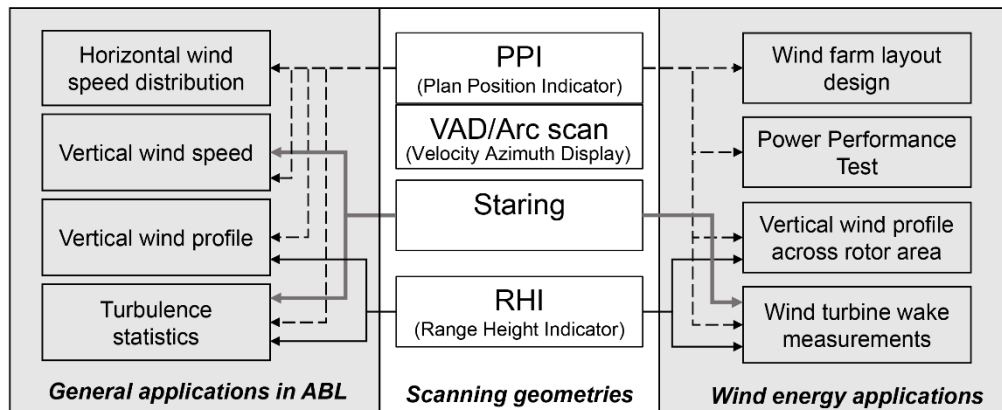


Figure 2-1 Flow diagram of lidar scanning geometries and their applications in studying flow characteristics in the Atmospheric Boundary Layer (ABL) and facilitating wind energy development.

Retrieval techniques usually employ assumptions of a horizontally homogeneous or linear wind field and use the least square fit method to estimate wind velocities (Banta

et al. 2002; Krishnamurthy et al. 2013) (see section 2.3a). If the wind field is inhomogeneous, the optimal interpolation may be employed for wind retrieval (Choukulkar et al. 2012). An alternative to the optimal interpolation is four dimensional variational data assimilation, in which measured radial velocities are assimilated into numerical models to produce a time-evolving, three dimensional wind field (Chai et al. 2004).

Three-dimensional scanning lidars have become economically feasible for wind energy applications and have been applied in a range of configurations to improve understanding of wind properties within and beyond modern wind turbine rotor areas and across whole wind farms (Emeis et al. 2008; Banta et al. 2013; Hasager et al. 2013). For example, with multiple PPI scans enclosing a large volume of the atmosphere, Krishnamurthy et al. (2013) showed that lidars can facilitate wind farm layout optimization using the derived spatial distribution of wind speed. (Banta et al. 2008) applied RHI scans to lidars and revealed characteristics of the Great Plains nocturnal low-level jet that are of value to wind resource assessments and wind farm operations. Lidars operated with VAD scans have become essential instruments for conducting wind resource assessment and wind turbine power performance tests (Wagner et al. 2011; Gottschall et al. 2012). They are used primarily to measure vertical wind shear up to approximately 200 m, thus reducing uncertainty related to wind profile extrapolation over the rotor disk (Wagner et al. 2011). Other applications include measuring inflow conditions for wind turbine control (Simley et al. 2014) and investigating flow dynamics in the wake (Bingöl et al. 2010). Using dual lidars, it is possible to observe the complex flow structure and turbulence spectra in the wake of a wind turbine (Iungo et al. 2013).

Although most lidar deployments to date have occurred onshore, the feasibility of using lidars for offshore wind energy applications has been evaluated by Peñã et al. (2009b) and Pichugina et al. (2012).

To meet the requirements of wind resource assessment, lidars need to provide accurate measurements of the 10-minute mean wind speed profile and turbulence intensity across the rotor disk (IEC 2005b). This can be achieved in several ways. The VAD technique can be applied to measure mean wind speed profiles above the lidar location. A suitable elevation angle is required to ensure that flow is horizontally homogeneous within the area scanned by the lidar. Volumetric scans formed by multiple stack PPI scans can provide coverage of wind velocity over the entire wind farm, but their low temporal resolution can lead to high uncertainty in wind speed and consequently wind power prediction (Stawiarski et al. 2013).

Arc scans, such as those presented here, are another option that have some advantages over the VAD scans and volumetric scans. In this configuration, lidars scan with a fixed elevation angle and cover a small azimuth range (i.e. a sector scan), so that large-scale horizontal inhomogeneity has less impact on wind velocity retrievals than it does in a  $360^\circ$  VAD scan (Schwiesow et al. 1985). Use of a low number of azimuth angles over a small sector can also increase the temporal sampling rate and therefore reduce uncertainty in 10-min wind speed estimates (Banakh et al. 1995), and the scanning azimuth angle can be systematically varied to measure wind velocity in any direction from the lidar location. Last, for low elevation angles arc scans can be used to measure vertical wind shear with a high resolution by assuming horizontal homogeneity and averaging it over a volume with a small horizontal footprint.

Uncertainty in the retrieved wind velocity from arc scans is related to wind turbulence properties and scanning geometries (Banakh et al. 1995). Understanding this relationship is critical to quantifying and reducing uncertainty by optimizing scanning geometry and improving data processing techniques to enhance utility to wind energy applications. The objective of this paper is to use lidar observations from a field experiment to present a synthesis of sources of uncertainty in wind velocity retrievals from arc scans, to quantify the uncertainty, and to make recommendations regarding best practices for arc scan geometries. The experiment set up and instrument specifications are described in section 2. The wind retrieval method and data quality control techniques are presented in section 3. Section 4 presents an evaluation of uncertainties in the retrieved wind speed and direction. A brief discussion is given in section 5 regarding the best practices for the arc scan method and data processing.

## **2.2 Experimental Setup**

### **2.2.1 Site**

This experiment was conducted at the National Wind Technology Center (NWTC) in Colorado from 15 to 25 February 2013. The site in the immediate vicinity of the NWTC is flat, with only a 20-m surface elevation change throughout a  $2 \text{ km} \times 2 \text{ km}$  square (Figure 2-2), but it is surrounded by complex terrain. The foothill of the Front Range are located approximately 5 km to the west, and as a result westerly winds during the experiment period were often associated with drainage flows from Eldorado Canyon (Clifton et al. 2013b). This complex terrain can cause inhomogeneous flow conditions (Wyngaard 2010) and introduce errors to the wind speed estimated from the arc scan. On the northern edge of the site there is a building complex, and on the eastern edge

there a row of installed wind turbines. Measurements on a 134-m meteorological tower (denoted as M5) installed approximately 150 m west of the wind turbines were used in this paper to evaluate lidar performance.

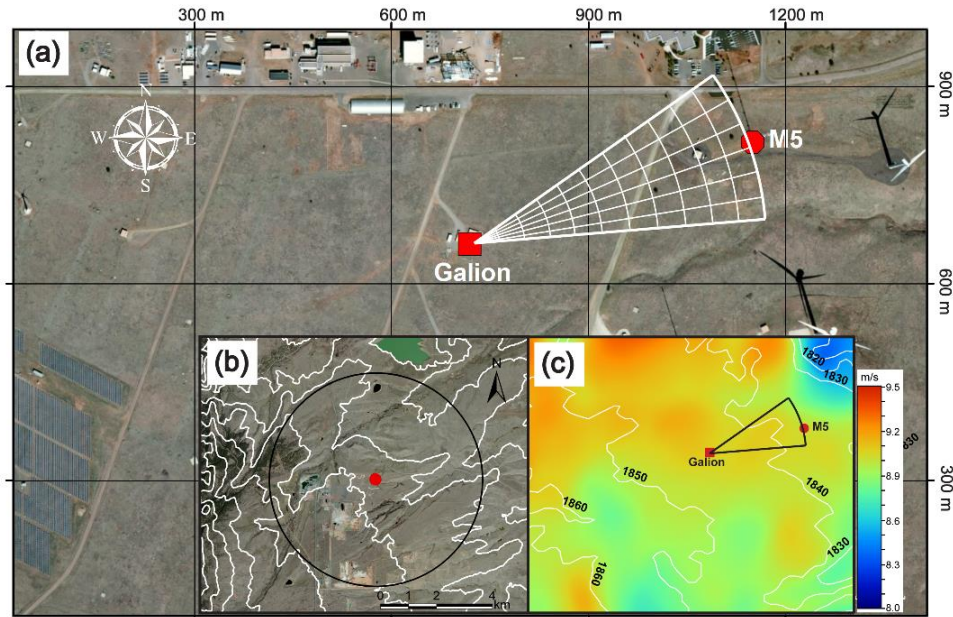


Figure 2-2 (a) Layout of the test site at the NWTC. The Galion lidar location is denoted by the red square, and the M5 is denoted by the red circle. The distance between the lidar and M5 is approximately 150 m. The location of the lidar range gates are depicted by the circular grids between M5 and the Galion. (b) The inset shows the topography surrounding the site. The interval of the overlaid elevation contour lines (white) is 50 m. The radius of the dark circle is 3.7 km, within which uniform terrain is required for horizontally homogeneous flow (Wyngaard 2010). (c) The inset shows the wind speed spatial distribution simulated by WASP Engineering and the elevation contour lines (white lines and 10-m interval) derived from Shuttle Radar Topography Mission elevation data. This WASP Engineering simulation is based on a wind speed of  $9 \text{ m s}^{-1}$  and a wind direction of  $272^\circ$  at a height of 74 m at the location of M5.

To examine the wind speed spatial variability at the site because of terrain and surface roughness changes, Wind Atlas Analysis and Application (WASP) Engineering (Mann et al. 2002) simulations were run in the range and scale of the proposed observations for 16 wind directions covering the directional sector  $210^\circ$ – $360^\circ$  that is used in the analysis presented herein. Note that the snow covered surface during part of

the experiment period may have produced a more homogeneous surface with lower roughness and therefore resulted in flow-surface interaction that are more reproducible by the linearized model of WAsP Engineering. Figure 2-2 shows an example of the simulation output for an incident wind speed of  $9 \text{ m s}^{-1}$  and a wind direction  $272^\circ$  at a height of 74 m at M5. Simulation results indicated a relatively homogenous flow field in the area scanned by the lidar. Wind speed varied no more than  $0.2 \text{ m s}^{-1}$  throughout the area scanned by the lidar at a height of 74 m. However, it should be noted that output from WAsP Engineering provided a simplified representation of flow conditions at the site and, as discussed below, the real flow field may exhibit larger spatial variability than was manifested in these simulations because of mesoscale forcing.

### **2.2.2 Pulsed Coherent Doppler Lidar**

The Galion G-4000 pulsed Doppler lidar, distributed by SgurrEnergy, has three-dimensional scanning capability and was used in this experiment (see specifications in Table 2-1). The lidar was deployed approximately 350 m west of M5 (see Figure 2-2). The arc scan used for this experiment was designed so that the center of the arc at range gate 11 was close to the sonic anemometer mounted at a height of 74 m on M5. The range gate size was 30 m, and the elevation angle was  $12.7^\circ$ ; thus, the center of range gate 11 was 76 m above the ground. The lidar scanning geometry was set with seven azimuth angles of  $55.8^\circ$ – $85.8^\circ$  with a  $5^\circ$  interval. It took approximately 3 s to complete one measurement and start a new one at the next azimuth angle; thus, there were approximately 25–28 radial velocity measurements per range gate over 10 min.

### **2.2.3 Meteorological Tower M5**

Measurements from the instruments on M5 (Table 2-2) were used as the reference data to evaluate the accuracy of wind velocity retrieved from the arc scan. Sonic

anemometers were mounted at six heights on long booms (boom length to face width ratio = 5.7) oriented 278 ° clockwise from the north. The sonic anemometer and the lidar used the same frame of reference in which the vertical axis was aligned with the local gravitational field. Sonic anemometers sampled at the rate of 20 Hz. High-frequency measurements were flagged as missing if they were beyond the valid data range ( $\pm 30 \text{ m s}^{-1}$ ). A 10-min time series of the sonic data were excluded if missing data exceeded 30%. Two types of cup anemometers were mounted on short boom (boom length to face width ratio = 2.8) attached to M5 at multiple heights and oriented 278 ° clockwise from the north (Table 2-2). Data exceeding the valid range ( $75 \text{ m s}^{-1}$ ) were removed to calculate the 10-min mean wind speeds from the cup anemometers.

Table 2-1 Specification of Galion G4000 three-dimensional scanning Doppler wind lidar (provided by SgurrEnergy)

Parameter	Value
Wave length ( $\mu\text{m}$ )	1.5
Pulse energy ( $\mu\text{J}$ )	30
Pulse duration (ns)	200
Pulse repetition frequency (kHz)	20
Aperture diameter (mm)	75
Focal length (m)	300
Maximum range (m)	4000
Radial velocity accuracy ( $\text{m s}^{-1}$ )	0.1

Table 2-2 Specifications of anemometers and wind vanes installed on M5

Parameter	Instrument	Height [m]	Range	Accuracy
Wind speed	Met One SS-201 cup anemometer	3, 10, 38, 87, 122	0 – 90 $\text{m s}^{-1}$	0.5 $\text{m s}^{-1}$ or 2%
Wind speed	Thies 4.3351.10.0000	30, 51, 80, 105, 130	0 – 75 $\text{m s}^{-1}$	0.2 $\text{m s}^{-1}$ or 1%
Wind direction	Met One SD-201 vane	3, 10, 38, 87, 122	0 – 360 °	3.6 °
Wind vector	ATI 'K'-type sonic anemometer	15, 41, 61, 74, 100, 119	$\pm 30 \text{ m s}^{-1}$	0.01 $\text{m s}^{-1}$

## 2.3 Wind Retrieval Method

This section briefly describes assumptions and methods used for the wind velocity retrieval from the arc scan and data quality criteria applied. The detailed mathematical description of the wind retrieval algorithm and uncertainty quantification is given in the appendix.

### 2.3.1 Assumptions

The wind field was assumed to be horizontally homogenous and stationary within 10 min. The wind vector is denoted as  $\mathbf{v}$ , and its three components are expressed as the sum of the mean and the turbulent fluctuation:

$$u = u_0 + u' \quad (2.1)$$

$$v = v_0 + v' \quad (2.2)$$

$$w = w_0 + w' \quad (2.3)$$

where positive  $u$ ,  $v$  and  $w$  are the instantaneous west-east, south-north, and upward vertical wind components, respectively. The letters with subscript 0 denote the means, and those with a prime superscript denote the turbulent fluctuation terms, which are assumed to have zero means. Similarly, the radial velocity ( $v_R$ ) measured by the lidar is defined as the sum of its mean ( $v_{R0}$ ) and turbulent fluctuation term ( $v'_R$ ):

$$v_R = v_{R0} + v'_R \quad (2.4)$$

where

$$v_{R0} = u_0 \cos \phi \sin \theta + v_0 \cos \phi \cos \theta + w_0 \sin \phi \quad (2.5)$$

$$v'_R = u' \cos \phi \sin \theta + v' \cos \phi \cos \theta + w' \sin \phi \quad (2.6)$$

In the above-mentioned equations,  $\theta$  is the azimuth angle clockwise from the north and  $\phi$  is the elevation angle. Because  $v_R$  is a linear combination of  $u$ ,  $v$  and  $w$ , it

a mean defined in Eq. (2.5) and variance, denoted as  $\langle v_R'^2 \rangle$ , given by (Eberhard et al. 1989):

$$\langle v_R'^2 \rangle = A_0 + A_1 \cos \theta + B_1 \sin \theta + A_2 \cos 2\theta + B_2 \sin 2\theta \quad (2.7)$$

$$A_0 = \frac{\cos^2 \phi}{2} (\langle u'^2 \rangle + \langle v'^2 \rangle + 2 \tan \phi^2 \langle w'^2 \rangle + \sigma_\varepsilon^2) \quad (2.8)$$

$$A_1 = \langle u'w' \rangle \sin 2\phi \quad (2.9)$$

$$B_1 = \langle v'w' \rangle \sin 2\phi \quad (2.10)$$

$$A_2 = -\frac{\cos^2 \phi}{2} (\langle u'^2 \rangle - \langle v'^2 \rangle) \quad (2.11)$$

$$B_2 = \langle u'v' \rangle \cos \phi^2 \quad (2.12)$$

where  $\langle \cdot \rangle$  denotes the ensemble average in time and space, and  $\sigma_\varepsilon^2$  is the lidar measurement error variance. According to Eq. (2.5), given that  $v_{R0}$  is available at more than three different azimuth angles at the same height, the three mean wind components can be estimated by solving the ordinary least squares equation [i.e. Eq. (2.A10)]. However, because the radial velocity variance depends on the azimuth angle, the weighted least squares (WLS) [i.e. Eq. (2.A11)] provide more accurate wind velocity estimates.

Vertical wind speed is not retrievable at the same time as the two horizontal components  $u_0$  and  $v_0$  from the arc scan, because the least squares method—including vertical wind speed—is unstable and has a high sensitivity to the turbulent variation of the radial velocity (Banakh et al. 1995). Uncertainty in the radial velocity propagates into the retrieved wind velocity according to the following equation (Demmel 1997):

$$\frac{\|\delta \mathbf{v}\|}{\|\mathbf{v}\|} \leq K(\mathbf{G}) \frac{\|\delta \mathbf{v}_R\|}{\|\mathbf{v}_R\|} \quad (2.13)$$

where  $\|\cdot\|$  denotes the norm of a vector,  $\|\delta\mathbf{v}_R\|/\|\mathbf{v}_R\|$  is the relative variation in radial velocity, and  $\|\delta\mathbf{v}\|/\|\mathbf{v}\|$  is the resultant variation in the retrieved wind velocity. The term  $K(\mathbf{G})$ , the *cond* number of  $\mathbf{G}$  defined in Eq. (2.A6), is the ratio of the maximum and minimum singular values of  $\mathbf{G}$ . Thus, Eq. (2.13) allows  $K(\mathbf{G})$  to be used as a measure of sensitivity of the retrieved wind velocity to the variation in radial velocity. In the experiment at the NWTC,  $K(\mathbf{G}) = 345.5$  if vertical wind speed is included in Eq. (2.A7), which can cause the variation in the radial velocity to increase by two or three order of magnitude when Eq. (2.A10) is solved for wind velocity (see Figure 2-3a). Naturally, vertical wind speed can be retrieved if the elevation angle is close or equal to  $90^\circ$ . However,  $u_0$  and  $v_0$  are not retrievable because of their small contributions to the radial velocity [as shown in (2.5)]. For the conditions during the NWTC experiment,  $K(\mathbf{G})$  reached its lowest value of 150 for  $\phi = 45^\circ$ . This is still unacceptably high and thus demonstrates that vertical wind speed cannot be retrieved simultaneously with  $u_0$  and  $v_0$ .

The inversion procedure in Eq. (2.A10) can be stabilized by setting  $w_0 \sin \phi = 0$  Eq. (2.5). When  $\phi$  and/or  $w_0$  are low, the radial velocity has little contribution from the vertical wind speed, and hence it is appropriate to assume  $w_0 = 0$  in the wind velocity retrieval. By assuming  $w_0 = 0$ ,  $K(\mathbf{G})$  reduces to 5.7 and the estimated velocity variation increases by no more than 2 (Figure 2-3). Neglecting vertical wind speed, however, introduces bias to the estimated  $u_0$  and  $v_0$ . The expected value of bias ( $\beta$ ) for  $N_\theta$  azimuth angles is defined as (Myers 1990):

$$\langle \beta \rangle = \tan \phi W \mathbf{B} \quad (2.14)$$

where  $\mathbf{B} = (\mathbf{X}^T \mathbf{X})^{-1} \mathbf{X}^T \mathbf{1}$  (2.15)

$$= \begin{bmatrix} \sin \theta_1 & \cos \theta_1 \\ \vdots & \vdots \\ \sin \theta_N & \cos \theta_N \end{bmatrix}_{N \times 2} \text{ and } \mathbf{1} = [1, \dots, 1]^T_{N \times 1} \quad (2.16)$$

The value of  $\langle \boldsymbol{\beta} \rangle$  computed this way are  $0.216w_0$  for  $u_0$  and  $0.075w_0$  for  $v_0$  in this experiment. They are thus much lower than the uncertainty caused by including vertical wind speed, provided that  $w_0$  is low (i.e.,  $u_0 \gg w_0$ ,  $v_0 \gg w_0$ , as shown in Figure 2-3).

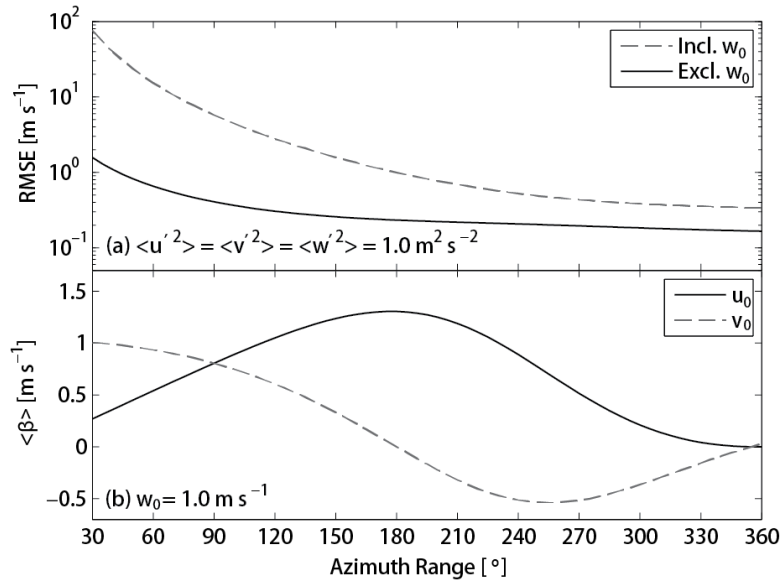


Figure 2-3 (a) The modeled root mean square error (RMSE) of the retrieved wind velocity with and without vertical wind speed according to Eq. (2.A12) in the Appendix, and (b) the expected value of bias  $\langle \boldsymbol{\beta} \rangle$  in  $u_0$  and  $v_0$  introduced by  $w_0 = 1.0 \text{ m s}^{-1}$  and elevation angle =  $12.7^\circ$  according to (2.14). In (a), wind components  $u$ ,  $v$  and  $w$  are assumed to be independent and have the same variance  $1.0 \text{ m}^2 \text{ s}^{-2}$ . The first line of sight of the azimuth range was at  $\theta = 0^\circ$ .

### 2.3.2 Radial velocity quality control

The accuracy of (and by association uncertainties in) lidar radial velocity measurements is determined by the signal-to-noise ratio (SNR) (Frehlich 1997). Thus, a high SNR is required to ensure data quality. A threshold of 0.01 (-20 dB) was used for the lidar deployed in this experiment. Because statistical properties were available from 25 to 28

radial velocity measurements per 10 min at each range gate, additional quality control procedures were applied, including a combination of SNR, outlier detection, and despiking. Radial velocity measurements at a given range gate within a 10-min period were subject to the following data selection criteria:

- 1) A radial velocity with  $\text{SNR} < 0.01$  (-20 dB) was flagged with an error code. A radial velocity with  $\text{SNR} > 10$  (10 dB) and  $v_R < 0.25 \text{ m s}^{-1}$  was assumed to be caused by hard targets and hence flagged as an error. Given that 50% of the data must be considered valid to derive an accurate estimate of interquartile range (IQR) in step 2, a 10-min time series was considered missing and excluded from further processing if the count of flags because of low/high SNR  $> 12$ .
- 2) Data that passed step 1 were then used for outlier detection using the box plot method (Hoaglin et al. 1983), wherein a radial velocity is an outlier if

$$v_R > v_{R,75} + 1.5IQR$$

$$v_R < v_{R,25} - 1.5IQR \quad (2.17)$$

or

where  $v_{R,25}$  and  $v_{R,75}$  are the 25<sup>th</sup> and 75<sup>th</sup> percentiles of the time series, respectively. Figure 2-4 shows an example in which an outlier passed the SNR test but failed the criteria in Eq. (2.17).

- 3) Spikes were detected in data that pass step 1 using the difference between the two consecutive measurements ( $\Delta v_R$ ) (Rebmann et al. 2012). A spike is defined from both sides (i.e. the preceding and subsequent measurement) if

$$|\Delta v_R| > 2 \cdot IQR_{\Delta} \quad (2.18)$$

and they have different signs (Figure 2-5).  $IQR_{\Delta}$  is the  $IQR$  of  $\Delta v_R$ .

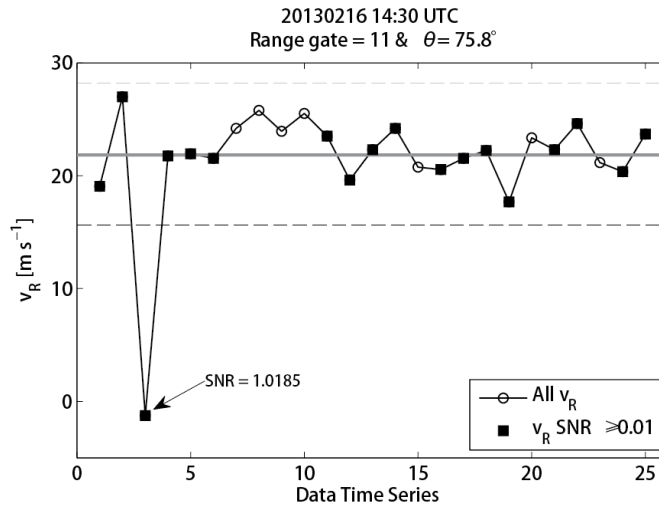


Figure 2-4 Outlier detection of lidar radial velocity ( $v_R$ ) based on Eq. (2.17) for a 10-minute time series measured at range gate 11 and azimuth angle  $75.8^\circ$ . The dashed lines are the outlier bounds beyond which measurements are treated as outliers. In this case, the outlier (the 3<sup>rd</sup> measurement) has a high SNR, but is identified as an outlier per Eq. (2.17).

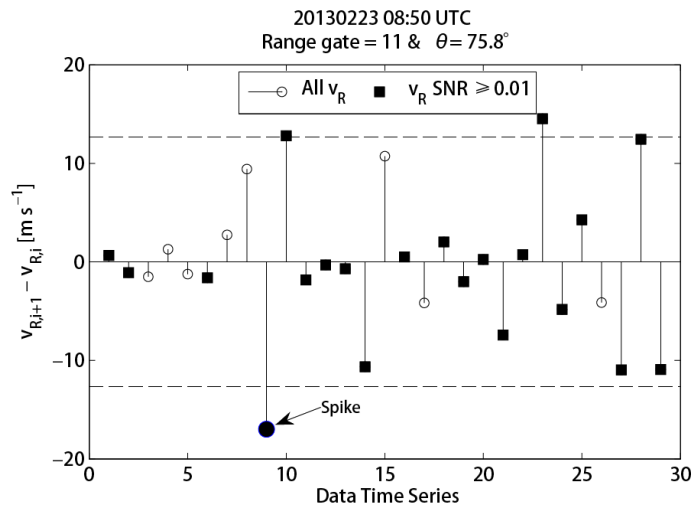


Figure 2-5 Spike detection of lidar radial velocity ( $v_R$ ) based on the radial velocity difference between the two neighboring measurements ( $v_{R,i+1} - v_{R,i}$ ) for a 10-minute time series. Measurements were taken at range gate 11 and an azimuth angle of  $75.8^\circ$ . As defined in Eq. (2.18), a spike is detected if  $|v_{R,i+1} - v_{R,i}| > 2IQR_\Delta$  as shown by the dashed lines. Also, different signs for two adjacent points are required to confirm a spike. In this case, the difference between data point 8 and 9 and the difference between data point 9 and 10 were outside of the dashed lines, and they have different signs. Therefore, data point 9 was identified as a spike.

All outliers and spikes identified were removed from the time series to allow more

reliable estimates of variance for uncertainty quantification.

### 2.3.3 Estimating mean wind velocity

After outliers and spikes were detected and removed using the methods described in section 2.3.2, the mean and variance of radial velocity over 10 min were calculated for all range gates. WLS was then used to estimate  $u_0$  and  $v_0$  using Eq. (2.A11) (Myers 1990). In this analysis, the measured 10-min mean radial velocity at each range gate was assumed to be independent, and hence its covariance matrix that defines the weight matrix for WLS only has diagonal entries given by  $\langle v_R'^2 \rangle / n_{10}$ , where  $n_{10}$  is the number of measurements used for averaging in each 10-min period. WLS has the advantage of incorporating measurement uncertainties into the estimates of  $u_0$  and  $v_0$ , as  $\langle v_R'^2 \rangle$  and  $n_{10}$  represent uncertainties associated with turbulence fluctuation and sample size, respectively. Moreover, WLS should have higher accuracy than the ordinary least squares, given the dependence of radial velocity variance on azimuth angles [as shown in Eq. (2.7)].

Cook's Distance is a measure of the influence of an observation on the predicted coefficients of WLS (Myers 1990). It can be used to find observations that significantly affect the retrieved wind velocity and thus is used to detect outliers possibly arising from inhomogeneous wind fields. Cook's Distance was applied for the arc scan implemented in this experiment once per averaging time with a threshold value 1.0 according to the formula  $4/(N-k-1)$  where  $N = 7$  and  $k = 2$  for 7 azimuth angles and 2 coefficients ( $u_0$  and  $v_0$ ) (Myers 1990). If the sample number is low, the columns of the WLS model matrix become linearly dependent and uncertainty will increase in the estimated wind velocity. Thus, outliers detected using Cook's Distance were removed, and the wind

velocity was estimated only if the mean radial velocities were available for at least 5 azimuth angles, that is,  $\geq 5/7$  of the data are available for WLS.

The goodness-of-fit of WLS was evaluated using the coefficient of determination ( $R^2$ ) derived from the measured and fitted 10-min radial velocity. In orthogonal scans, the mean radial velocity is close to zero, because the wind direction is perpendicular to the line-of-sight. The variance, however, does not decrease proportionally with the mean as shown in Eq. (2.7). It is independent of wind direction if turbulence is isotropic. Thus,  $R^2$  has low values when orthogonal scans occur. Statistical simulation showed that, if the wind field is horizontally homogenous,  $R^2 > 0.8$  for 99% of cases of orthogonal scans. For non-orthogonal scans,  $R^2 > 0.9$  for all cases. Hence, a threshold value 0.8 was chosen for  $R^2$ . Cases with  $R^2 < 0.8$  indicate bad fits that may be associated with violation of the homogeneity assumption.

The standard error of the retrieved wind speed, denoted as  $\sigma_V$  hereafter, can be approximated by the following equation and used as a measure of uncertainty (Lyons 1991):

$$\sigma_V = \frac{1}{V} \sqrt{(u_0 \sigma_{u_0})^2 + (v_0 \sigma_{v_0})^2 + 2\rho_{u_0 v_0} \sigma_{u_0} \sigma_{v_0} u_0 v_0} \quad (2.19)$$

where

$$V = \sqrt{u_0^2 + v_0^2}$$

In Eq. (2.19),  $\sigma_{u_0}$  and  $\sigma_{v_0}$  are the estimated standard errors for  $u_0$  and  $v_0$ , respectively;  $\rho_{u_0 v_0}$  is the estimated correlation between  $u_0$  and  $v_0$ ;  $V$  is the estimated wind speed. Values of  $\sigma_{u_0}$ ,  $\sigma_{v_0}$  and  $\rho_{u_0 v_0}$  can be found from the covariance matrix calculated from Eq. (2.A12), assuming that the radial velocity at each range gate is independent. The standard error  $\sigma_V$  includes uncertainties caused by both

wind speed fluctuation and instability of WLS. It should be noted that errors can be introduced into  $\sigma_V$  if the term  $w_0 \sin \phi$  is non-zero.

## 2.4 Results and Discussion

Using the methods described in the previous section, 10-min mean wind speeds and directions were retrieved from the arc scans conducted at the NWTC and evaluated against concurrent anemometer measurements from M5. Among the 1556 records collected over 11 days by the lidar, 325 were flagged as missing as the result of the data quality procedure and 165 had poor goodness-of-fit ( $R^2 < 0.8$ ). However, an evaluation is only conducted for free stream sectors ( $210^\circ$ – $360^\circ$ ) in which flow was not distorted by the meteorological mast or the nearby wind turbines [where flow distortion is determined using the method defined in (IEC 2005a)]. Period when  $|w_0| > 1 \text{ m s}^{-1}$  (based on the sonic data at 74 m height on M5) were also excluded, since large vertical wind speeds at the site were associated with non-stationary and non-homogenous drainage flows from the west.

The accuracy of lidar measurements was evaluated in terms of two linear regression,

$$y_{lidar} = b_0 + b_1 x_{ref} \quad (2.20)$$

and

$$y_{lidar} = a_1 x_{ref} \quad (2.21)$$

where  $a_1$ ,  $b_1$  and  $b_0$  are the coefficients;  $x_{ref}$  is the reference data from M5; and  $y_{lidar}$  the retrieved lidar data, in terms of the absolute error ( $e_{abs}$ ) defined as

$$e_{abs} = y_{lidar} - x_{ref} \quad (2.22)$$

and the relative error ( $e_{rlv}$ ), defined as

$$e_{rlv} = (y_{lidar} - x_{ref})/x_{ref} \quad (2.23)$$

The bias (BIAS) and root-mean-squared-error (RMSE) were then defined as the mean

of  $e_{abs}$  or  $e_{rlv}$  and the square root of the mean of squared  $e_{abs}$  or  $e_{rlv}$ , respectively. In the following section,  $V$  and  $D$  will be used to denote the 10-min mean wind speed and direction, respectively, and subscripts are used to differentiate data from different instruments. For example,  $V_{lidar}$  is the lidar mean wind speed and  $D_{sonic}$  is the sonic mean wind direction.

#### **2.4.1 Mean wind speed**

The accuracy of  $V_{lidar}$  was evaluated by comparing 254 pairs of  $V_{lidar}$  at range gate 11 and  $V_{sonic}$  at 74 m height on M5 (Figure 2-6). There was relatively large scatter between  $V_{lidar}$  and  $V_{sonic}$  with  $R^2 = 0.956$  and  $RMSE = 0.72 \text{ m s}^{-1}$ . The fitted  $b_1$  and  $a_1$  are both  $> 1.0$  mainly because that  $V_{lidar} > V_{sonic}$  at high wind speeds. Except a few outliers (which are discussed in more details below), the RMSE scaled to wind speed.

Instrument errors should have little contribution to the scatter because of the stringent quality control procedure described above. The lidar pitch and roll were well below  $0.5^\circ$ ; therefore, the associated errors would be much lower than 0.6% of the true wind speed and negligible. The scatter shown in Figure 2-6 was likely caused by turbulent wind fluctuation, WLS instability and a violation of the assumption of homogeneity. These sources are quantified in the following analysis.

#### **Turbulence and error**

High turbulent wind fluctuation, which is commonly measured by the standard deviation of wind speed, affects lidar measurements in the following two ways. First, radial velocity measured by the lidar is a spatially weighted average in a volume along the line of sight, but ascribed to a radial velocity at the center of a range gate (in this

analysis range gate 11) (Frehlich 1997). Thus, high uncertainties in radial velocity measurements are expected when turbulent wind fluctuation increases in the sampled volume. The other effect of high turbulent fluctuation is related to the instrument sampling rate. The lidar was configured to take measurements at 7 azimuth angles, and each measurement took approximately 3 seconds. This sampling rate resulted in only one sample every 18 s for one azimuth angle. When rapidly fluctuating winds are present, a low sampling rate can cause high uncertainty in the estimated mean radial velocity and eventually the estimated wind velocity.

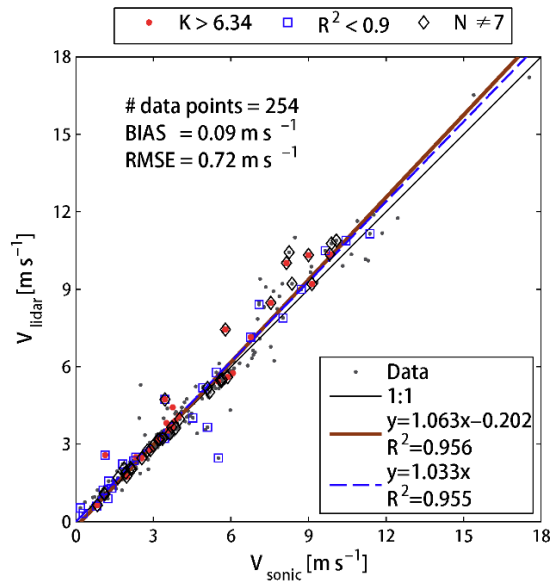


Figure 2-6 Relationship between the 10-min mean wind speed from the sonic anemometer ( $V_{sonic}$ ) at 74 m height on M5 in the free stream sector (210°–360°) and lidar range gate 11 ( $V_{lidar}$ ). Lidar data with high *cond* numbers of the model matrix  $[K(\mathbf{G})]$  are marked with red dots, low  $R^2$  of the WLS fits are shown by the blue squares, and estimates derived using data with a high number of missing measurements at some azimuth angles are shown as dark diamonds.

Turbulence kinetic energy (TKE), defined as

$$TKE = \frac{1}{2} (\langle u'^2 \rangle + \langle v'^2 \rangle + \langle w'^2 \rangle) \quad (2.24)$$

is used in to demonstrate the effects of turbulent wind fluctuation on lidar errors. As shown,  $e_{abs}^2$  increases with increasing TKE.

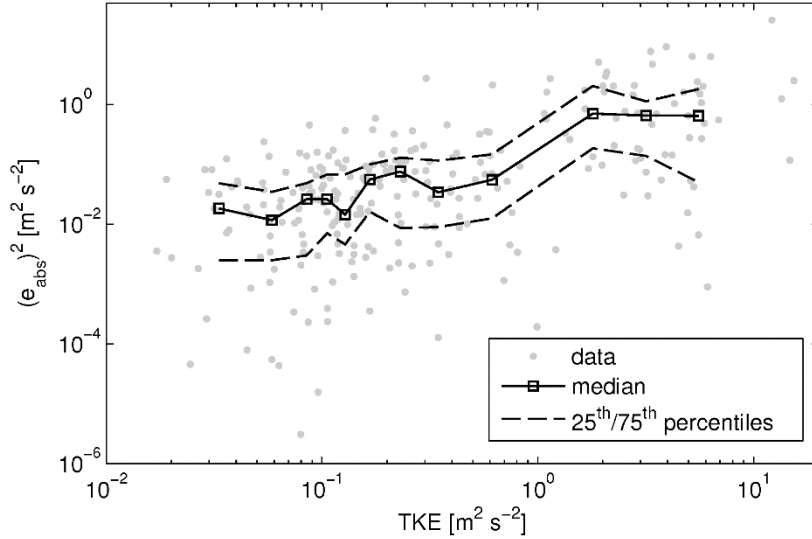


Figure 2-7 Relationship between the squared lidar wind speed error  $[(e_{abs})^2]$  at range gate 11 and the TKE derived from the sonic anemometer at 74 m height on M5. The medians and 25<sup>th</sup> and 75<sup>th</sup> percentiles were calculated for 12 TKE bins that had the same sample number in each bin.

### WLS and error

The number of measurements used to calculate the mean radial velocity varies as the result of data selection procedure described in section 2.3.2. The lowest number is 13. Lowering sample number can increase uncertainty in the estimated mean. However, the increased uncertainty is accounted for by WLS, because the weight given to a mean radial velocity is inversely proportional to its variance. Therefore, the number of samples used to calculate the mean radial velocity should have little effect on the accuracy of the estimated wind speed. Nevertheless, WLS instability can arise when mean radial velocities are missing or excluded at some azimuth angles. Reducing the

number of mean radial velocities in WLS can increase the model matrix *cond* number  $K(\mathbf{G})$  and inversion instability (see Figure 2-7 in which retrieved wind speeds with high  $K(\mathbf{G})$  and missing mean radial velocities are marked by red dots and dark diamonds, respectively). These estimates in general have large errors at high wind speeds, but their errors are relatively small at low wind speeds. Note that some observations with high  $K(\mathbf{G})$  still have small errors when TKE is small ( $< 0.25 \text{ m}^2 \text{ s}^{-2}$ ). Thus, even though errors in the estimated wind speed are amplified by large *cond* numbers, they can still be low as the result of small variance of the mean radial velocities.

### **Inhomogeneity and error**

A violation of the assumption of homogeneity is another source of error. Winds can become horizontally nonuniform because of their interactions with the complex topographical features around the site. As described above, a threshold  $R^2$  value of 0.8 was used to detect estimates possibly related to high spatial variability, and this removes 74 or 22.5% of 328 records that had matching sonic measurements within the free-stream sector. Increasing the threshold value (to 0.9) can improve data quality to some extent. The points with blue squares in Figure 2-7 are those with  $0.8 \leq R^2 \leq 0.9$ . The relative RMSE for those points is 52%, which is much higher than 16.1% for the rest of points with  $R^2 > 0.9$ .

To further investigate the effects of nonuniform flow on errors, measurements from the sonic anemometer were converted to radial velocities (denoted as  $v_{R0,s}$ ) and their mean and variance (denoted as  $\langle v_{R,s}'^2 \rangle$ ) at the 7 azimuth angles using Eq. (2.5) and Eq. (2.7), respectively. Then  $v_{R0,s}$  was compared with its concurrent lidar-measured radial velocities (denoted as  $v_{R0,l}$ ). If the flow was uniform, then the difference between  $v_{R0,s}$

and  $v_{R0,l}$  should be within a range defined by  $\langle v'_{R,s}{}^2 \rangle$ . Statistical tests were conducted for all of the  $v_{R0,l}$  against normal distributions with their means and standard deviations defined by  $v_{R0,s}$  and  $\langle v'_{R,s}{}^2 \rangle$ , respectively; and  $N_d$  was used to denote the number of azimuth angles at which  $v_{R0,l}$  are significantly different from  $v_{R0,s}$ . Figure 2-8 shows the relationship between  $e_{rlv}$  and  $N_d$ . Errors were large when  $N_d = 2-4$ , because of the existence of nonuniform flows (see example in Figure 2-9). Wind speed for these cases varied monotonically with azimuth angle, and measured radial velocities can fit Eq. (2.5) very well. However, the fitted coefficients gave incorrect estimates of wind speed, because of the consistent spatial variability pulled the sinusoidal curve of Eq. (2.5) in a wrong direction. If the difference between  $v_{R0,s}$  and  $v_{R0,l}$  was fitted as a linear function of the azimuth angle, statistically significant large slopes were found for cases for which  $N_d = 2-4$  (Figure 2-8). When  $N_d < 1$ , flow was uniform and errors of the retrieved wind speeds were minimal. When  $N_d = 7$ , all of the  $v_{R0,l}$  were different from  $v_{R0,s}$ ; however, the error of the estimated wind speed was small. This outcome is possible if a spatial gradient of wind speed only exists between the sonic anemometer location and the arc scanned by the lidar but not along the arc. The retrieved wind speed represents the uniform wind field along the arc. As long as the spatial variability is small across the small distance between the arc and the sonic anemometer, the error of the retrieved wind speed should be small.

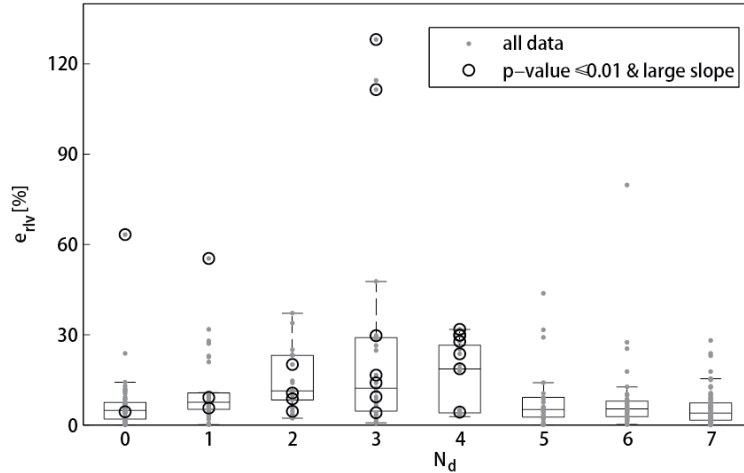


Figure 2-8 Boxplots of relative errors ( $e_{rlv}$ ) of all retrieved lidar wind speeds grouped according to the number ( $N_d$ ) of measured mean radial velocity that was significantly different from the radial velocity estimated from sonic measurements. If the difference between the mean radial velocity from the lidar and the sonic showed a significant linear relationship with the azimuth angle, the respective data point was marked by a dark circle. The linear relationship was significant if the fitted slope was significantly nonzero (p-value  $\leq 0.01$ ) and larger than the 90<sup>th</sup> percentile of all the fitted slopes.

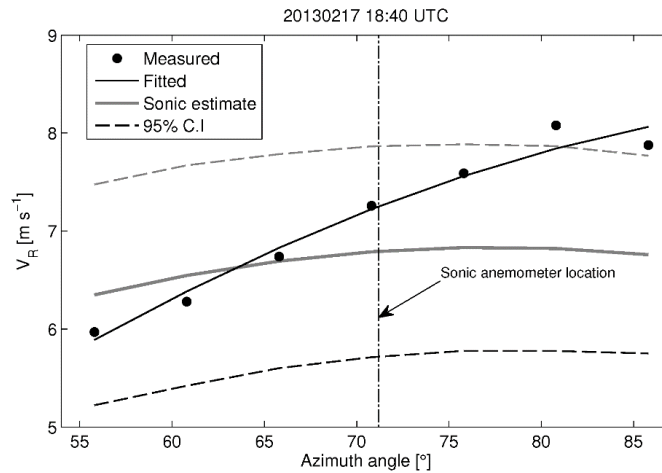


Figure 2-9 A case study showing a comparison between the 10-min mean radial velocities ( $v_R$ ) measured by the lidar (solid circles) and estimated from the sonic measurements (thick gray line) for a range of azimuth angles with an elevation angle = 12.7°. The sonic mean wind speed = 7.13  $m s^{-1}$ , and the wind direction = 257°. The gray dashed lines show the 95% confidence interval for the radial velocity estimated from the sonic based on the turbulence statistics derived from sonic measurements. Lidar measurements fit Eq. (2.5) very well (as shown by the dark line), but the estimated wind speed (8.69  $m s^{-1}$ ) overestimates the sonic wind speed by 22%.

### Approaches to quantify uncertainties in $V_{lidar}$

As discussed above, uncertainty in  $V_{lidar}$  is proportional to turbulent wind fluctuation and, thus TKE can be used to identify  $V_{lidar}$  values that have high associated uncertainty and even to quantify part of the uncertainty in  $V_{lidar}$ . TKE can be estimated from direct lidar measurements when radial velocity variance is available from at least six azimuth angles (Sathe and Mann 2012a). However, this estimation is not possible for the arc scan covering a small azimuth range, because the model matrix has a high *cond* number. An alternative method is to approximate TKE from Eq. (2.7) under the assumption of isotropic turbulence. Then all the covariance terms in Eq. (2.7) become zero and the variance terms have the same value. As a result, radial velocity variance is equal to two thirds of TKE—that is,

$$\langle v_R'^2 \rangle = \frac{2}{3} TKE \quad (2.25)$$

Note that in the analysis the lidar measurement error term  $\sigma_\epsilon^2$  was neglected, as was attenuation of TKE by the volumetric averaging of the lidar measurement. Nevertheless, as shown in Eq. (2.25) is consistent with the fitted relationship between the  $\langle v_R'^2 \rangle$  measured by the lidar and the TKE measured by the sonic anemometer, which has a slope of  $0.630 \pm 0.012$ , which is very close to two-thirds.

Screening of  $V_{lidar}$  using an arbitrary threshold of the 30<sup>th</sup> highest  $\langle v_R'^2 \rangle$  value (as a proxy for high TKE) can improve the quality of the linear fit between  $V_{lidar}$  and  $V_{sonic}$  (Figure 2-11), although it should be noted that removing data with high  $\langle v_R'^2 \rangle$  actually removed some data with high wind speeds, because TKE is dependent on and proportional to wind speed.

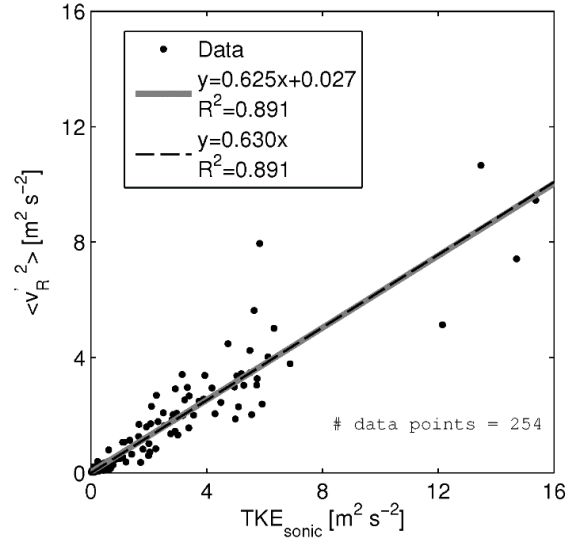


Figure 2-10 Relationship between 10-min mean values of TKE derived from the sonic measurements and the radial velocity variance ( $\langle v_R'^2 \rangle$ ) from the lidar measurements. Also shown are linear fits to these data with and without intercept.

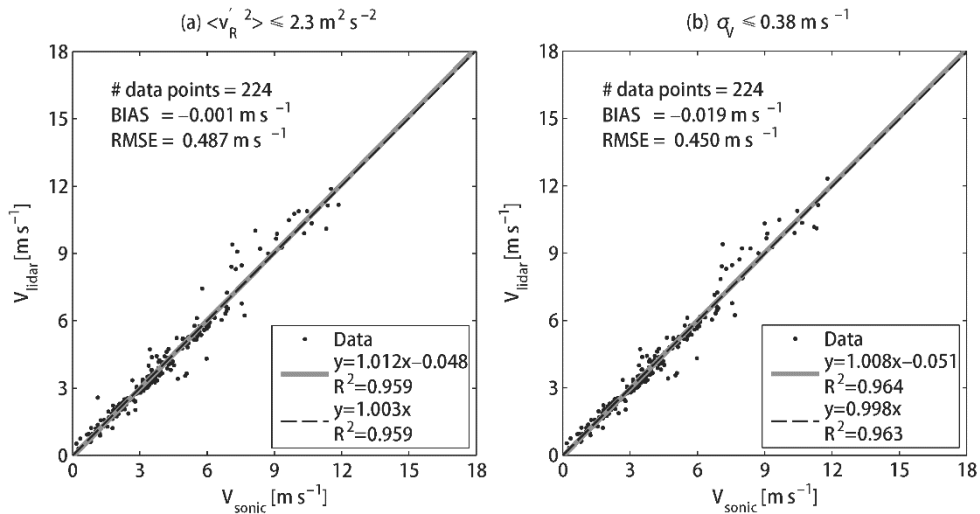


Figure 2-11 Relationship between the sonic mean wind speed ( $V_{sonic}$ ) and the lidar mean wind speed ( $V_{lidar}$ ) for the data from Figure 2-6 with (a)  $\langle v_R'^2 \rangle \leq 2.3 \text{ m}^2 \text{ s}^{-2}$  and (b)  $\sigma_v \leq 0.38 \text{ m s}^{-1}$ , which excluded data with the top 30% of high  $\langle v_R'^2 \rangle$  and  $\sigma_v$ , respectively.

The standard error  $\sigma_v$  defined in Eq. (2.19) can also be used to quantify the uncertainty in  $V_{lidar}$  estimates, because it is a function of both turbulent wind

fluctuation and WLS instability. As shown in,  $V_{sonic}$  is within the 95% confidence interval on  $V_{lidar}$  as described using  $\sigma_V$  for most of cases, suggesting  $\sigma_V$  could be used for uncertainty quantification. The large discrepancies seen in the wind direction sector  $210^\circ$ - $270^\circ$  were associated with nonuniform flows (as shown in Figure 2-9). As in the analysis where the highest 30 values of  $\langle v_R'^2 \rangle$  were excluded, if the 30 measurements with the highest  $\sigma_V$  were excluded, again improvement was made for both the fitted linear model and the error statistics (Figure 2-11). The analysis summarized in Figure 2-11 suggests that  $\sigma_V$  might be a better parameter than  $\langle v_R'^2 \rangle$  for quality control.

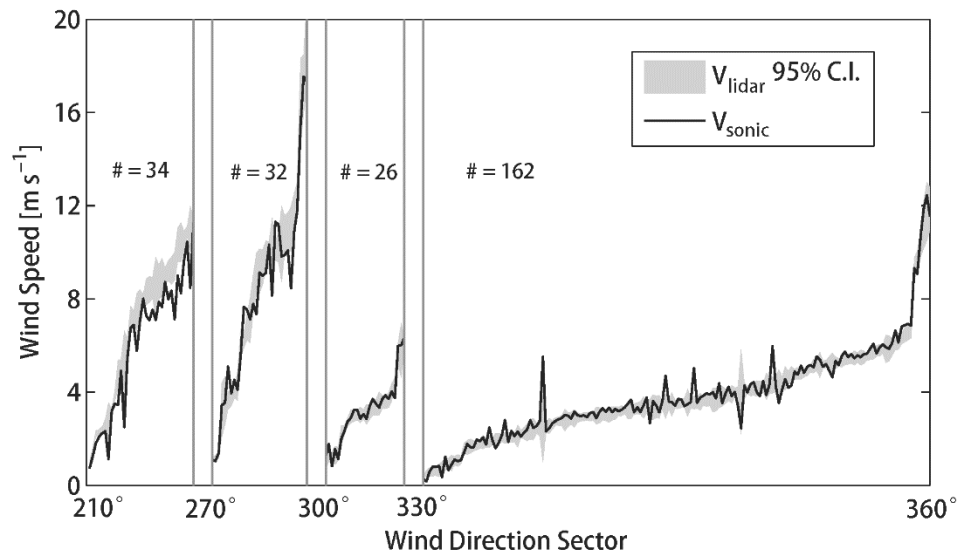


Figure 2-12 Comparison of the lidar mean wind speed ( $V_{lidar}$ ) and the sonic mean wind speed ( $V_{sonic}$ ) in four wind direction sectors:  $210^\circ$ - $270^\circ$ ,  $270^\circ$ - $300^\circ$ ,  $300^\circ$ - $330^\circ$ , and  $330^\circ$ - $360^\circ$ . Data presented here are the same as those presented in Figure 2-6. The wind speed measurements are shown in rank order of the lidar mean wind speed. The 95% confidence interval of the lidar mean wind speed is based on the standard error ( $\sigma_V$ ) calculated using Eq. (2.19).

## 2.5 Mean Wind Direction

Ten minute values of  $D_{sonic}$  (at 74 m) and  $D_{lidar}$  (at 76 m) exhibited some coherence but rather large scatter (Figure 2-13), particularly when  $D_{sonic} < 300^\circ$ . This is consistent with the large  $V_{lidar}$  errors seen in this sector (Figure 2-11) and the scatter was caused by high wind fluctuation and nonuniform flows. The scatter was low for  $D_{sonic} > 300^\circ$ , but  $D_{lidar}$  was biased relative to  $D_{sonic}$  by  $5.2^\circ$  (Figure 2-13). If  $D_{sonic}$  is correct, then this suggests that the lidar was not correctly aligned with the north direction. Note that the offset from true north does not affect accuracy of the retrieved mean wind speed.

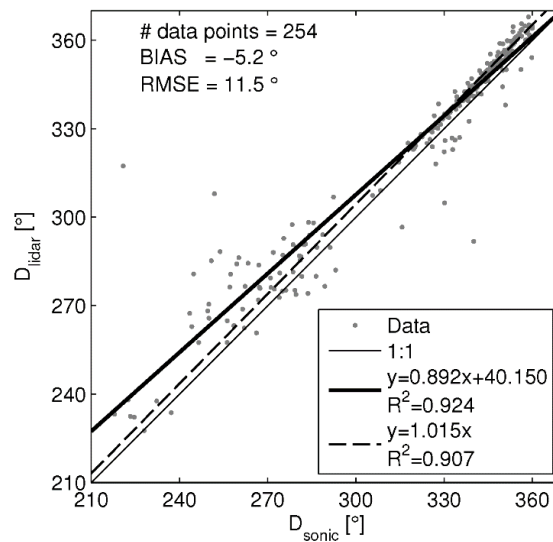


Figure 2-13 Relationship between the 10-min mean wind direction from the lidar range gate 11 ( $D_{lidar}$ ) and sonic anemometer ( $D_{sonic}$ ) at 74 m height on M5 in the free stream sector ( $210^\circ$ – $360^\circ$ ). A value of  $360^\circ$  was added to wind directions from the lidar that are lower than  $90^\circ$  to avoid direction ambiguity around  $0/360^\circ$ .

## 2.6 Vertical Profile of the Horizontal Wind Speed

In the previous discussion, uncertainties in the wind speed and direction retrieved at a specific height (range gate 11) were evaluated using the sonic anemometer

measurements as the reference. Here we evaluate the accuracy of the retrieved wind speed at multiple heights or range gates in terms of vertical profiles of the 10-minute mean horizontal wind speed as measured by the four cup anemometers (up to a height of 80 m) mounted on M5. Only those cases that are presented in Figure 2-6 and all of the data available from range gate 3 to 11 were evaluated. Range gate 2 and 12 were excluded because of their low data availability. The retrieved wind speed had different spatial coverage at different heights due to the scanning geometry. The arc length increased from 55 m at range gate 3 to 180 m at range gate 11. The horizontal and vertical distance between range gate 3 and 11 were 263 m and 60 m, respectively. Wind profiles were analyzed for the wind speed range  $4\text{--}12\text{ m s}^{-1}$  in two wind direction sectors ( $210^\circ\text{--}330^\circ$  and  $330^\circ\text{--}360^\circ$ ) using wind speeds from the cup anemometer at 80 m and wind direction from the sonic anemometer at 74 m. The wind speed range was chosen because it is relevant to wind power production. The data were divided into two wind direction bins to investigate whether the positive bias observed at range gate 11 in the wind direction bin  $210^\circ\text{--}330^\circ$  existed at the other range gates.

For the wind direction sector  $210^\circ\text{--}330^\circ$ , the lidar consistently overestimated wind speeds at all heights (Figure 2-14). The overestimation was likely caused by the spatial inhomogeneity described in the section 2.4.1 and illustrated in Figure 2-9. For the direction sector  $330^\circ\text{--}360^\circ$ , the mean wind speed profile from the lidar and the cup anemometers were almost the same. Moreover, individual wind speed profiles from the cup anemometers and the lidar matched almost exactly. Power-law profiles were fitted to individual lidar wind speed profiles in this direction sector and used to predict wind speed at the heights of the cup anemometers. The predicted wind speed, when compared

with the cup wind speed, has  $\text{BIAS} = -0.075 \text{ m s}^{-1}$  and  $\text{RMSE} = 0.222 \text{ m s}^{-1}$  at 55 m and  $\text{BIAS} = -0.033 \text{ m s}^{-1}$  and  $\text{RMSE} = 0.270 \text{ m s}^{-1}$  at 80 m.

According to Eq. (2.5) and Eq. (2.7), radial velocity measurements from orthogonal scans should have large uncertainty. Although it is not possible to make any generalizable conclusions about the accuracy for orthogonal scans from only 254 measurements, note that the lidar measurements in the directional sector  $330^\circ\text{--}360^\circ$  where the wind direction was perpendicular to one of the lines of sight, exhibited good agreement with the cup anemometer measurements (Figure 2-14), possibly as the result of low turbulent wind fluctuation in this directional sector.

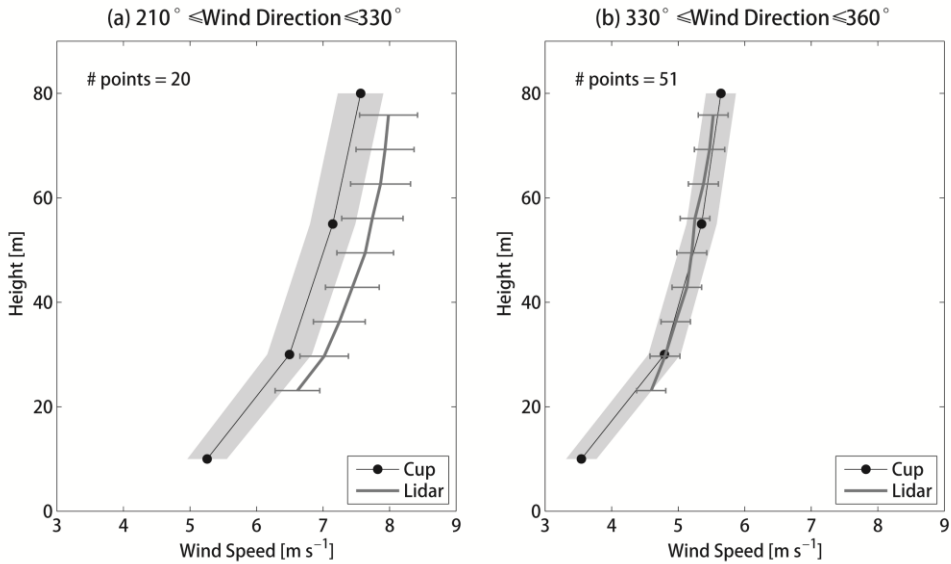


Figure 2-14 Mean vertical profiles of the 10-min mean wind speed retrieved from the lidar and measured by the cup anemometers on M5 for wind direction sector (a)  $210^\circ\text{--}330^\circ$  and (b)  $330^\circ\text{--}360^\circ$ . Only wind speeds of 4-12  $\text{m s}^{-1}$  as measured by the cup anemometer at 80 m height were included. Wind direction was defined by measurements from the sonic measurement at 74 m height. Standard errors of the mean values for the lidar profiles and the cup profiles are plotted as error bars and shaded areas, respectively.

### 2.7 Practical Issues and Guidelines for Arc Scans

For homogenous and stationary wind field, turbulent wind fluctuation is the main source

of uncertainty in retrievals of wind velocities from arc scans. The relationship between wind speed variance and uncertainty in the retrieved wind speed is determined by the following three variables: 1) the azimuth range of the arc scan  $\theta_s$ , 2) the azimuth resolution  $\Delta\theta$ , and 3) the elevation angle  $\phi$ . Both  $\theta_s$  and  $\Delta\theta$  define the number of azimuth angles ( $N_\theta$ ) per arc scan and the sample number ( $n_{10}$ ) at each azimuth angle in a 10-min period. The combination of the three variables needs to be optimized to minimize uncertainty.

Before an optimization is made, it is important to acknowledge that the vertical wind speed cannot simultaneously be retrieved without degradation of the retrieval accuracy of the horizontal wind components; hence, it must be assumed to be zero for the arc scan. Neglecting the vertical wind speed introduces bias in the estimated  $V_{lidar}$ , but the bias is much smaller than the level of uncertainty introduced by including the vertical wind speed in Eq. (2.A7). As shown in , for  $\theta_s = 30^\circ$  and  $\Delta\theta = 5^\circ$ , assuming  $w_0 = 0$  reduces uncertainty in the estimated  $V_{lidar}$  by approximately 80 times relative to the alternative while it introduces only  $1 \text{ m s}^{-1}$  bias if the actual  $w_0 = 1 \text{ m s}^{-1}$ , and less if  $w_0 < 1 \text{ m s}^{-1}$ . To reduce the bias in the estimated  $V_{lidar}$ , it is advisable to use the mean radial velocity for wind velocity retrieval, because  $w_0$  is more likely to  $\rightarrow 0$  than any instantaneous value. Otherwise, bias in the estimated  $V_{lidar}$  can be inflated because of variation in the vertical wind speed and the non-linear relationship between the scalar wind speed and the wind vector. If  $w_0$  is high, such as it is sometimes at the NWTC, then it might be beneficial to add a vertical scan to the arc scan in a similar manner to the Doppler Beam Swing (DBS) technique (Werner 2005). The measurement of  $w_0$  from the vertical scan can then be used to correct the bias in the estimated  $V_{lidar}$ .

The value of  $\theta_s$  determines the effectiveness of the least squares method used for wind velocity retrieval. Uncertainty in the retrieved wind velocity is caused by radial velocity variance and is amplified by matrix inversion instability. Radial velocity variance is determined by the covariance matrix for  $u$ ,  $v$ , and  $w$ , as shown in Eq. (2.A8), and the variation of radial velocity propagates into the retrieved wind speed and can be inflated by a factor defined by  $K(\mathbf{G})$ , as shown in Eq. (2.13). In general,  $K(\mathbf{G})$  and uncertainty in the estimated  $V_{lidar}$  decreases with increasing  $\theta_s$ , assuming isotropic homogenous turbulence (Figure 2-15) (Banakh et al. 1995); hence it is always recommended to use a large  $\theta_s$  while being cognizant that for a given averaging period the value of  $\Delta\theta$  determines the spatial resolution and temporal resolution of the arc scan and  $\theta_s$  and  $\Delta\theta$  dictate the repetition rate at which each range gate is sampled. With a large  $\Delta\theta$ , the spatial resolution decreases, because  $N_\theta$  decreases, but  $n_{10}$  increases at each azimuth angle. As a result, the uncertainty of the mean radial velocity is reduced. Thus, under the assumption of isotropic turbulence, uncertainty in the retrieved wind velocity decreases with increasing  $\Delta\theta$  or decreasing  $N_\theta$  (Figure 2-15). For the same  $\Delta\theta$ , increasing  $\theta_s$  can reduce uncertainty except for low  $\Delta\theta$ . When  $\Delta\theta$  is low (e.g.  $\Delta\theta = 30^\circ$  as shown in Figure 2-15), increasing  $\theta_s$  causes  $n_{10}$  to decrease and the mean radial velocity uncertainty to increase. Consequently, uncertainty in the retrieved wind speed increases with increasing  $\theta_s$ . Whenever possible, it is desirable for  $N_\theta = 5 - 7$ . According to Figure 2-15, uncertainty should be minimized when  $N_\theta = 3$ , but this is not recommended. Arc scans with low  $N_\theta$  are sensitive to the spatial variability of wind speed, because the weight of WLS is too high at each azimuth angle. For  $N_\theta = 3$ , a slight deviation of wind speed at one azimuth angle from the underlying

true wind speed can significantly change the fitted curve defined by Eq. (2.5) and consequently the fitted wind speed. Note that the effect of  $\theta_s$  and  $\Delta\theta$  on the retrieved wind velocity depends on the turbulence length scale (uncertainty  $\propto$  length scale) (Banakh et al. 1995).

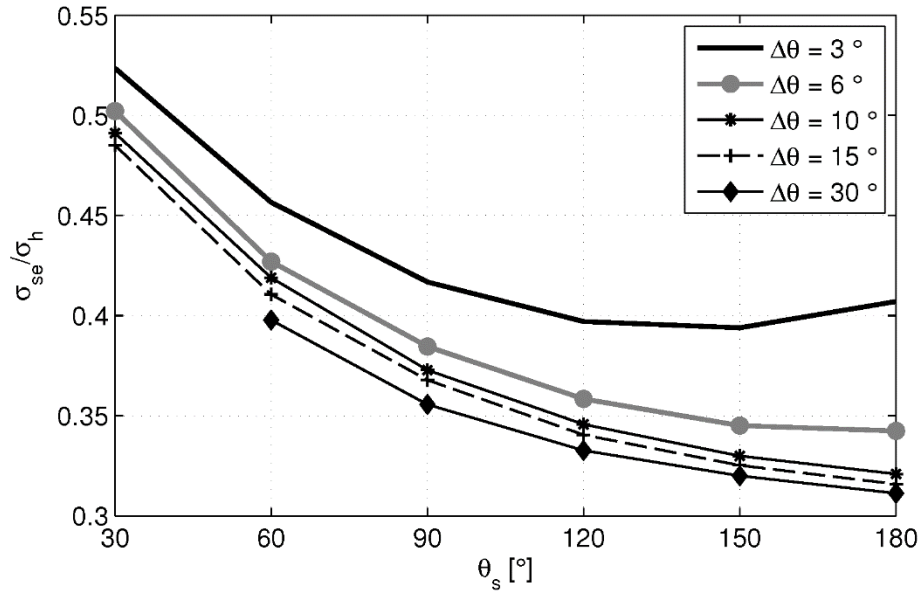


Figure 2-15 Uncertainty in the retrieved wind speed from arc scans as a function of the arc scan azimuth range ( $\theta_s$ ) and the azimuth interval ( $\Delta\theta$ ). The number of beams  $N_\theta = 1 + \theta_s/\Delta\theta$ . Uncertainty is measured by  $\sigma_{se}/\sigma_h$ , where  $\sigma_{se}^2 = \sigma_{u_0}^2 + \sigma_{v_0}^2$  as defined in Eq. (2.19) and  $\sigma_h^2 = \langle u'^2 \rangle + \langle v'^2 \rangle$ . The method used in this analysis is from Banakh et al. (1995) and is described in Eq. (2.A3). Turbulence was assumed to be isotropic, and the turbulence spatial correlation was assumed to decay exponentially. The error in the radial velocity was set to zero by assuming a high return intensity. Wind speed =  $8 \text{ m s}^{-1}$ . Wind direction =  $270^\circ$ . The horizontal wind speed standard deviation =  $1.414 \text{ m s}^{-1}$  as  $\langle u'^2 \rangle = \langle v'^2 \rangle = 1 \text{ m}^2 \text{ s}^{-2}$ . The turbulence length scale = 400 m.

The optimal choice of  $\phi$  depends on the required vertical profile resolution, magnitude of  $w_0$ , and the horizontal extent over which homogeneity is valid. Lowering  $\phi$  can increase the vertical resolution, but it requires a homogeneous wind field over a

large area. The bias because of the assumption of  $w_0 = 0$  is proportional to  $\tan \phi$  as shown in Eq. (2.14); therefore, the bias increases with  $\phi$  for a given combination of azimuth angles. Finally, note that the return signal weakens and therefore data availability decreases as distance increases. To ensure high data availability, it is good practice to focus the laser at the desired range and limit the number of range gates on either side of the focus.

## 2.8 Conclusions

A range of scanning geometries can be used with lidar, but the properties that can be retrieved and the accuracy of the wind speed and direction estimates are complex functions of the inverse method, scanning configurations, and site characteristics, because they determine the flow complexity. Here we evaluate arc scans and conduct an analysis designed to evaluate sources of uncertainty and error in wind speed retrievals using data collected at a site with low complexity in the proximal environment (i.e., with 2 km) but with relatively complex terrain at a distance of 5 km. To stabilize the wind velocity retrieval algorithm as applied to arc scan returns, the vertical wind speed must be neglected. Because the mean vertical wind speed is likely to be zero in most environments, the implication is that the mean radial velocity should be used for the mean wind velocity estimate. Employing an assumption of  $w_0 = 0$  for every 10-min time series at each range gate, outliers and spikes were removed from our experimental time series and the mean and variance of radial velocity were calculated to estimate wind speed and direction using WLS. The resulting wind estimates were compared to those from a collocated sonic anemometer and were found to have a fitted slope for a regression forced through zero of 1.033 and  $\text{RMSE} = 0.72 \text{ m s}^{-1}$  over an observed wind

speed range of up to  $18 \text{ m s}^{-1}$ . Errors in the wind speed retrieved from the arc scan were a function of turbulent wind fluctuation, WLS instability, and the spatial variability of wind speed. The magnitude of the uncertainties resulting from the turbulent wind fluctuations in the sample volume were approximated using the radial velocity variance (as an approximation of turbulence kinetic energy), whereas the uncertainty deriving from both the turbulent wind fluctuation and WLS instability were quantified using the standard error of the retrieved wind speed.

A long-term arc scan measurement campaign over a flat and uniform site with homogeneous and stationary flow is essential to studying the dependence of the arc scan uncertainty on the relative angle between the arc and the wind direction. Further, such a campaign would be useful to characterize the error properties of the wind velocity retrieved from the arc scan and their relationships to turbulence properties and scanning geometry so that an optimal geometry can be chosen for wind energy applications.

## 2.9 Appendix

### 2.9.1 Relationship between radial velocity and wind velocity

The arc scan is set to have  $N$  azimuth angles ( $\theta_n$ ,  $n = 1, 2, \dots, N$ ) with a fixed elevation angle ( $\phi$ ) and repeat  $Q$  times over 10 min. The radial velocity  $v_{Rn}^q$  is the radial velocity measurement from the  $q^{\text{th}}$  scan at  $n^{\text{th}}$  azimuth angle, and it is the projection of wind vector  $\mathbf{v}_n^q = (u_n, v_n, w_n)^T$  on the line of sight, written as

$$v_{Rn}^q = \mathbf{d}_n^T \mathbf{v}_n^q + \varepsilon_n^q \quad (2.A1a)$$

where

$$\mathbf{d}_n^T = [\cos \phi \sin \theta_n, \cos \phi \cos \theta_n, \sin \phi] \quad (2.A1b)$$

and  $\varepsilon_n^q$  is the lidar measurement error. The superscript T denotes the matrix

For homogenous and stationary wind field, two parts comprise the wind vector:

$$\mathbf{v}_n^q = \mathbf{v}_0 + \mathbf{v}_n'^q \quad (2.A2)$$

The term  $\mathbf{v}_0 = [u_0, v_0, w_0]^T$  is the mean wind vector representing a large-scale steady motion and is constant over 10 min. The term  $\mathbf{v}_n'^q = [u_n'^q, v_n'^q, w_n'^q]^T$  is the fluctuating wind vector representing stochastic turbulent motions. It is a random vector with zero mean and covariance matrix  $\Sigma_{v_n}^q$ .

For the radial velocities measured at all of the  $N$  azimuth angles of the  $q^{th}$  scan,

$$\mathbf{v}_R^q = \mathbf{D}\mathbf{v}^q + \boldsymbol{\varepsilon}^q \quad (2.A3)$$

where

$$\mathbf{v}_R^q = [v_{R1}^q, v_{R2}^q, \dots, v_{RN}^q]^T \quad (2.A3a)$$

$$\mathbf{D} = \begin{bmatrix} \mathbf{d}_1^T & \dots & \mathbf{0} \\ \vdots & \ddots & \vdots \\ \mathbf{0} & \dots & \mathbf{d}_N^T \end{bmatrix}_{N \times 3N} \quad \text{and} \quad \mathbf{v}^q = \begin{bmatrix} v_1^q \\ \vdots \\ v_N^q \end{bmatrix}_{3N \times 1} \quad (2.A3b)$$

$$\boldsymbol{\varepsilon}^q = [\varepsilon_1^q, \varepsilon_2^q, \dots, \varepsilon_N^q]^T \quad (2.A3c)$$

In the equation above  $\mathbf{0}$  is the zero vector.

For all the  $Q \times N$  radial velocities ( $\mathbf{v}_R$ ) measured over 10 minutes,

$$\mathbf{v}_R = \mathbf{D}_A \mathbf{v} + \boldsymbol{\varepsilon} \quad (2.A4)$$

$$\mathbf{D}_A = \begin{bmatrix} \mathbf{D} & \dots & \mathbf{0} \\ \vdots & \ddots & \vdots \\ \mathbf{0} & \dots & \mathbf{D} \end{bmatrix}_{NQ \times 3NQ} \quad \text{and} \quad \mathbf{v} = \begin{bmatrix} v^1 \\ \vdots \\ v^Q \end{bmatrix}_{3NQ \times 1} \quad (2.A4a)$$

$$\boldsymbol{\varepsilon}^T = [\boldsymbol{\varepsilon}^{1T} \quad \dots \quad \boldsymbol{\varepsilon}^{QT}]_{1 \times NQ} \quad (2.A4b)$$

According to Eq. (2.A2), the vector  $\mathbf{v}$  in Eq. (2.A4) can be written as

$$\mathbf{v} = \bar{\mathbf{v}} + \mathbf{v}' = \begin{bmatrix} \mathbf{v}_0 \\ \vdots \\ \mathbf{v}_0 \end{bmatrix}_{3NQ \times 1} + \begin{bmatrix} \mathbf{v}'^1 \\ \vdots \\ \mathbf{v}'^M \end{bmatrix}_{3NQ \times 1} \quad (2.A5)$$

Therefore, the vector  $\mathbf{v}$  corresponding to all the measured radial velocities is a random vector with mean  $\bar{\mathbf{v}} = [\mathbf{v}_0^T, \mathbf{v}_0^T, \dots, \mathbf{v}_0^T]_{1 \times 3NM}$  and covariance matrix  $\Sigma_{\mathbf{v}}$  which is determined by the properties of atmospheric turbulence associated with  $\mathbf{v}'$ . Replacing  $\mathbf{v}$  in Eq. (2.A4) with Eq. (2.A5) and applying an averaging operator ( $\mathbf{A}$ ) to both sides of the equation gives

$$\mathbf{v}_{R0} = \mathbf{G}\mathbf{v}_0 + \mathbf{D}_A\mathbf{v}' + \mathbf{A}\boldsymbol{\varepsilon} \quad (2.A6)$$

$$\mathbf{G}^T = [\mathbf{d}_1, \mathbf{d}_2, \dots, \mathbf{d}_N]_{3 \times N} \quad (2.A6a)$$

$$\mathbf{D}_A = \frac{1}{Q} [\mathbf{D}, \mathbf{D}, \dots, \mathbf{D}]_{N \times 3NQ} \quad (2.A6b)$$

$$\mathbf{A} = \frac{1}{Q} [\mathbf{I}_{N \times N}, \mathbf{I}_{N \times N}, \dots, \mathbf{I}_{N \times N}]_{N \times NQ} \quad (2.A6c)$$

The averaging operator, which consists of  $Q$  identity matrices  $\mathbf{I}$ , is used to calculate the mean radial velocities ( $\mathbf{v}_{R0}$ ) at all of the  $N$  azimuth angles. Because  $\mathbf{v}'$  is a random vector with zero mean and covariance  $\Sigma_{\mathbf{v}}$ , the mean radial velocity vector in Eq. (2.A6) is a random vector with mean

$$\langle \mathbf{v}_{R0} \rangle = \mathbf{G}\mathbf{v}_0 \quad (2.A7)$$

and covariance matrix

$$\Sigma_{\mathbf{v}_R} = \mathbf{D}_A \Sigma_{\mathbf{v}} \mathbf{D}_A^T + \mathbf{A} \Sigma_{\boldsymbol{\varepsilon}} \mathbf{A}^T \quad (2.A8)$$

where  $\Sigma_{\boldsymbol{\varepsilon}}$  is the covariance matrix for the lidar measurement errors. If the lidar measurement errors are independent and have equal variance  $\sigma_{\boldsymbol{\varepsilon}}^2$ , the covariance matrix

in Eq. (2.A8) can be written as

$$\boldsymbol{\Sigma}_{v_R} = \mathbf{D}_A \boldsymbol{\Sigma}_v \mathbf{D}_A^T + \frac{\sigma_\varepsilon^2}{Q} \mathbf{I} \quad (2.A9)$$

### 2.9.2 Mean wind velocity estimation

Assuming  $\mathbf{v}$  follows a multivariable normal distribution, the mean wind velocity over 10 min can be estimated from measured radial velocities using the ordinary least squares regression, as follows

$$\widehat{\mathbf{v}}_0 = (\mathbf{G}^T \mathbf{G})^{-1} \mathbf{G}^T \mathbf{v}_{R0} \quad (2.A10)$$

where  $\widehat{\mathbf{v}}_0$  denotes the estimated value of  $\mathbf{v}_0$ . Equation (2.A10) gives an unbiased estimator of  $\mathbf{v}_0$  if the radial velocity is independent and has equal variance; however, this is not true as shown in Eq. (2.A8). As a result, in terms of variance of the estimated wind velocity, the most efficient estimator should be the weighted least squares regression, and  $\widehat{\mathbf{v}}_0$  can be calculated from the following equation (Myers 1990):

$$\widehat{\mathbf{v}}_0 = (\mathbf{G}_w^T \mathbf{G}_w)^{-1} \mathbf{G}_w^T \mathbf{v}_{R0} \quad (2.A11)$$

where

$$\mathbf{G}_w = \mathbf{L} \mathbf{G} \quad (2.A11a)$$

$$\boldsymbol{\Sigma}_{v_R}^{-1} = \mathbf{L}^T \mathbf{L} \quad (2.A11b)$$

In Eq. (2.A11), the weight matrix  $\mathbf{L}$  is related to the covariance matrix  $\boldsymbol{\Sigma}_{v_R}$  through Cholesky decomposition. Assuming measurement errors are independent and have the same variance, the covariance matrix ( $\widehat{\boldsymbol{\Sigma}}_{v_0}$ ) for  $\widehat{\mathbf{v}}_0$  in Eq. (2.A11) is given by

$$\widehat{\boldsymbol{\Sigma}}_{v_0} = [\mathbf{G}^T (\mathbf{D}_A \boldsymbol{\Sigma}_v \mathbf{D}_A^T + \sigma_\varepsilon^2 \mathbf{I} / Q)^{-1} \mathbf{G}]^{-1} \quad (2.A12)$$

If turbulence is isotropic, wind vectors are independent, and measurement errors are negligible, then  $\widehat{\boldsymbol{\Sigma}}_{v_0}$  in Eq. (2.A12) can be simplified into the following equation:

$$\widehat{\boldsymbol{\Sigma}}_{\mathbf{v}_0} = \frac{\sigma^2}{Q} [\mathbf{G}^T (\mathbf{D}\mathbf{D}^T)^{-1} \mathbf{G}]^{-1} \quad (2.A13)$$

where  $\sigma^2$  is the variance for  $u$ ,  $v$  and  $w$ .

For an unbiased estimator, uncertainty in the estimated coefficients is measured by the mean squared error (MSE), which is equal to the trace of the covariance matrix ( $\widehat{\boldsymbol{\Sigma}}_{\mathbf{v}_0}$  for wind velocity retrieval). According to Eqs. (2.A12) and (2.A13), increasing the repetition time  $Q$  reduces MSE. The relationship between  $\widehat{\boldsymbol{\Sigma}}_{\mathbf{v}_0}$  and scanning geometry ( $\mathbf{D}_A$  and  $\mathbf{G}$ ) is non-linear and unpredictable because of the unknown property of turbulence or the value of  $\boldsymbol{\Sigma}_v$ .

### 2.9.3 Wind velocity retrieval uncertainty estimation

If we assume the turbulence is isotropic, then the correlation between two wind components separated by a distance vector  $\mathbf{r}$  can be derived from the following equation (Panofsky and Dutton 1984):

$$\rho_{ij}(\mathbf{r}) = \rho_{11}(r)\delta_{ij} + \frac{1}{2}r \left( \delta_{ij} - \frac{r_i r_j}{r^2} \right) \frac{d}{dr} [\rho_{11}(r)], \quad (2.A14)$$

where  $i = 1, 2, 3$ ,  $j = 1, 2, 3$  and  $u_1$ ,  $u_2$  and  $u_3$  are the streamwise, transverse and vertical wind velocities, respectively. The distance vector  $\mathbf{r} = [r_1, r_2, r_3]^T$  is defined by the distance in the streamwise ( $r_1$ ), the transverse ( $r_2$ ) and the vertical ( $r_3$ ) directions, and it has length  $r$ . The Kronecker delta  $\delta_{ij}=1$  when  $i=j$  and 0 otherwise. The streamwise spatial correlation function  $\rho_{11}(r)$  can be approximated by the exponential decay function, as follows

$$\rho_{11}(r) = \exp\left(-\frac{r}{L_v}\right) \quad (2.A15)$$

where  $L_v$  is the turbulence integral length scale. For the arc scan, measurements at two

range gates are taken at different times and locations and two adjacent measurements at the same range gate are also taken at the different times. The spatial distance between two measurements can be calculated by using the Taylor's hypothesis of frozen turbulence (Stull 1988). Then, each entry in  $\Sigma_v$  can be derived from Eqs. (2.A14) and (2.A15), assuming isotropic turbulence, and  $\widehat{\Sigma}_{v_0}$  and its trace (MSE) can be calculated for a given arc scan scanning geometry.

## CHAPTER 3 LIDAR ARC SCAN UNCERTAINTY REDUCTION THROUGH SCANNING GEOMETRY OPTIMIZATION<sup>2</sup>

### 3.1 Introduction

Coherent Doppler lidars (hereafter called lidars) have been used to probe a range of atmospheric boundary layer (ABL) phenomena, including nocturnal low level jets in the Great Plains (Banta et al. 2008), spatial variability of wind in the marine ABL (Pichugina et al. 2012), structures of the urban ABL (Calhoun et al. 2006; Frehlich et al. 2006) and turbulent properties and flow patterns over complex terrain (Krishnamurthy et al. 2011; Choukulkar et al. 2012). Lidars also have applications in wind energy resource estimation and wake characterization (Banta et al. 2013; Barthelmie et al. 2014) due to their ability to accurately and precisely measure flow structures both in front of and in the wake of a wind turbine (Aitken et al. 2014; Simley et al. 2014) and spatial variability of wind speeds over prospective wind farms (Krishnamurthy et al. 2013).

Lidar measurements usually involve operating the instrument with a scan geometry to acquire radial velocities from at least three directions and estimating wind velocity according to the following equation:

$$v_r(s) = \mathbf{d}^T \mathbf{u} \quad (3.1)$$

where  $\mathbf{d}^T = [\cos \phi \sin \theta, \cos \phi \cos \theta, \sin \phi]$  and  $\mathbf{u}^T = [u, w, w]$ . The radial velocity  $v_r$  is the projection of the wind velocity  $\mathbf{u}$  on the line of sight (LOS) at the location  $\mathbf{s}$

---

<sup>2</sup> Wang, H., R. J. Barthelmie, S. C. Pryor, and G. Brown, 2015: Lidar arc scan uncertainty reduction through scanning geometry optimization, *Atmospheric Measurement Techniques Discussion*, **8**, 10429-10471. doi: 10.5194/amtd-8-10429-2015

$= s\mathbf{d}$  for which  $s$  is the distance from the lidar along the LOS and  $\mathbf{d}$  is unit directional vector determined by the elevation angle  $\phi$  and the azimuth angle  $\theta$  of the LOS from north. The uncertainty or standard error of the estimated wind velocity has great importance to wind energy applications and is a function of the atmospheric turbulence structure and the specific lidar scanning geometry (Banakh et al. 1995). Two common scanning geometries applied in wind energy are the Velocity-Azimuth-Display (VAD) scan and the arc scan. VAD scans apply a full-azimuth conical scan (i.e.  $\theta$  from 0 to  $360^\circ$ ) with a constant elevation angle ( $\phi$ ) and the wind velocity is estimated by solving Eq. (3.1) under the assumption of a horizontally homogeneous wind field. When the assumption is met VAD scans are reliable and well understood and can meet the stringent accuracy requirement for wind energy applications (Gottschall et al. 2012). The arc scan involves  $\phi$  being held constant and  $\theta$  varied to sample a conical sector (e.g. Henke and Clive (2015)). VAD scans are commonly used for wind resource assessment because in homogeneous terrain or under a constant wind gradient the function used to derive the wind velocity should have the smallest errors while arc scans can potentially have large errors if the fit is distorted by a small number of erroneous points. However, arc scans “are less affected by inhomogeneities in the wind field on scales of the scan diameter than are the full circle scans” (Schwiesow et al. 1985). Arc scans have a role, especially if heterogeneous conditions exist, because the scan can be focused on the region of interest. For example, a VAD scan centered at the hub of an operating wind turbine will be affected by inhomogeneity because of the wind turbine wake. If the purpose of measurement is the freestream wind speed, a smaller sector scan or arc scan upwind of the wind turbine can be more suitable than a full conical scan.

Arc scans also have the advantage that by only sampling the area of interest the number of sample repetitions in a given time can be increased, decreasing the statistical uncertainty in solving Eq. (3.1). Use of arc scans adds two additional parameters to the scanning geometry: (1) the arc span (i.e. the width of the scan sector,  $\Delta\theta$ ) and (2) the angle between the center of the arc and the wind direction which is a measure of the orientation of the arc scan and will be called hereafter the relative direction and denoted as  $\beta$ . The selection of these parameters have implications for the accuracy of the retrieved wind speed (Courtney et al. 2014; Wang et al. 2015a). Here we extend prior work on optimizing scan geometry to minimize the uncertainty in the estimated wind speeds. We present a quantitative analysis of the dependence of the retrieved wind speed uncertainty on scanning geometry and turbulence intensity, and provide a tool for use in planning lidar deployments for wind energy applications such as power performance tests. The analysis uses both a theoretical turbulence model and real arc scan measurements from a pulsed lidar deployed in three different geographic locations characterized by different surface roughness and turbulence regimes. We conclude by demonstrating how the wind speed uncertainty from lidar arc scan measurement is propagated to the uncertainty in predicting annual energy production (AEP).

### **3.2 Uncertainty in the Lidar Radial Velocity**

Uncertainties in measured radial velocities from a pulsed lidar (e.g. Sgurr’s Galion lidar from which measurements are presented herein, Table 1) are well characterized (Frehlich and Yadlowsky 1994; Frehlich 1997) and can be described as follows:

$$v_R = v_{R0} + e + \delta \tag{3.2}$$

where  $v_R$  is the measured radial velocity,  $v_{R0}$  is the true radial velocity in the sensing volume,  $\delta$  is the bias due to systematic errors and  $e$  is the random error which has zero mean and variance  $\sigma_e^2$ . The magnitude of  $\sigma_e^2$  is a function of both the signal-to-noise ratio (SNR) and the radial velocity variance ( $\sigma_{v_r}^2$ ) in the sensing volume. The true radial velocity from a range gate is well approximated by the weighted average of radial velocities in the sensing volume as (Frehlich 1997):

$$v_{R0} = \int_0^{\infty} v_r(s)W(r-s)ds \quad (3.3)$$

where  $r$  is the lidar range gate location on the LOS, and  $W(r-s)$  is a weighting function with its peak value at  $r=s$ . Note that we use  $v_r$  to denote a radial velocity at a point location and  $v_R$  a measured (volumetrically averaged) radial velocity.

The precision of  $v_R$  is bounded by the Cramer–Rao Bound (CRB) which is a function of SNR (Pearson and Collier 1999). The relationship between CRB and SNR derived from Eq. (5) in Pearson and Collier (1999), and that estimated from radial velocity measurements using the autocorrelation method from Frehlich (2001) are shown in Figure 3-1 for the Galion lidar. Both show that CRB decreases exponentially with increasing SNR, and for the Galion lidar,  $\sigma_e^2$  has the lower bound of  $0.01 \text{ m}^2 \text{ s}^{-2}$  when  $\text{SNR} > 20 \text{ dB}$ .

The uncertainty in  $v_R$  scales with turbulence intensity because turbulent fluctuations of both wind speed and backscattering particle locations in the sensing volume can broaden the signal spectrum and thus increase the uncertainty in  $v_R$  (Banakh et al. 1995; Frehlich 1997). When the turbulence is sufficiently strong ( $\sigma_{v_r}^2 \geq 0.5w_R$  where  $w_R$  is the spectrum width of lidar signal in velocity space that is  $0.877 \text{ m}$

$s^{-1}$  for the Galion lidar), the random error variance  $\sigma_e^2$  becomes proportional to  $\sigma_{v_r}^2$ . If  $\sigma_{v_r}^2$  is extremely large, the spectrum width will be such that the peak is indistinguishable from the noise and thus the radial velocity selected by an estimator can be any value within the velocity search space ( $\pm 39 \text{ m s}^{-1}$  for the Galion lidar).

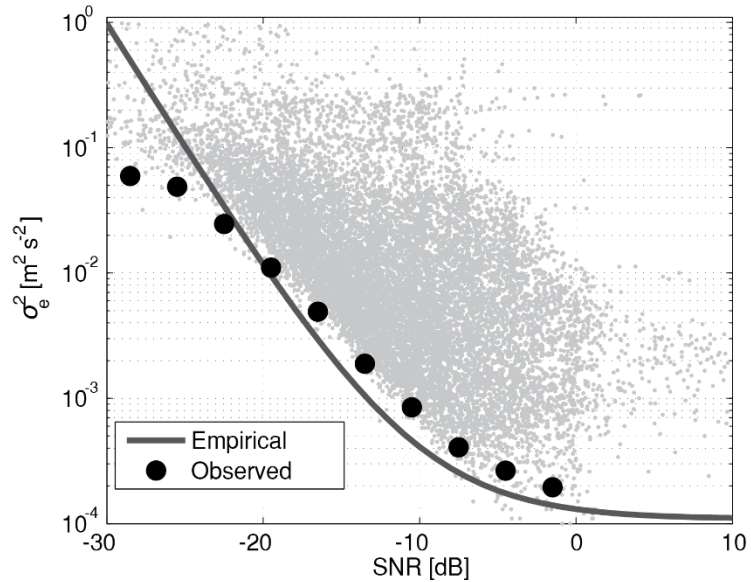


Figure 3-1 The relationship between the signal-to-noise ratio (SNR) and the radial velocity random error variance ( $\sigma_e^2$ ). The gray dots show the observed radial velocity variance approximated by the difference between the variance and the autocovariance at one time lag of the radial velocities collected in an experiment in which the lidar was operated with a staring mode at the US National Renewable Energy Laboratory (Wang et al. 2015a), and the observed Cramer–Rao Bound (CRB) (filled dark circles) is approximated by the mean of the lowest 5% of the gray dots (Frehlich 2001). The empirical relationship between the SNR and the CRB is denoted by the dark solid line and is based on Eq. (5) in Pearson and Collier (1999).

Other sources of error in  $v_R$  include non-linear vertical wind shear which can introduce a bias in radial velocity measurement (Lindelöw et al. 2008), and lidar misalignment which results in incorrect azimuth and elevation angles so the measured radial velocity does not represent the wind field at the intended location. For a well-

secured ground-based lidar pitch (displacement from the horizontal) and roll (i.e. “tilt”) angles can be measured and are usually much lower than  $1^\circ$ , causing negligible errors. The synthesis given above thus indicates that when SNR is reasonably high, the uncertainty in  $v_R$  is small ( $\sigma_e^2 < 0.01 \text{ m}^2 \text{ s}^{-2}$ ), and makes a much smaller contribution to the overall uncertainty in the derived horizontal wind speed than turbulent wind fluctuations in the sampling volume (as shown in the next section). Hence, the uncertainty in  $v_R$  will not be considered further in calculating the uncertainty in the estimated mean wind speed from arc scans.

### **3.3 Uncertainty in Wind Speeds Derived from Lidar Arc Scan Measurements**

As in other Eulerian measurement systems (e.g. a network of anemometers deployed on meteorological masts), a lidar conducting arc scans measures the wind velocity by sampling the wind field with a specified sampling frequency and spatial coverage, but the lidar only measures the radial velocity and wind velocity needs to be estimated using an inverse method applied under certain assumptions about the wind field. When the radial velocity has negligible errors, the uncertainty in the estimated wind velocity is controlled by (1) the spatial statistics of the wind field that determine the variation of, and the correlation between the samples (and hence effective sample size, and the representativeness of the wind field), (2) the scanning geometry that determines the temporal and spatial resolution of the samples and (3) the stability of the inverse method. In this section, we describe how the uncertainty in the estimated mean horizontal wind speed from arc scans (denoted as  $V_l$ ) is related to the characteristics of the wind field and the scanning geometry. The method used follows that of Banakh et al. (1995) which was developed to evaluate the uncertainty of wind velocities estimated from VAD scans.

In a homogeneous and stationary wind field, the covariance between the  $i$ th and  $j$ th radial velocities, which are measured by a lidar at the range gates centered at  $\mathbf{r}_i = r_i \mathbf{d}$  and  $\mathbf{r}_j = r_j \mathbf{d}$ , respectively, is a function of the relative location between these two measurements. With the assumption of frozen turbulence, the relative location between the two measurements is  $\mathbf{p}_{ij} = \mathbf{r}_i - \mathbf{r}_j - \Delta \mathbf{p}_{ij}$  where  $\Delta \mathbf{p}_{ij} = [(i - j)\delta t] \mathbf{u}_0$  is the separation distance induced by the mean wind velocity  $\mathbf{u}_0 = (u_0, v_0, w_0)$  during a time interval  $(i - j)\delta t$ . The covariance between the two radial velocity measurements ( $a_{ij}$ ) then can be written as:

$$a_{ij} = \iint_0^\infty [W(s_i - r_i)W(s_j - r_j)]K_r(\mathbf{q}_{ij})ds_i ds_j \quad (3.4)$$

where  $\mathbf{q}_{ij} = \mathbf{s}_i - \mathbf{s}_j - \Delta \mathbf{p}_{ij}$ . The term  $K_r(\mathbf{q}_{ij})$  is the covariance between the point radial velocities ( $v_r$ ) separated by  $\mathbf{q}_{ij}$  that is related to the covariance matrix  $\mathbf{C}(\mathbf{q}_{ij})$  wind velocities with the same separation distance:

$$K_r(\mathbf{q}_{ij}) = d_i^T \mathbf{C}(\mathbf{q}_{ij}) d_j \quad (3.5)$$

The entries in the covariance matrix  $\mathbf{C}$  are the ensemble variance and covariance between three orthogonal wind components. Note no summation is assumed over repeated indices in Eqs. (3.4) and (3.5). Let  $\mathbf{A}$  denote the covariance matrix for all measured radial velocities within a 10 minute period. The entry of  $\mathbf{A}$  at  $i$ th row and  $j$ th column is defined by Eq. (3.4). For a given scanning geometry, Eqs. (3.4) and (3.5) show that, apart from the atmospheric turbulence structure, the statistics of the measured radial velocities are controlled by the mean wind field because the separation distance  $\Delta \mathbf{p}_{ij}$  or  $\Delta \mathbf{q}_{ij}$  varies with the mean wind speed and direction (as illustrated in Figure 3-2). When the relative direction of the lidar beam  $\beta = 0^\circ/180^\circ$  (westerly/easterly in

Figure 3-2), the samples are located in a rectangular area swept by the wind over the arc. When  $\beta = \pm 90^\circ$  the samples are from a line aligned with the arc. If the scan direction is the same as the wind (i.e.  $\beta = +90^\circ$ ), the samples from one arc scan are clustered and almost from the same location (northerly in Figure 3-2). When  $\beta = -90^\circ$  the locations sampled by one arc are more spatially extended (southerly in Figure 3-2).

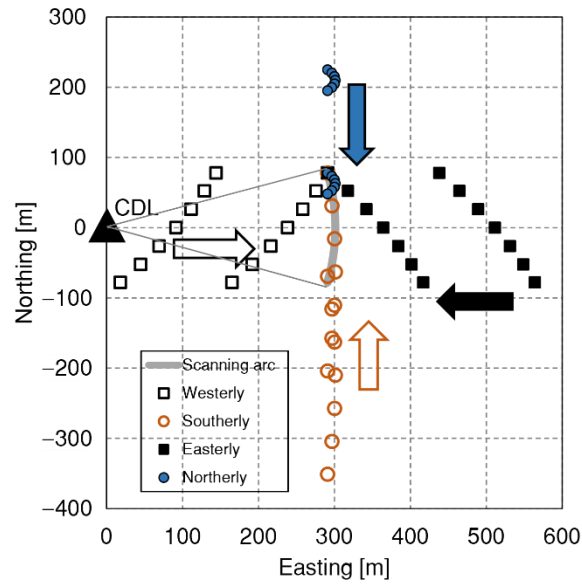


Figure 3-2 An example of the spatial distribution of air parcels sampled in two consecutive arc scans by a lidar at range distance  $s = 315$  m for four different wind directions (westerly, easterly, northerly, and easterly) under the following assumptions: (1) frozen turbulence, (2) the lidar is located at the origin (the dark triangle) scanning from  $\theta = 75^\circ$  to  $105^\circ$  with  $5^\circ$  increments with elevation angle  $\phi = 17^\circ$ , (3) the mean wind speed is  $7 \text{ m s}^{-1}$  and (4) the sampling interval is 3 sec.

The uncertainty in the wind velocity estimated from arc scans can be derived from the covariance matrix  $\mathbf{A}$  of the measured radial velocities. Assuming a horizontally homogeneous wind field with zero mean vertical wind speed (i.e.  $w_0 = 0$ ), the solution of the ordinary least squares ( $V_l$ ) based on Eq. (3.1) is the estimate of horizontal wind velocity (Wang et al. 2015a):

$$\mathbf{V}_l = \mathbf{G}\mathbf{v}_R \quad (3.6)$$

where  $\mathbf{G} = (\mathbf{D}^T\mathbf{D})^{-1}\mathbf{D}^T$  and  $\mathbf{v}_R$  is a vector including  $N$  radial velocities measured in, for example, 10 minutes. The matrix  $\mathbf{D}$  is a  $N \times 2$  matrix with its  $i$ th row given by  $[\cos \phi \sin \theta_i, \cos \phi \cos \theta_i]$ . The estimated wind velocity  $\mathbf{V}_l$  comprises horizontal components,  $\mathbf{V}_l = (u_l, v_l)$ . The uncertainty in  $\mathbf{V}_l$  is characterized by its covariance matrix ( $\mathbf{C}_l$ ) given by:

$$\mathbf{C}_l = \mathbf{G}\mathbf{A}\mathbf{G} \quad (3.7)$$

Assuming zero random error for radial velocity (Wang et al. 2015a). The variance of the random error  $\sigma_e^2$  is  $\sim 0.01 \text{ m}^2 \text{ s}^{-2}$  (see Sect. 3.2) which is much smaller than the diagonal terms of  $\mathbf{A}$  ( $> 0.1 \text{ m}^2 \text{ s}^{-2}$  given wind speed  $> 4 \text{ m s}^{-1}$  and turbulence intensity  $\approx 10\%$ ); therefore, it can be neglected. For most applications, the desired output from arc scans is the horizontal wind speed ( $V_l$ ) that is estimated as:

$$V_l = \sqrt{u_l^2 + v_l^2} \quad (3.8)$$

The uncertainty in  $V_l$  as quantified by the standard error ( $\sigma_l$ ) can be approximated as (Lyons 1991):

$$\sigma_l = [(u_l\sigma_{lu})^2 + (v_l\sigma_{lv})^2 + 2(\rho_{uv}\sigma_{lu}\sigma_{lv})(u_lv_l)]^{0.5}/V_l \quad (3.9)$$

where  $\sigma_{lu}^2$  and  $\sigma_{lv}^2$  represent the variance of  $u_l$  and  $v_l$  and can be found from the diagonal of  $\mathbf{C}_l$ , respectively. The term  $\rho_{uv}$  in Eq. (3.9) is the correlation between  $u_l$  and  $v_l$ , and  $\rho_{uv}\sigma_{lu}\sigma_{lv}$  is the covariance that is given by the only non-diagonal term in  $\mathbf{C}_l$ . The value of  $\sigma_l$  can be estimated from the observational data using Eq. (3.7) with the diagonal terms in  $\mathbf{A}$  being approximated by  $v_R$  variance derived from

measurements and the off-diagonal terms being zero (i.e. assuming no correlation between the measured radial velocities) (Wang et al. 2015a).

### 3.4 Uncertainty Computed from an Isotropic Turbulence Model

Following the background presented in section 3.3 above, the uncertainty in a 10 minute mean wind speed estimated from lidar arc scans is analyzed as a function of (1) turbulence intensity, (2) mean wind speed and direction, and (3) scanning geometry using an isotropic turbulence model. For isotropic turbulence the covariance of the measured radial velocities in Eq. (3.4) can be calculated as follows: the entry at the  $l$ th row and  $k$ th column ( $l, k = 1, 2, 3$ ) of the covariance matrix  $\mathbf{C}(\mathbf{q})$  in Eq. (3.5) is given by the following equation (Monin and Yaglom (1965) cited in (Banakh et al. 1995)):

$$c_{lk}(\mathbf{q}) = c_u(q)\delta_{lk} + \frac{1}{2}q \frac{dc_u}{dq} \left( \delta_{lk} - \frac{q_l q_k}{q^2} \right) \quad (3.10)$$

where  $q = |\mathbf{q}|$ ,  $q_1$ ,  $q_2$  and  $q_3$  are the separation distances in the streamwise, transverse and vertical directions, respectively, and  $\delta_{lk}$  is the Kronecker delta. The streamwise spatial covariance function  $c_u(q)$  can be approximated by the exponential decay function:

$$c_u(q) = \sigma_u^2 \exp\left(-\frac{q}{L_u}\right) \quad (3.11)$$

where  $\sigma_u^2$  is the streamwise velocity variance, and  $L_u$  is the turbulence integral length scale which can be calculated from turbulence intensity ( $\text{TI} = \sigma_u/V_0$ ) in a neutrally stratified atmospheric boundary layer (see Appendix A). Note that Eq. (3.11) misrepresents properties of turbulence of small scales and thus is not consistent with the von Kármán model used to calculate  $L_u$  in Appendix A, but it has similar accuracy to the von Kármán model in predicting the uncertainty of wind speed from conical scans

(Banakh et al. 1995). Thus, Eq. (3.11) is used here for its simplicity and effectiveness. For a given wind speed and direction, the separation distance vector  $\mathbf{q}$  can be from  $\phi$ ,  $\delta\theta$  and  $r$ , and the point radial velocity covariance defined in Eq. (3.5) can be derived from Eqs. (3.10) and (3.11). Then the covariance of the measured radial velocities can be calculated by defining a weighting function in Eq. (3.4). In this analysis the weighting function is approximated by a triangular weighting function defined as:

$$W(r - s) = \max\left[0, \frac{2}{\Delta R} \left(1 - \frac{2}{\Delta R} |r - s|\right)\right] \quad (3.12)$$

where  $\Delta R$  is the spatial extent of  $v_R$  along the LOS, which is a function of the lidar pulse length and hence the illuminated volume at the time of measurement. For the Galion  $\Delta R = 60$  m according to Frehlich (1997) and the lidar parameters in Table 3-1. The radial velocity covariance matrix  $\mathbf{A}$  in Eq. (3.7) is calculated for  $N$  measured radial velocities and used in Eq. (3.9) for calculation of the associated uncertainty in  $V_l$  which is presented here as the relative standard error (abbreviated as lidar RSE and denoted as  $\varepsilon_l$ ) defined as the ratio of the standard error of the estimated mean horizontal wind speed ( $\sigma_l$ ) to the true mean horizontal wind speed ( $V_0$ ):

$$\varepsilon_l = \frac{\sigma_l}{V_0} \quad (3.13)$$

The magnitude of  $\varepsilon_l$  is a function of TI, mean wind speed and direction. Note that  $\varepsilon_l$  is inversely proportional to  $\Delta R/L_u$  which determines the amount of averaging taken for  $v_R$  (see Eq. (3.3)). For a given  $L_u$ , a large  $\Delta R$  implies an average over a bigger area, and therefore less variation in the measured radial velocity and less uncertainty in the estimated wind velocity. Because  $L_u$  is defined as a function of TI and height (see

Appendix A) and only lidar with a constant  $\Delta R$  is investigated here, the dependence of  $\varepsilon_l$  on  $\Delta R/L_u$  is not considered hereafter.

Table 3-1 Galion G4000 Doppler wind lidar specification<sup>1</sup>

Parameter	Value
Wave length	1.56 $\mu\text{m}$
Pulse energy	30 $\mu\text{J}$
Pulse duration <sup>2</sup>	200 ns (30 m)
Range gate size	30 m
Spatial resolution <sup>3</sup>	60 m
Aperture diameter	75 mm
Pulse repetition frequency	20 kHz
Sampling frequency	100 MHz
Dwell time	1 s
Radial velocity accuracy	0.1 $\text{m s}^{-1}$

1. This specification is provided by SgurrEnergy

2. Full width at half maximum

3. Spatial resolution is the sum of the pulse duration and the range gate size (Frehlich 1997).

The relative importance of these functional dependencies and relevance to wind energy applications can be demonstrated using an example in which a lidar is used for a power performance test of a turbine. This type of test is undertaken to determine if the turbine is operating according to the specified power curve (i.e. production of electricity as a function of the inflow wind speed) and thus it involves measurements of the incident flow into the turbine rotor (Wagner et al. 2011). When lidars are used for this purpose they are typically deployed to measure with arc scans at the hub height 2–4 rotor diameters in front of the wind turbine (IEC 2005a). Assuming that the hub height is 90m, the rotor diameter is 90m, and the lidar placed at the base of the turbine is operated with a fixed elevation angle of  $16.7^\circ$  to measure wind velocities 3 rotor diameters in

front of the turbine at hub height (i.e.  $r = 313\text{m}$ ). The arc scan is defined using a span of  $\Delta\theta$  comprising  $M_\theta$  azimuth angles. It takes  $\delta t$  sec to finish one measurement at one azimuth angle and move  $\delta\theta$  to the next azimuth angle, so the sampling intervals are  $\delta t$  in time and  $\delta\theta$  in space. As a result, one arc scan takes  $M_\theta\delta t$  sec and the total number of arc scans conducted in 10 minutes is  $M_{10} = 600/M_\theta\delta t$ . For the power performance test scenario described above typical parameters would be:  $\delta t = 3$  sec,  $\Delta\theta = 30^\circ$  and  $\delta\theta = 6^\circ$ . For reasonable values of TI and  $V_0$ , using the isotropic turbulence model and the definition of the dominant length scale  $L_u$  in Appendix A, RSE ( $\varepsilon_l$ ) shows strongest dependence on TI (Fig. 3a), and increases from about 1.5% for  $V_0 = 7\text{--}9$  m s<sup>-1</sup> at TI= 5% (a low turbulence environment such as might be experienced offshore) to 6–9% for TI > 20% (i.e. a high turbulence environment). RSE also increases with increasing wind speed through its relationship with the variance. The RSE ( $\varepsilon_l$ ) for TI = 12%, for a range of wind speed and relative direction ( $\beta$ ) from -180 to 180°, indicates that under the assumption of isotropic turbulence  $\varepsilon_l$  varies with  $\beta$  but the variation is no more than  $\pm 2\%$  for the range of conditions shown in Figure 3-3b. The relationship shown in Figure 3-3b are expected because the sample locations and resulting spatial correlations between the samples are determined by wind speed and direction (see. Figure 3-2). RSE reaches its minimum at  $\beta = 0$  and  $180^\circ$  and exhibits the lowest dependence on wind speed. The maximum  $\varepsilon_l$  occurs at  $\beta = \pm 45$  and  $\pm 135^\circ$  and exhibits a much stronger dependence on wind speed. When  $\beta = \pm 90^\circ$ ,  $\varepsilon_l$  reaches local minimum and has a relatively large difference between  $\beta = -90^\circ$  and  $\beta = +90^\circ$  because of the different spatial distribution and thus spatial correlation of samples between  $\beta = -90^\circ$  and  $\beta = +90^\circ$  (see Figure 3-2). The effect of scanning geometry on

$\varepsilon_l$  decreases with increasing arc span ( $\Delta\theta$ ) and decreasing beam number (or azimuth angles) per arc scan (Figure 3-4). Enlarging  $\Delta\theta$  increases the spatial coverage, and lowering the number of beams per arc scan increases the separation distance between samples, both of which reduce the correlation between samples and consequently the uncertainty in the estimated horizontal mean wind speed. Additionally, when  $\Delta\theta$  increases and beam number decreases, the condition number of the matrix  $\mathbf{G}$  in Eq. (3.6) decreases and, as a result, the uncertainty introduced by the inverse method (least squares method) decreases (Wang et al. 2015a). The effect of scanning geometry on  $\varepsilon_l$  naturally exhibits a dependence on the relative direction ( $\beta$ ). When the wind direction is parallel to the beams ( $\beta = 0^\circ$ ),  $\varepsilon_l$  is weakly dependent on both arc span and beam number (Figure 3-4a). For example, with a fixed beam number,  $\varepsilon_l$  decreases by only 0.4% when increasing  $\Delta\theta$  from  $30^\circ$  to  $120^\circ$ . When  $\beta = \pm 45^\circ$ ,  $\varepsilon_l$  is less sensitive to beam number than arc span (Figure 3-4b). When  $\beta = \pm 90^\circ$ ,  $\varepsilon_l$  is more sensitive to beam number than arc span (Figure 3-4c and d). Sensitivity is highest when  $\beta = +90^\circ$  and  $\Delta\theta < 60^\circ$ . When  $\beta = +90^\circ$ , there is a band of local minima with  $\varepsilon_l < 4\%$  starting at  $\Delta\theta = 30^\circ$  and beam number 8. The beam numbers and the arc spans associated with those minima are such that the distance between two adjacent azimuth angles is equal to the next one. In other words, under the frozen turbulence assumption the lidar samples the same location repetitively, causing the uncertainty to reduce. The uncertainty in wind speed derived from arc scans naturally causes uncertainty in determining the wind speed corresponding to a power output and consequently uncertainty in the measured power curve. If the power coefficient of the wind turbine is invariant with wind speed, the uncertainty in the measured power curve is  $3\varepsilon_l$  (because wind power is proportional

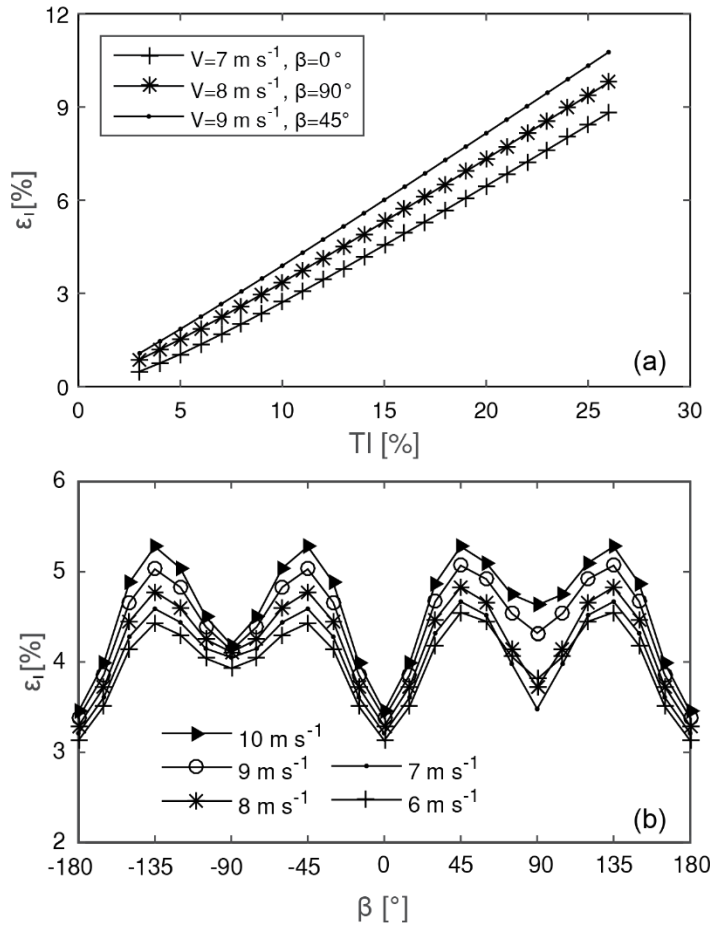


Figure 3-3 Dependence of the relative standard error ( $\epsilon_l$ ) of wind speed estimated from arc scans on (a) turbulence intensity (TI) and (b) wind speed ( $V_0$ ) and direction (expressed as the relative direction ( $\beta$ )) based on the isotropic turbulence model given in Eq. (3.10) for the following scan geometry:  $\phi = 16.7^\circ$ ,  $\Delta\theta = 30^\circ$ ,  $\delta\theta = 6^\circ$  and  $r = 313 \text{ m}$ . The Coriolis parameter  $f_0 = 0.0001 \text{ m s}^{-1}$ .

to the cube of wind speed). Hence, neglecting other sources of uncertainty and error in wind turbine power performance test, such as shear across the swept area (Wagner et al. 2011), the analyses presented above imply that if the lidar beam is well aligned with the incoming “free stream”, the uncertainty in the measured power curve derived from the wind speed measurement by lidar for this example turbine and wind speed of 7–9  $\text{ms}^{-1}$  is about  $\pm 4\%$  for a site with low turbulence intensity (TI = 5%) and  $\pm 20\%$  for a high turbulence intensity environment (TI = 20%). Though these values of uncertainty

resulting from lidar arc scans are similar to the uncertainties in the power curve measured with cup anemometers with the same turbulence characteristics (Wyngaard 2010), using lidar arc scans can eliminate the uncertainty of cup anemometer measurements caused by meteorological mast flow distortion, which has a typical value of  $\pm 1\%$  in wind speed and therefore  $\pm 3\%$  in wind power (IEC 2005a).

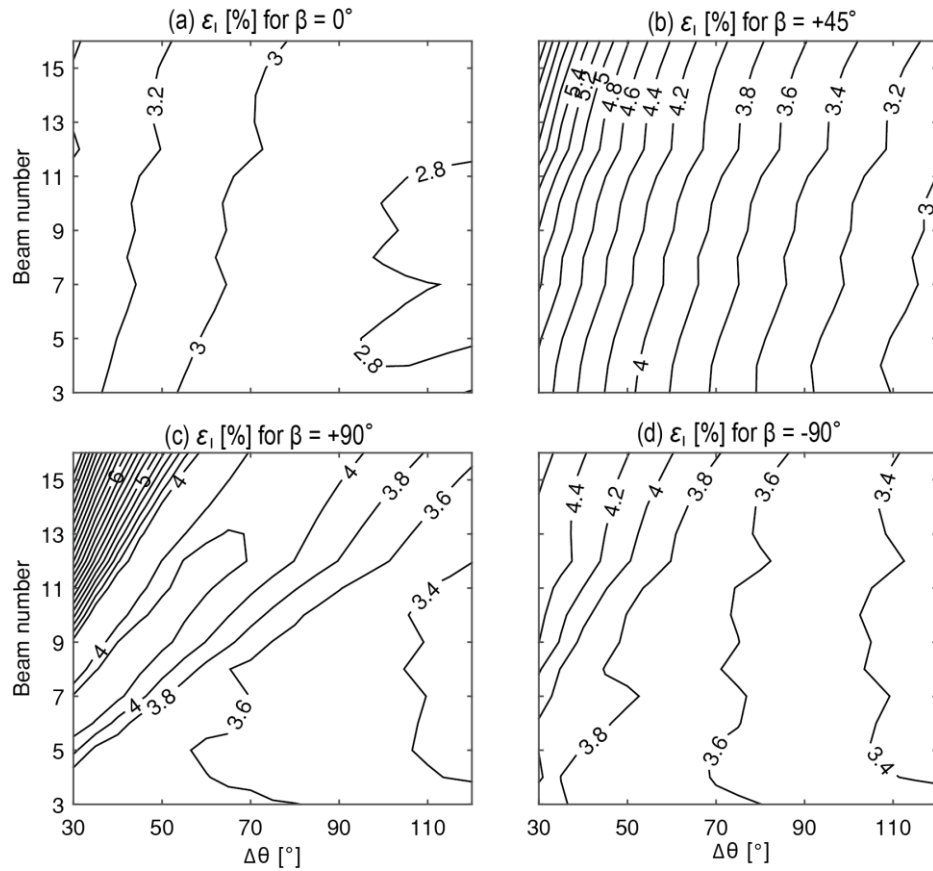


Figure 3-4 Dependence of relative standard error ( $\epsilon_1$ ) of wind speed ( $V_0$ ) on arc span ( $\Delta\theta$ ) and beam number per arc scan for relative directions (a)  $\beta = 0^\circ$ , (b)  $\beta = +45^\circ$ , (c)  $\beta = +90^\circ$ , and (d)  $\beta = -90^\circ$  with  $\phi = 16.7^\circ$  and  $r = 313$  m. The results are calculated for  $V_0 = 7$  m s $^{-1}$  and TI = 12% over a 10 minute period. The Coriolis parameter  $f_0 = 0.0001$  s $^{-1}$ . The contour interval is 0.2%.

### 3.5 Observed Arc Scan Uncertainty

The theoretical uncertainty from the isotropic turbulence model presented in the previous section is a useful tool for decomposing the uncertainty by source, and

potentially to aid in planning lidar scan geometries prior to on-site deployment. It is used here to contextualize empirical analyses of the uncertainty on the mean wind velocity, turbulence statistics and scanning geometry using observational data derived from arc scans at three sites. Site names are not revealed because of confidentiality, but the site characteristics are provided below and the scan geometries are summarized in Figure 3-5. In all cases the analysis is based on the estimated 10 minute horizontal mean wind speed ( $V_l$ ) from the Galion measurements as derived using the ordinary least squares method. The RSE of  $V_l$  will be evaluated through the relative difference ( $e_d$ ) between  $V_l$  and the measurement ( $V_c$ ) from cup anemometers installed on nearby meteorological masts (in compliance with the standard IEC (2005a)):

$$e_d = \frac{V_l - V_c}{V_c} \quad (3.14)$$

Periods with  $V_c < 4 \text{ m s}^{-1}$  or lidar SNR  $< -20 \text{ dB}$  are excluded from the analysis. To quantify the measurement uncertainty, the observed RSE ( $\hat{\epsilon}_d$ ) is defined as the standard deviation of  $e_d$  binned by wind direction or turbulence intensity, and the 95% confidence interval, CI<sub>95</sub>, of  $\hat{\epsilon}_d$  is estimated by (Ahn and Fessler 2003):

$$\text{CI}_{95} = \hat{\epsilon}_d \pm 1.96\hat{\epsilon}_d/\sqrt{2(n-1)} \quad (3.15)$$

where  $n$  is the number of samples in a bin. Note that this definition means that only the spread of values is evaluated and bias is not considered.

The value of  $\hat{\epsilon}_d$  has contributions from random errors related to both instrument and turbulence. The lidar instrument errors are not considered; hence, the expected RSE ( $\epsilon_d$ ) based on the relative difference between lidar and cup anemometer measurements has the following definition:

$$\varepsilon_d^2 = \varepsilon_l^2 + \varepsilon_c^2 - 2\rho_{lc}\varepsilon_l\varepsilon_c + \varepsilon_{cup}^2 \quad (3.16)$$

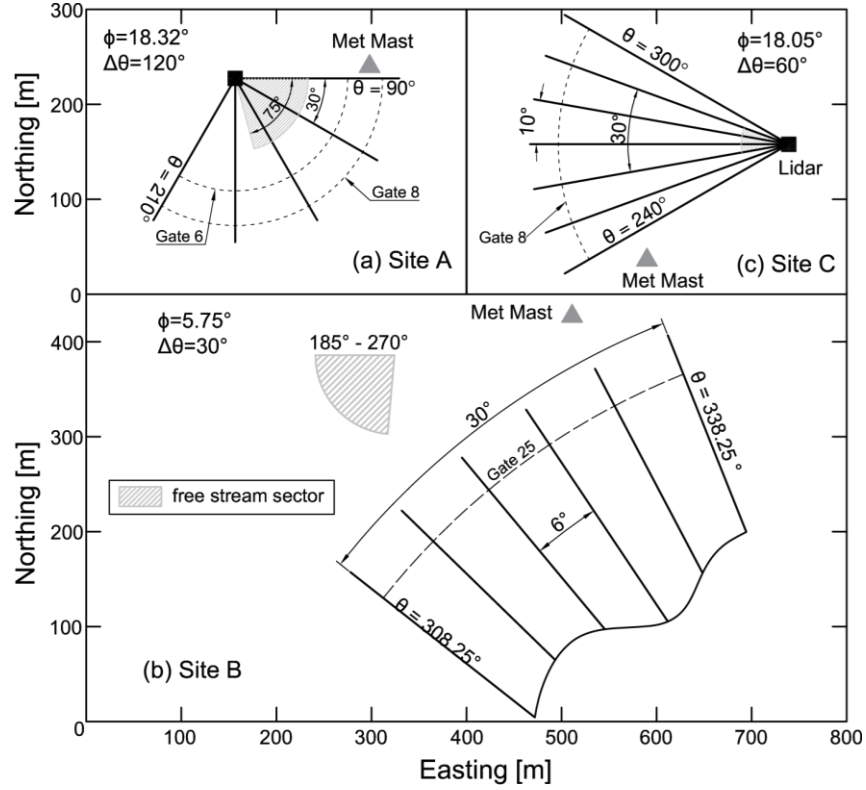


Figure 3-5 Plan views of the scanning geometries used at (a) site A, (b) site B and (c) Site C. The dark squares indicate the lidar locations, and the hatched areas indicate the wind direction sectors without flow distortions. Locations of meteorological masts are denoted by the solid gray circles. The elevation angle ( $\phi$ ) and the arc span ( $\Delta\theta$ ) used at each of the sites are also given.

Terms on the RHS of Eq. (3.16) represent sources of errors and will be estimated as follows in order to differentiate the lidar RSE from the difference between lidar and cup anemometer measurements:

- $\varepsilon_l$  is the lidar RSE due to turbulence defined in Eq. (3.13) that can be estimated with the isotropic turbulence model.
- $\varepsilon_c$  is the cup RSE due to turbulence which is a function of the integral time scale

and the sampling duration (Lenschow et al. 1994). Eq. (13) in Lenschow et al. (1994) will be used to estimate  $\varepsilon_c$  by assuming that the streamwise velocity autocorrelation function decays exponentially. The integral time scale is derived from the integral length scale ( $L_u$ ) in Eq. (A12) and the observed mean wind speed. The sampling duration is 10 minutes.

- $\rho_{lc}$  is the correlation between the turbulence-related errors of lidar and cup anemometers that depends on the spatial structure of turbulence and the distance between cup and lidar measurement locations. Estimating  $\rho_{lc}$  is difficult because lidar measures a volume and cup measures a point (or a line assuming frozen turbulence). A simple approximation is used here to estimate  $\rho_{lc}$ . The separation distance is the distance between the center of an arc and the cup location which are 150 m for both Site A and Site B and 120 m for Site C. The correlation decays exponentially with the same integral scale that is used to estimate  $\varepsilon_l$  and  $\varepsilon_c$  at each site.
- $\varepsilon_{cup}$  is the instrument error that can be found from the following equation:

$$\varepsilon_c = \left(\frac{k}{\sqrt{3}}\right) \cdot \left(\frac{0.05 \text{ m s}^{-1}}{V_0} + 0.005\right) \quad (3.17)$$

where  $k$  is the cup anemometer class number that represents the maximum relative error of a cup anemometer in turbulent wind fields (IEC 2005a; Pedersen et al. 2006). The  $k$  values for cup anemometers used at the three sites are listed in Table 3-2.

Table 3-2 Uncertainty classification of the cup anemometers used at the three sites

Site	Cup Anemometer	IEC Class <sup>1</sup>	Class Number
Site A	NRG 40C	A	2.40 <sup>2</sup>
Site B	Vector L100	A	1.80 <sup>2</sup>
Site C	WindSensor P2546A	B	3.71 <sup>3</sup>

<sup>1</sup> Class A is for sites with flat terrain and Class B is for sites with complex terrain (IEC 2005a).

<sup>2</sup> Pedersen et al. (2006).

<sup>3</sup> Cup anemometer manufacture.

### 3.5.1 Site A

Site A is a wind farm on a flat barren land, approximately 20 km from a coastline and at latitude 27° N. The Galion lidar was operated for 20 days with arc scans centered at  $\theta = 150^\circ$  with  $\Delta\theta = 120^\circ$ ,  $\delta\theta = 30^\circ$  and  $\phi = 18.32^\circ$  (Figure 3-5a). Wind speeds estimated from arc scan measurements at range gate 6 and 8 are evaluated against the concurrent data from cup anemometers installed on booms aligned southwest ( $227^\circ$ ) at 60m height and 80m height on a meteorological mast east of the lidar, respectively (Figure 3-5a). Because of flow distortions from the wind turbines and the meteorological mast, the uncertainty evaluation is conducted only in the wind direction sector 90–165° (based on the wind vane measurement at 77m on the meteorological mast), resulting in 952 and 775 measurements of 10 minute mean wind speeds at 80 and 60m height, respectively, and 100% recovery rate at both heights.

The observed RSE of relative difference ( $\hat{\epsilon}_d$ ) is calculated for 10° bins of  $\beta$  with  $V_c$  between 4 and 16 m s<sup>-1</sup>, and all terms on the RSE of Eq. (3.16) are estimated using the mean and variance of wind speed in each bin. The cup ( $\epsilon_c$ ) and the lidar ( $\epsilon_l$ ) RSE show similar dependence on the relative wind direction (Figure 3-6) which is solely the result of variation of the mean and variance of wind speed with the relative direction. The directional dependence of RSE mentioned in section 3.4 should be negligible

because of the large arc span applied here. The fact that  $\varepsilon_l < \varepsilon_c$  in all direction bins (Figure 3-6) supports the advantage of using large  $\Delta\theta$  for arc scans. A large  $\Delta\theta$  allows averaging over a large area, reducing the random error of mean wind speed. The expected RSE ( $\varepsilon_d$ ), which combines both  $\varepsilon_l$  and  $\varepsilon_c$  based on Eq. (3.16), agrees well with the observed RSE ( $\hat{\varepsilon}_d$ ) except for some overestimation when  $\beta < -20^\circ$  at 80 m height (Figure 3-6). The consistency between  $\hat{\varepsilon}_d$  and  $\varepsilon_d$  at Site A indicates that turbulent wind fluctuations are the main source of uncertainty and those assumptions made in applying the isotropic turbulence model are largely realized.

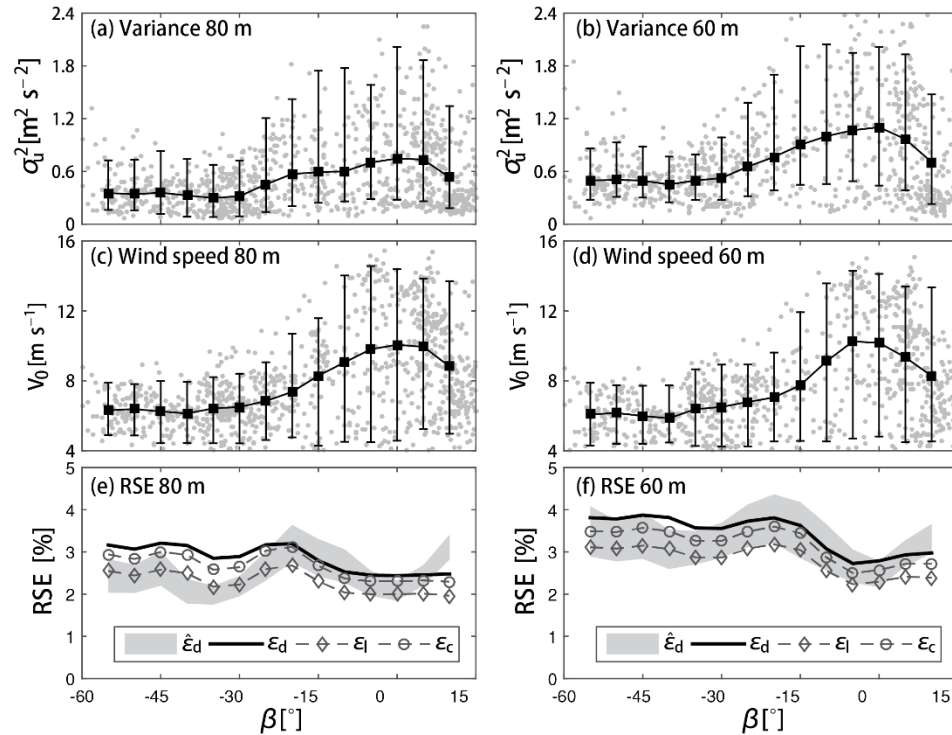


Figure 3-6 Variation of the standard error (RSE) with the relative direction ( $\beta$ ) at Site A at 80 m height in (a, c and e) and 60 m height in (b, d and f). The RSE is given in (e and f) for the 95% confidence interval of the observed difference between the cup and lidar measurements ( $\hat{\varepsilon}_d$ ), the predicted difference between the cup and lidar measurements ( $\varepsilon_d$ ), the predicted cup error ( $\varepsilon_c$ ), and the predicted lidar error ( $\varepsilon_l$ ). The input for the RSE predictions include the mean wind speed ( $V_0$ ) shown in (c and d) and the mean wind speed variance ( $\sigma_u^2$ ) shown in (a and b) for 80 m height and 60 m height, respectively.

### 3.5.2 Site B

Site B is 335 an offshore wind farm at latitude  $54.0^\circ$  N at which the Galion lidar made arc scans for three months centered at  $\Delta\theta = 323.25^\circ$  with  $\Delta\theta = 30^\circ$ ,  $\delta\theta = 6^\circ$  and  $\phi = 5.75^\circ$ . Wind speeds retrieved from range gate 25 are evaluated against concurrent cup anemometer measurements collected on a boom oriented at  $135^\circ$  at 90 m on the meteorological mast north-northwest of the lidar (Figure 3-5b). Observations within a wind direction sector  $185\text{--}270^\circ$  (2954 measurements of 10 minute mean wind speeds with 97% data recovery rate) are used for analysis because of flow distortion from the wind turbines and the meteorological mast in the other sectors.

Data are stratified into two wind speed bins  $8\text{--}12$  and  $12\text{--}16$   $\text{m s}^{-1}$  (based on  $V_c$ ), and are sampled in  $10^\circ$  bins of  $\beta$ . In general there is a good agreement between the observed ( $\hat{\varepsilon}_d$ ) and expected ( $\varepsilon_d$ ) RSE (Figure 3-7). Due to the small arc span applied at Site B,  $\varepsilon_l$  has higher dependence than  $\varepsilon_c$  on the relative direction ( $\beta$ ), and  $\varepsilon_l > \varepsilon_d$  (Figure 3-7). It seems that  $\hat{\varepsilon}_d$  follows  $\varepsilon_l$  when  $\beta$  changes, while  $\varepsilon_c$  has little variation with  $\beta$  (Figure 3-7). The high  $\hat{\varepsilon}_d$  when  $\beta > -70^\circ$  is likely caused by the high values of  $\varepsilon_l$ , although there could be other contributors such as wind turbine wakes and low sample size.

### 3.5.3 Site C

Site C is a wind farm located at latitude  $38.1^\circ$  N in relatively complex terrain. Arc scans were performed over 25 days centered at  $\theta = 270^\circ$  with  $\Delta\theta = 60^\circ$ ,  $\delta\theta = 10^\circ$  and  $\phi = 18.05^\circ$  (Figure 3-5c). Wind speeds retrieved from range gate 8 are evaluated against measurements from a cup anemometer deployed on a boom oriented to  $247.5^\circ$  at 80m on the meteorological mast southwest of the lidar (Figure 3-5c). There is no flow

distortion in the wind direction sector 205–290°. However, because of orographic channeling, 95% of observations are associated with wind directions between 260 and 290°. Thus, this sector, which contains 2167 measurements of 10minute mean wind speed (93% data recovery rate), is chosen for the uncertainty analysis.

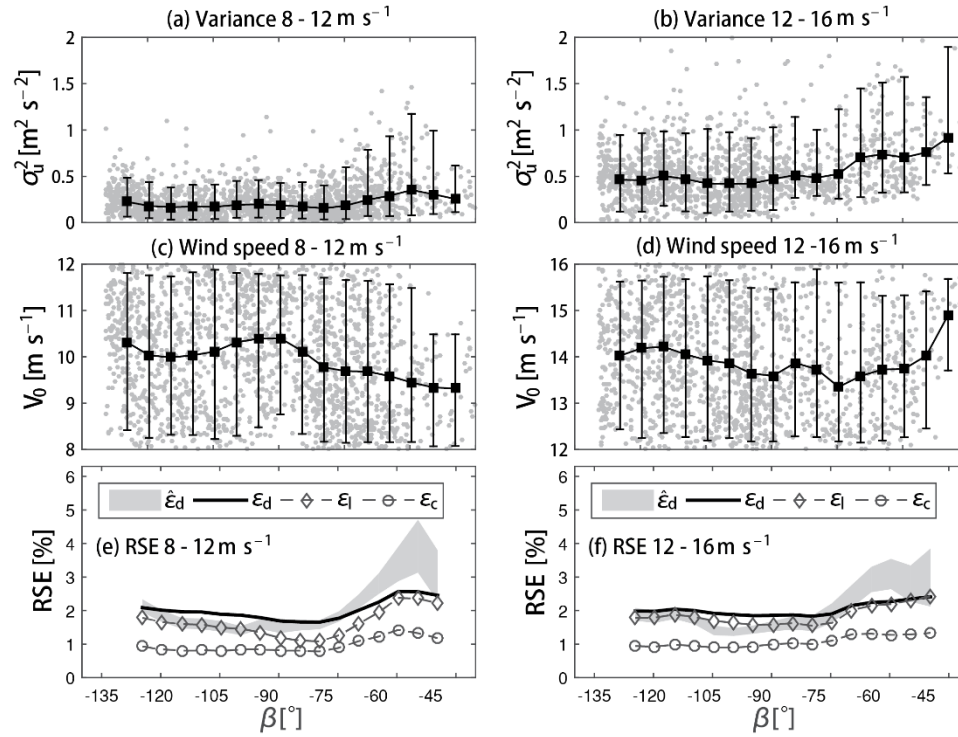


Figure 3-7 Variation of the standard error (RSE) with the relative direction ( $\beta$ ) at Site B for the wind speed bin 8–12  $\text{m s}^{-1}$  in (a, c and e) and the wind speed bin 12–16  $\text{m s}^{-1}$  in (b, d and f). The RSE is given in (e and f) for the 95% confidence interval of the observed difference between the cup and lidar measurements ( $\hat{\epsilon}_d$ ), the predicted difference between the cup and lidar measurements ( $\epsilon_d$ ), the predicted cup error ( $\epsilon_c$ ), and the predicted lidar error ( $\epsilon_l$ ). The input for the RSE predictions include the mean wind speed ( $V_0$ ) shown in (c and d) and the mean wind speed variance ( $\sigma_u^2$ ) shown in (a and b) for the wind speed bin 8–12  $\text{m s}^{-1}$  and 12–16  $\text{m s}^{-1}$ , respectively.

Both observed ( $\hat{\epsilon}_d$ ) and expected ( $\epsilon_d$ ) RSE for 2° bins of  $\beta$  and wind speed between 6 and 14  $\text{m s}^{-1}$  indicate a dependence on wind direction which derives largely from the directional variability of the mean and variance of wind speed (Fig. 8).  $\hat{\epsilon}_d$  increases

from 2% for  $\beta \sim -10^\circ$  to nearly 4% at  $\beta \sim +12^\circ$  in large part due to the decrease in mean wind speed (from 11 to approx. 9  $\text{m s}^{-1}$ ) and increase in variance (from  $< 0.6$  to nearly  $1 \text{ m}^2 \text{ s}^{-2}$ ). Though the agreement between  $\hat{\varepsilon}_d$  and  $\varepsilon_d$  is good, both  $\varepsilon_l$  and  $\varepsilon_c$  are much lower than  $\hat{\varepsilon}_d$ . It is the instrument error of cup ( $\varepsilon_{cup}$ ) that contributes the most to the difference between the lidar and cup measurements. The values of  $\varepsilon_l$  and  $\varepsilon_c$  are very close. Note that  $\varepsilon_l$  and  $\varepsilon_c$  should be lower than the actual values because non-homogeneous horizontal wind fields and non-zero vertical wind speeds over complex terrain violate assumptions in the theoretical models (Bingöl et al. 2009).

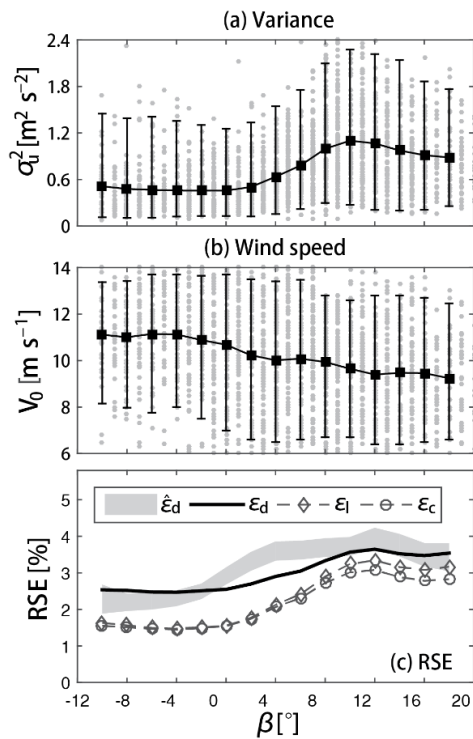


Figure 3-8 Variation of the standard error (RSE) with the relative direction ( $\beta$ ) at Site C at 80 m height. The RSE is given in (c) for the 95% confidence interval of the observed difference between the cup and lidar measurements ( $\hat{\varepsilon}_d$ ), the predicted difference between the cup and lidar measurements ( $\varepsilon_d$ ), the predicted cup error ( $\varepsilon_c$ ), and the predicted lidar error ( $\varepsilon_l$ ). The input for the RSE predictions include the mean wind speed ( $V_0$ ) shown in (b) and the mean wind speed variance ( $\sigma_u^2$ ) shown in (a).

### 3.6 Discussion

The isotropic turbulence model is not a true representation of the turbulent wind field in the atmosphere. The three wind components rarely have equal variance and the same turbulence integral length scale. Further, the exponential decay function is only an approximation of the turbulence autocorrelation function. Nevertheless, the analyses presented above indicate that when properly constrained, the isotropic turbulence model reproduces the uncertainty in wind speed estimated from arc scans with different scanning geometries at different sites, and the predicted relationship between RSE and turbulence intensity is also consistent with the observed relationship (Figure 3-9). The effect of the arc span on the uncertainty of wind speed estimated from arc scans as presented based on the theoretical approach can also be verified by observations after they have been normalized to remove the effect of sample number, turbulence intensity and wind speed on the uncertainty to allow comparison across the sites. Thus the relative errors ( $e_d$ ) are scaled using (Wyngaard 2010):

$$e_{dN} = \frac{e_d}{S_1 \cdot S_2 \cdot S_3} \quad (3.18)$$

where

- $S_1 = (M_{10})^{-1/2}$  represents the relationship between the uncertainty and the sample number  $M_{10}$  used to derive the mean horizontal wind speed.
- $S_2 = TI$  accounts for the fact that the uncertainty scales with turbulence intensity
- $S_3 = V_0 \cdot L_u / 600$  sec represents the spatial coverage of a measurement over 600 sec (10 minutes) relative to the turbulence integral length scale.

The standard deviations of the errors, when  $e_{dN}$  is rescaled back to  $e_d$  with  $V_0 = 9 \text{ m s}^{-1}$ ,  $TI = 12\%$  ( $L_u = 209 \text{ m}$  according to Appendix A) and  $M_{10} = 40$  using Eq. (3.18), are 2.0%, 2.0% and 6.8% after being corrected for  $\varepsilon_c$  and  $\varepsilon_{cup}$  according to Eq. (3.16) for Site A, Site C and Site B, respectively. In other words, the uncertainty increases when  $\Delta\theta$  decreases from  $120^\circ$  at Site A to  $30^\circ$  at Site B, which is consistent with the predicted relationship between  $\Delta\theta$  and RSE given in Figure 3-4. This implies that the approach presented in section 3.3 and 3.4 may be of great use for lidar scan geometry optimization for a given site. Note that the effect of  $\beta$  has not been removed in the rescaling because an overlapping bin of  $\beta$  with a sufficient sample number cannot be found at the three sites; therefore, the rescaling may change if  $\beta$  is considered.

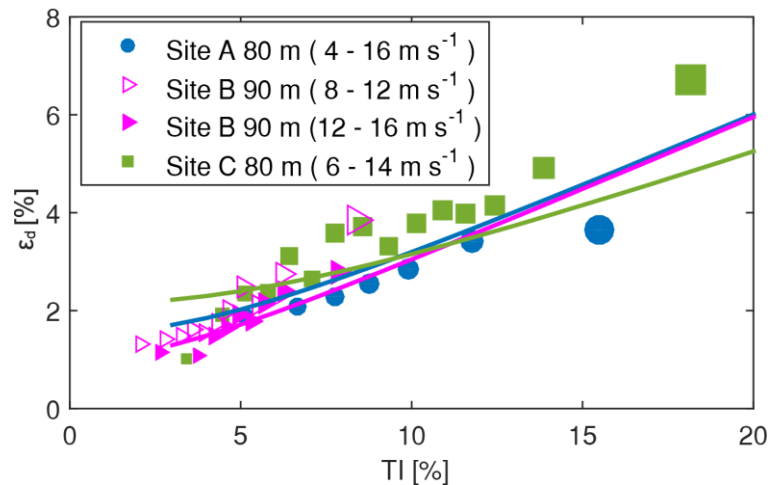


Figure 3-9 The relationship between the RSE of the relative difference between lidar and cup measurements ( $\varepsilon_d$ ) and the turbulence intensity (TI) at the three sites. The 95% confidence interval for each observed RSE ( $\hat{\varepsilon}_d$ ) is denoted by the marker size. The solid lines with matching colors are the predicted relationships at the sites. Prediction at Site A uses wind speed  $8 \text{ m s}^{-1}$  and wind direction  $150^\circ$ , at Site B wind speed  $10 \text{ m s}^{-1}$  and wind direction  $323^\circ$ , and at Site C wind speed  $10 \text{ m s}^{-1}$  and wind direction  $270^\circ$ . Values of  $\varepsilon_d$  here are derived from the cup errors related to turbulence ( $\varepsilon_c$ ) and instrument ( $\varepsilon_{cup}$ ), and the predicted lidar RSE ( $\varepsilon_l$ ) according to Eq. (3.16) and Table 3-2.

### 3.7 Implication for Applications in Wind Energy

If wind speed measurements deriving from arc scans of a lidar are used to predict annual energy production (AEP) at a given site, naturally, the uncertainty in wind speeds will propagate into AEP prediction and contribute to the uncertainty in wind resource assessment. The annual AEP is predicted as follows:

$$E_y = \sum_{j=1}^J \sum_{i=1}^I (T_y F_{V,i} F_{D,j}) P_i \quad (3.19)$$

where  $F_{V,i}$  and  $F_{D,j}$  are the probabilities of the  $i$ th wind speed and  $j$ th wind direction bin, respectively,  $P_i$  is the power production of a wind turbine at wind speed  $V_i$ , and  $T_y$  is the total hours in a year. Assuming statistical independence between lidar measurements, the contribution of the arc scan measurement uncertainty to the uncertainty of  $E_y$  is quantified by the standard error ( $\sigma_y$ ) defined as follows (IEC 2005a):

$$\sigma_y^2 = \sum_{j=1}^J \sum_{i=1}^I (T_y F_{V,i} F_{D,j}) c_i^2 \sigma_{l,ij}^2 \quad (3.20)$$

where  $\sigma_{l,ij}$  is the lidar measurement standard error (see Eq. (3.9)) for the  $i$ th wind speed and  $j$ th wind direction bin, and  $c_i$  is the sensitivity factor determined by:

$$c_i = \left| \frac{P_i - P_{i-1}}{V_i - V_{i-1}} \right| \quad (3.21)$$

A scenario analysis of the resulting uncertainty in AEP prediction is undertaken under the following assumptions: (1) the wind speed follows a Rayleigh distribution with a mean of  $7 \text{ m s}^{-1}$ , (2) the wind direction follows a von Mises distribution with a mean of  $90^\circ$  (see Appendix B for the probability density functions), (3) arc scans

centered at  $\theta = 90^\circ$  with 6 beams, and  $\phi = 15^\circ$ , and (4) the hub-height is 80m. Turbulence intensity and turbulence integral length scale are estimated from surface roughness length using Eqs. (A3) and (A12) in Appendix A, respectively.

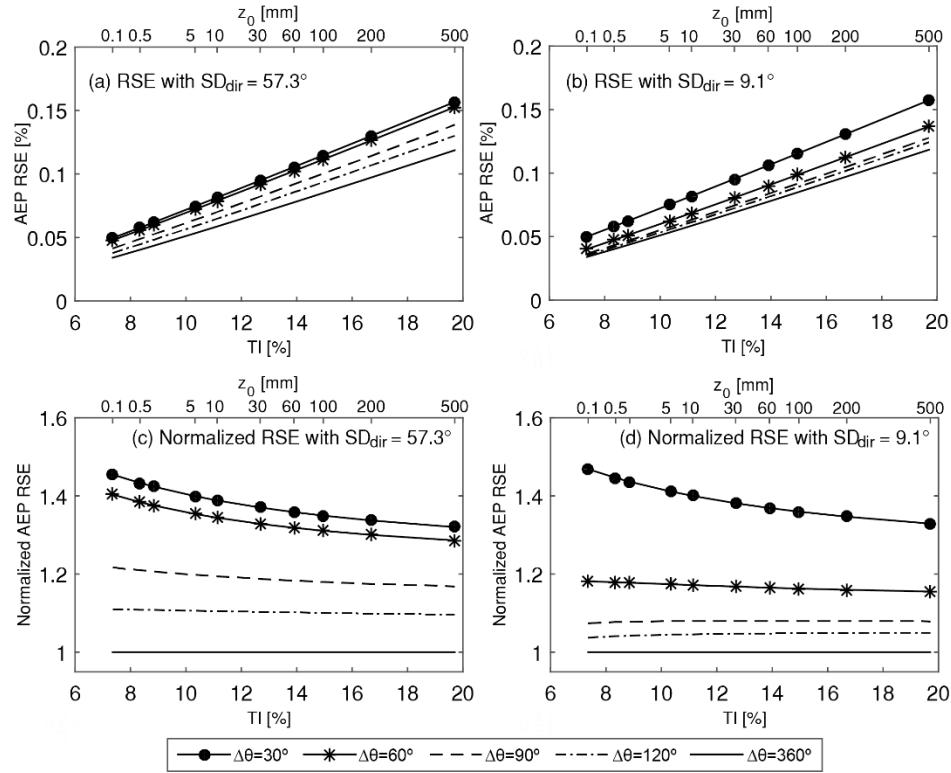


Figure 3-10 The relative standard error (RSE) in annual energy production (AEP) arising from arc scan velocity retrieval uncertainty as a function of turbulence intensity (TI) and surface roughness length ( $z_0$ ), assuming that wind speed follows a Rayleigh distribution with a mean of  $7 \text{ m s}^{-1}$ , and wind direction follows the von Mises distribution with a mean of  $90^\circ$  and standard deviation ( $SD_{dir}$ ) of  $57.3^\circ$  in (a) and  $9.1^\circ$  in (b). Four arc spans and a full azimuth conical scan (see the legend) are used for AEP prediction with six beams,  $\phi = 15^\circ$  and  $r = 315 \text{ m}$ . The normalized AEP RSE, which is the ratio of predicted RSE from arc scans to that from the conical scan, is shown in (c) for  $SD_{dir} = 57.3^\circ$  and in (d) for  $SD_{dir} = 9.1^\circ$ .

The uncertainty in AEP prediction calculated using Eq. (3.20) and a power curve from a commercial wind turbine is shown in Figure 3-10 for different arc spans, wind

direction distributions, and surface roughness length values. Because of the large number of samples used for AEP prediction ( $T_y = 8760$ ), the AEP RSE defined as  $\sigma_y/E_y$  is very low (0.05–0.2%). The uncertainty in AEP increases linearly with TI (and hence  $z_0$ ) and decreases with increasing arc span, but is not sensitive to the wind direction variation. The normalized AEP RSE, which is the ratio of the AEP RSE of arc scans to that of 6-beam conical scan (or  $\Delta\theta = 360^\circ$ ), has the highest value of about 1.4 for  $\Delta\theta = 30^\circ$  (Figure 3-10c and d). Note the uncertainty of conical scan is the minimum value of uncertainty that arc scans can achieve (as a result of  $\Delta\theta \rightarrow 360^\circ$ ).

### **3.8 Conclusions**

Wind speeds measured by lidars are subject to uncertainties that originate from prevailing atmospheric conditions, lidar scanning geometry and wind velocity retrieval method. The analyses presented herein assume horizontal homogeneity and zero mean vertical speed, and thus neglect their roles in dictating optimal lidar operation. The effects of atmospheric turbulence properties and scanning geometry on the uncertainty in the wind speed estimated from lidar arc scans are investigated with both theoretical predictions and actual observations. The theoretical predictions are based on the frozen turbulence hypothesis and an isotropic turbulence model, and the actual observations include arc scan measurements from different scanning geometries both onshore and offshore. The predictions and the observations are consistent, and may be summarized as follows:

- The uncertainty can be scaled with the turbulence intensity
- The lowest uncertainty can be achieved by aligning the line of sight with the wind direction. The highest uncertainty occurs when the wind direction is  $45^\circ$  relative

to the line of sight. There is a local minimum of uncertainty when the line of sight at the center of arc is orthogonal to the wind direction. However, it should be noted that radial velocities measured from orthogonal scans are zero.

- The uncertainty can generally be reduced by increasing arc span and decreasing beam number, although a minimum number of beams is required to characterize the wind velocity. The reduction is most significant when the relative angle between wind direction and line of sight is  $45^\circ$ . If the relative angle is close to zero, adjusting scan geometry will not change the uncertainty significantly. With orthogonal scans, the uncertainty is more sensitive to beam number than arc span.
- When arc scans are used for wind resource assessment, the uncertainty in annual energy production prediction arising from uncertainty in arc scan velocity retrieval is negligible. The uncertainty decreases with decreasing surface roughness and turbulence intensity, and increasing arc span.

The uncertainty estimation approach developed in this paper on the basis of the isotropic turbulence model, though is subject to limits and caveats, is able to predict the effect of wind velocity, turbulence intensity and scan geometry on the arc scan uncertainty at the three sites presented herein. Thus, this approach, although it needs to be further validated by more measurements, may have great utility for a priori optimization of lidar scan geometries for a given site.

### **3.9 Appendix A: Atmospheric Boundary Layer Turbulence Characteristics**

In the neutrally stratified surface layer of the atmospheric boundary layer (ABL), the vertical profile of horizontal wind speed is given by the logarithmic wind profile (Stull

1988):

$$V_0(z) = \frac{u_*}{\kappa} \ln\left(\frac{z}{z_0}\right) \quad (3.A1)$$

where  $u_*$  is the surface friction velocity,  $z_0$  is the surface roughness length,  $\kappa = 0.4$  the von Kármán constant and  $z$  is height above the ground. The standard deviation of the horizontal wind speed ( $\sigma_u$ ) normalized by the friction velocity is a constant, that is,

$$\frac{\sigma_u}{u_*} = c_n \quad (3.A2)$$

where constant  $c_n = 2.5$  (Stull 1988). Hence, according to Eqs. (3.A1) and (3.A2), turbulence intensity, defined as  $TI = \sigma_u/V_0$  can be estimated using the following equation:

$$TI = \frac{c_n \kappa}{\ln(z/z_0)} \quad (3.A3)$$

The turbulence integral length scale is defined as:

$$L_u = \frac{1}{\sigma_u^2} \int_0^{+\infty} c_u(p) dp \quad (3.A4)$$

where  $c_u$  is the spatial covariance function of streamwise velocity. Based on the von Kármán model and the Kolmogorov's 5/3 law, for turbulence with high wave number (e.g. turbulence in the inertial subrange),  $L_u$  in the atmospheric surface layer ( $L_{us}$ ) is defined as:

$$L_{us} = c_1 \frac{\sigma_u^3}{\varepsilon_T} \quad (3.A5)$$

where  $c_1 = 0.7$  (Banakh et al. 1995; Frehlich and Cornman 2002). The turbulence kinetic energy dissipation rate ( $\varepsilon_T$ ) is related to the dimensionless dissipation rate ( $\phi_\varepsilon$ ) via the following equation:

$$\varepsilon_T = \frac{\phi_\varepsilon u_*^3}{\kappa Z} \quad (3.A6)$$

For a neutrally stratified atmosphere  $\phi_\varepsilon = 1$  (Panofsky and Dutton 1984). Thus, combining Eqs. (3.A2), (3.A5) and (3.A6) yields a linear relationship between the turbulence integral length scale and height in the neutrally stratified surface layer:

$$L_{us} = c_1 c_n^3 \kappa Z \quad (3.A7)$$

The actual turbulence integral length scale in the ABL is constrained by the ABL height ( $z_i$ ) and the following equation can be used to account for the effect of  $z_i$  on  $L_u$ :

$$L_u(z) = \frac{L_{us}(z)}{1 + c_2 \frac{L_{us}(z)}{z_i}} \quad (3.A8)$$

where  $c_2 = 2.5$  (Blackadar 1962; Banakh et al. 1995). The height of the neutrally stratified ABL can be determined using the following equation:

$$z_i = c_z \frac{u_*}{f_0} \quad (3.A9)$$

where the coefficient  $c_z = 0.07-0.3$  in the literature (Seibert et al. 2000) and we use  $c_z = 0.3$  in this paper. The term  $f_0$  is the Coriolis parameter and defined as:

$$f_0 = 2\Omega \sin \phi_L \quad (3.A10)$$

where  $\phi_L$  is the latitude and  $\Omega = 7.292 \times 10^{-5} \text{ rad s}^{-1}$  is the angular speed of the Earth.

Combining Eqs. (3.A2), (3.A7) and (3.A8) yields the following formula:

$$L_u = \frac{c_1 c_n^3 \kappa Z}{1 + \frac{\kappa c_1 c_2 c_n^4 f_0 Z}{c_z \sigma_u}} \quad (3.A11)$$

Using the values assigned to these empirical coefficients,  $L_u$  can be calculated using the following equation:

$$L_u = \frac{4.375z\sigma_u}{\sigma_u + 91.146f_0z} \quad (3.A12)$$

### 3.10 Appendix B: Wind Speed and Direction Probability Distributions

The wind speed distribution can be modelled using the Rayleigh distribution with the following probability density function (Forbes et al. 2011):

$$f_V = \frac{2V}{A} \exp\left[-\left(\frac{V}{A}\right)^2\right] \quad (3. B1)$$

where A is the scale factor.

The wind direction distribution can be modelled by the von Mises distribution with the following probability density function (Forbes et al. 2011):

$$f_D = \frac{\exp[b \cos(D - \bar{D})]}{2\pi I_0(b)} \quad (3. B2)$$

where  $D$  is wind direction,  $\bar{D}$  is the mean wind direction,  $b$  is the concentration parameter, and  $I_0(\cdot)$  is the modified Bessel function of the first kind of order zero. The circular standard deviation ( $\sigma_D^2$ ) of the wind direction is then defined as:

$$\sigma_D^2 = 1 - I_1(b)/I_0(b) \quad (3. B3)$$

where  $I_1(\cdot)$  is the modified Bessel function of the first kind of order one.

## CHAPTER 4 ERRORS IN RADIAL VELOCITY VARIANCE FROM DOPPLER WIND LIDAR<sup>3</sup>

### 4.1 Motivations and approach

Coherent Doppler lidars (hereafter called lidars) are increasingly being deployed to measure flow in the atmospheric boundary layer (ABL) particularly for applications to wind engineering (e.g. Banta et al. (2013)). Accordingly, uncertainties in lidar-derived mean wind velocity estimates have been well characterized (Lindelöw 2009; Wang et al. 2015b) and methods and procedures have been developed for error reduction and uncertainty control (Gottschall et al. 2012; Clifton et al. 2013a). However, use of lidar for turbulence measurements, while possible (Mann et al. 2010; Branlard et al. 2013; Newman et al. 2015), is less established (Sathe and Mann 2013; Sathe et al. 2015).

Virtually all approaches for deriving the second order moments of the flow are predicated on the radial velocity variance (Sathe and Mann 2013; Newman et al. 2015). Thus, improved understanding of errors in lidar-derived radial velocity variance estimates is a necessary pre-requisite to development of robust techniques to enable widespread use of lidar for high-fidelity turbulence measurements. Accordingly, the objectives of this work are to improve characterization of the error properties of radial velocity variance and develop tools to reduce these errors. The approach taken and the format of this paper are as follows: The theoretical framework used herein to quantify errors in radial velocity variance from lidar measurements leverages that developed to characterize uncertainties in statistical moments estimated from time series of sonic

---

<sup>3</sup> The work based on this chapter has been submitted to *Atmospheric Measurement Techniques* (AMT-2016-83)

anemometer measurements in Lenschow et al. (1994), and is modified to incorporate the effect of volumetric averaging and the slow sampling rate (section 4.3). The theoretical findings are then compared to empirical estimates obtained from measurements of a Galion lidar and three co-deployed sonic anemometers (section 4.4). The theoretical framework is then used to investigate the sampling duration required to obtain a pre-defined error magnitude (section 4.5).

## 4.2 Preliminaries

A brief description of lidar measurements is given below, for more details see Mann et al. (2008) and Sathe and Mann (2012b).

Denoting a wind velocity vector as:

$$\mathbf{u} = (u_1, u_2, u_3) \quad (4.1)$$

where  $u_1$ ,  $u_2$  and  $u_3$  are streamwise, transverse and vertical wind components respectively at position  $\mathbf{x} = (x_1, x_2, x_3)$ . Without loss of generality, we can assume the mean streamwise velocity  $U_1$  has been removed and  $\mathbf{u}$  are the fluctuating components of turbulence with zero means. A lidar measures the radial velocity ( $v_r$ ) from the Doppler frequency shift induced by the motion of scatterers along the line of sight (LOS), where the orientation of LOS is defined by the unit directional vector:

$$\mathbf{n} = (\cos \phi \sin \theta, \cos \phi \cos \theta, \sin \phi) \quad (4.2)$$

where  $\theta$  is the azimuth angle that increases clockwise from being zero in positive  $x_2$  direction and  $\phi$  is the elevation relative to the  $x_1$ - $x_2$  plane. The radial velocity is the projection of wind velocity on the LOS and is defined as:

$$v_r = \mathbf{n} \cdot \mathbf{u} \quad (4.3)$$

For a pulsed lidar, each radial velocity is measured over a dwell time of approximately 1.0 sec during which spectra from many pulses are averaged to improve the accuracy of measurement. When operated with a scan geometry, the lidar steers its transceiver to probe with different sets of  $\theta$  and  $\phi$ . Hence, the sampling interval of two consecutive measurements at one location depends on the dwell time, the scan geometry, and the mechanical design of the lidar. The shortest sampling interval can be achieved with the staring scan for which the lidar measures with fixed  $\theta$  and  $\phi$ , that is, the sampling interval is equal to the dwell time. Each measured radial velocity ( $v_R$ ) is estimated from an averaged spectrum acquired over a range gate; hence, it is a weighted average of radial velocities along the LOS:

$$v_R(s) = \int_{-\infty}^{+\infty} Q(s') v_r(s - s') ds' \quad (4.4)$$

where  $s$  denotes the range gate location and  $s'$  is the range distance on the LOS. Note that we use  $R$  as the subscript to denote an averaged quantity and  $r$  to denote a point quantity. The weighting function  $Q$  in Eq. (4.4) can be approximated by the Gaussian function (Kristensen et al. 2011):

$$Q(s') = \frac{1}{\sqrt{2\pi}\sigma_Q} \exp\left(-\frac{s'^2}{2\sigma_Q^2}\right) \quad (4.5)$$

where the standard deviation  $\sigma_Q$  is a measure of the size of volumetric averaging, and it is 15.4 m for the Galion lidar used herein (Wang et al. 2015b).

The covariance of  $v_r$  ( $R_r$ ) and  $v_R$  ( $R_R$ ) along the  $x_1$  direction are defined as follows (Mann et al. 2008):

$$R_r(r_1) = n_i n_j R_{ij}(r_1 \mathbf{e}_1) \quad (4.6)$$

$$R_R(r_1) = n_i n_j \int_{-\infty}^{+\infty} \int_{-\infty}^{+\infty} Q(s') Q(s'') R_{ij}((s'' - s') \mathbf{n} + r_1 \mathbf{e}_1) ds' ds'' \quad (4.7)$$

where  $s'$  and  $s''$  denote the range distance,  $R_{ij}$  is the velocity tensor for the  $i$ th and  $j$ th velocity components,  $n_i$  and  $n_j$  are the components of  $\mathbf{n}$ , and  $\mathbf{e}_1$  and  $r_1$  are the unit vector and the separation distance on the  $x_1$  axis, respectively. Note that  $i, j = 2, 3$  and summation is assumed over repeated indices. We can map  $r_1$  to the temporal lag  $\tau$  through the frozen turbulence hypothesis (Taylor 1938);  $r_1 = U_1 \tau$ . The spatial autocorrelation function of  $v_r$  ( $\rho_r$ ) and  $v_R$  ( $\rho_R$ ) separated by  $(r_1, 0, 0)$  are then respectively as

$$\rho_r(r_1) = R_r(r_1) / \mu_{2,r} \quad (4.8)$$

$$\rho_R(r_1) = R_R(r_1) / \mu_{2,R} \quad (4.9)$$

where  $\mu_{2,r} = R_r(0)$  is the variance of  $v_r$  and  $\mu_{2,R} = R_R(0)$  is the variance of  $v_R$ . Due to the averaging given in Eq. (4.4),  $R_R(0) < R_r(0)$  and the ratio  $R_R(0)/R_r(0)$  decreases when the size of volumetric averaging increases (i.e.  $\sigma_Q/L_1$  increases where  $L_1$  is the integral length scale of  $u_1$ ) (Mann et al. 2008). However,  $R_R(r_1) = R_r(r_1)$  when  $r_1$  is sufficiently large (e.g.  $r_1 \gg L_1$ ), because values of  $R_r(r_1)$  with large  $r_1$  are determined by eddies of large sizes that are not affected by the averaging. As illustrated in Figure 4-1 assuming that turbulence is isotropic,  $R_R(r_1)$  starts at a value lower than  $R_r(r_1)$  at  $r_1 = 0$  and gradually converges to  $R_r(r_1)$  as  $r_1$  increases. Because  $R_r(0)$  and  $R_R(0)$  are the denominators in Eqs. (4.8) and (4.9), respectively,  $\rho_R \geq \rho_r$  and  $(\rho_R - \rho_r)$  increase with increasing  $\sigma_Q/L_1$ . As a result, if we denote  $L_r$

and  $L_R$  respectively as the integral length scales for  $v_r$  and  $v_R$ ,  $L_R > L_r$  and increases with increasing  $\sigma_Q/L_1$  (Figure 4-1). Although quantitative evaluation of  $R_R/R_r$  or  $(\rho_R - \rho_r)$  as a function of  $r_1$  requires knowledge of velocity tensors  $R_{ij}$  which is hard to define, the qualitatively statement above is also true for non-isotropic turbulence and has implications on the errors of radial velocity variance estimates as demonstrated in the next section.

### 4.3 Errors in radial velocity variance

In the following, the analysis and notation used are from Lenschow et al. (1994), and we use the word error to refer to the error of radial velocity variance estimated from time series.

Radial velocity variance is estimated from time series of radial velocity that is related to  $\mathbf{u}(t)$  which is a stationary and ergodic time series generated from a Gaussian process characterized by the mean wind speed  $U_1$  and the covariance tensors. Assuming that the mean has been removed from  $\mathbf{u}(t)$ , it can be shown that both  $v_r$  and  $v_R$  are also from a stationary and ergodic time series of a Gaussian process that the following properties:

- Ensemble mean  $\mu_{1,r} = \langle v_r \rangle = 0$  and  $\mu_{1,R} = \langle v_R \rangle = 0$
- Ensemble variance  $\mu_{2,r} = \langle v_r^2 \rangle$  and  $\mu_{2,R} = \langle v_R^2 \rangle$
- Ensemble autocorrelation  $\rho_r(\tau)$  and  $\rho_R(\tau)$

The systematic and random errors are derived in the following for a disjunct time series of  $v_r$ , but the results can be used for  $v_R$ . As discussed in more detail in the subsequent text, the difference between  $v_r$  and  $v_R$  in terms of the relative errors derives solely from the difference between  $\rho_r$  and  $\rho_R$ .

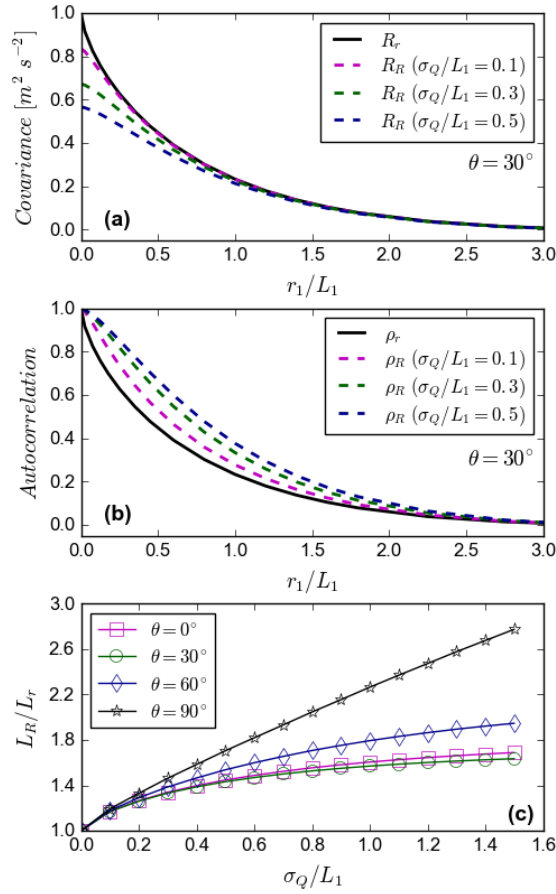


Figure 4-1 Examples of turbulence statistics of point radial velocity ( $v_r$ ) and averaged radial velocity ( $v_R$ ) derived from Eqs. (4.6) and (4.7) with the isotropic turbulence model (Pope 2000) with streamwise velocity  $U_1 = 8 \text{ m s}^{-1}$ , turbulence intensity = 12.5%, and lidar elevation angle =  $10^\circ$ . The covariance and autocorrelation functions for  $v_r$  ( $R_r$  and  $\rho_r$ ) and  $v_R$  ( $R_R$  and  $\rho_R$ ) for azimuth angle  $\theta = 30^\circ$  are shown in (a) and (b), respectively, as functions of  $r_1/L_1$  where  $r_1$  is the spatial lag in streamwise direction and  $L_1$  is the integral length scale of streamwise velocity.  $R_R$  and  $\rho_R$  are presented in terms of  $\sigma_Q/L_1$  where  $\sigma_Q$  represents the size of volumetric averaging (see Eq. (4.5)). The effect of volumetric averaging on the integral length scale of radial velocity is presented in (c) in terms of the relationship between  $L_R/L_r$  and  $\sigma_Q/L_1$  for different  $\theta$  values where  $L_r$  and  $L_R$  are the integral length scales of  $v_r$  and  $v_R$ .

Radial velocity measurements from a pulsed lidar naturally form a discrete time series (see section 4.2). If a pulsed lidar is operated with the VAD technique to estimate

turbulence statistics (e.g. Sathe et al. (2015)), the lidar samples at least six locations sequentially and therefore the sampling interval ( $\delta t$ ) at one location is at least six times of the sampling interval per one lidar measurement (i.e.  $\delta t > 6$  sec and is at least 60 times slower than a sonic anemometer sampling at 10 Hz). Hence, the radial velocity variance estimated from  $v_r$  acquired over a period  $T$  with a sampling interval  $\delta t$  is estimated from:

$$\mu_{2,r}(T) = \frac{1}{N} \sum_{i=1}^N [v_r(t_i) - \mu_{1,r}(T)]^2 \quad (4.10)$$

where  $t_i$  is the time stamp of measurement,  $N = 1 + T/\delta t$  is the sample number, and  $\mu_1(T)$  is the ensemble mean estimate:

$$\mu_{1,r}(T) = \frac{1}{N} \sum_i^N v_r(t_i) \quad (4.11)$$

The radial velocity variance estimated from Eq. (4.10) has a systematic error  $E_{s,r}$  given by:

$$E_{s,r} = \langle \mu_{2,r}(T) \rangle - \mu_{2,r} = -\langle \mu_{1,r}^2(T) \rangle \quad (4.12)$$

Note that  $\langle \mu_1^2(T) \rangle$  is the sample mean variance; hence the systematic error is always negative, and its relative magnitude is given by (Box et al. 2008):

$$e_{s,r} = -\frac{E_{s,r}}{\mu_{2,r}} = \frac{S_{1,r}}{N^2} \quad (4.13)$$

where

$$S_{1,r} = \sum_{i=1}^N \sum_{j=1}^N \rho_r(t_i - t_j) \quad (4.14)$$

Each radial velocity variance estimated from Eq. (4.10) also has a random error relative to the expected value of estimate  $\langle \mu_2(T) \rangle$  that has zero mean and variance defined as:

$$E_{r,r}^2 = \langle [\mu_{2,r}(T) - \langle \mu_{2,r}(T) \rangle]^2 \rangle \quad (4.15)$$

Applying the Isserlis relation of a Gaussian process (Lenschow et al. 1994), it can be shown that the relative random error variance is:

$$e_{r,r}^2 = \frac{E_{r,r}^2}{\mu_{2,r}^2} = \frac{2}{N^4} S_{1,r}^2 + \frac{2}{N^2} S_{2,r} - \frac{4}{N} S_{3,r} \quad (4.16)$$

where

$$S_{2,r} = \sum_i^N \sum_j^N [\rho_r(t_i - t_j)]^2 \quad (4.17)$$

$$S_{3,r} = \sum_{i=1}^N \sum_{m=1}^N \sum_{n=1}^N \rho_r(t_i - t_m) \rho_r(t_n - t_i) \quad (4.18)$$

The error expressions derived in Eqs. (4.13) and (4.16) are valid for  $v_R$  variance with the replacement of the autocorrelation and the variance by  $\rho_R$  and  $\mu_{2,R}$ , respectively.

It is clear from Eqs. (4.13) and (4.16) that the errors are functions of the sampling interval, the sampling duration and the autocorrelation function. The volumetric averaging defined in Eq. (4.4) affects the shapes of the radial velocity covariance and autocorrelation function which was illustrated by an analysis based on the isotropic turbulence model in section 4.1 (Figure 4-1). However, atmospheric turbulence is not isotropic. To investigate this effect under realistic atmospheric conditions wind vectors are statistically simulated from the Risø Smooth-Terrain (SMOOTH) spectrum model using TurbSim (TurbSim 2016). The simulation domain is  $725 \times 60 \times 12$  m ( $x_1 \times x_2 \times x_3$ ) centered at 80 m above the ground, and has a horizontal and vertical resolution of

1.0 and 0.5 m, respectively. The mean wind speed is  $8 \text{ m s}^{-1}$ . The time interval is 0.125 sec. Point radial velocities ( $v_r$ ) are calculated using Eq. (4.3) for varying LOS orientations in the horizontal plane relative to the  $x_1$  direction (denoted by  $\beta$ ) with a fixed elevation angle of  $10^\circ$ . Lidar-equivalent radial velocities ( $v_R$ ) are derived by averaging  $v_r$  on the LOS within  $\pm 30$  m from the domain center using the weighting function in Eq. (4.5). As expected, variance reduction occurs for all LOS orientations. The difference between  $R_R$  and  $R_r$  in Figure 4-2 is similar to that in Figure 4-1, and can be explained using the structure function ( $D_r$ ) defined as:

$$D_r(\tau) = 2[R_r(0) - R_r(\tau)] \quad (4.19)$$

for a given time lag ( $\tau$ ) and used to represent the energy of eddies of sizes that are smaller than the scale  $U_1\tau$  (Pope 2000). Volumetric averaging only attenuates the energy of eddies of small sizes (Kristensen et al. 2011). When  $\tau$  is small relative to the integral time scale  $\tau_0$ , volumetric averaging causes  $D_r$  to decrease; hence,  $R_R$  has a lower gradient than  $R_r$  relative to  $\tau$  per Eq. (4.19). When  $\tau/\tau_0$  is large (e.g.  $\tau/\tau_0 > 0.25$ ), because volumetric averaging has little effect on eddies of scales of large  $\tau$ ,  $R_R = R_r$ . The difference between  $R_R$  and  $R_r$  results in  $\rho_R > \rho_r$  for all time lags and LOS orientations (Figure 4-2). Similar simulation is also conducted with the Kaimal (IECKAI) spectrum model (TurbSim 2016). Autocorrelation functions  $\rho_r/\rho_R$  are derived from the simulated  $v_r/v_R$  from both models, and the associated errors are calculated using Eqs. (4.13) and (4.16) (Figure 4-3). Though the difference between the errors of variance of  $v_r$  and  $v_R$  varies with LOS orientation and turbulence model (the turbulence structure), errors associated with  $v_R$  are consistently higher than that related to  $v_r$ , indicating volumetric averaging can cause errors of radial velocity

variance to increase.

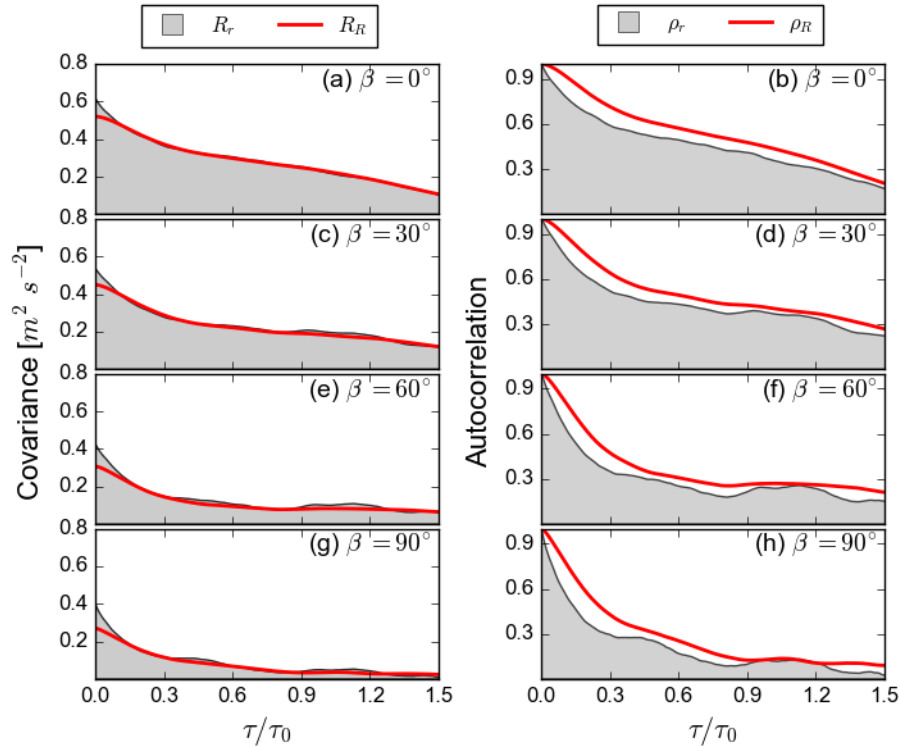


Figure 4-2 Covariance ( $R_r$  and  $R_R$  on the left) and autocorrelation functions ( $\rho_r$  and  $\rho_R$  on the right) of the point radial velocity ( $v_r$ ) and averaged radial velocity ( $v_R$ ) derived from statistically simulated time series using TurbSim with the SMOOTH model (TurbSim 2016). Parameters are set to the default values. Covariance and autocorrelation functions are presented for four different LOS orientations here as indicated by the angle of LOS relative to the mean wind direction ( $\beta$ ). The time lag ( $\tau$ ) is normalized by  $\tau_0$  which is the first time when  $\rho_r = 1/e$  at  $\beta = 0^\circ$ . A fixed elevation angle of  $10^\circ$  is used.

Thus both the statistically simulated wind data and physical reasoning provide evidence that volumetric averaging can increase the autocorrelation of radial velocity and consequently increase the errors in radial velocity variance estimate. Further confirmation will be provided in the next section, where data from a field experiment are used to show the effect of volumetric averaging and sampling duration on the errors.

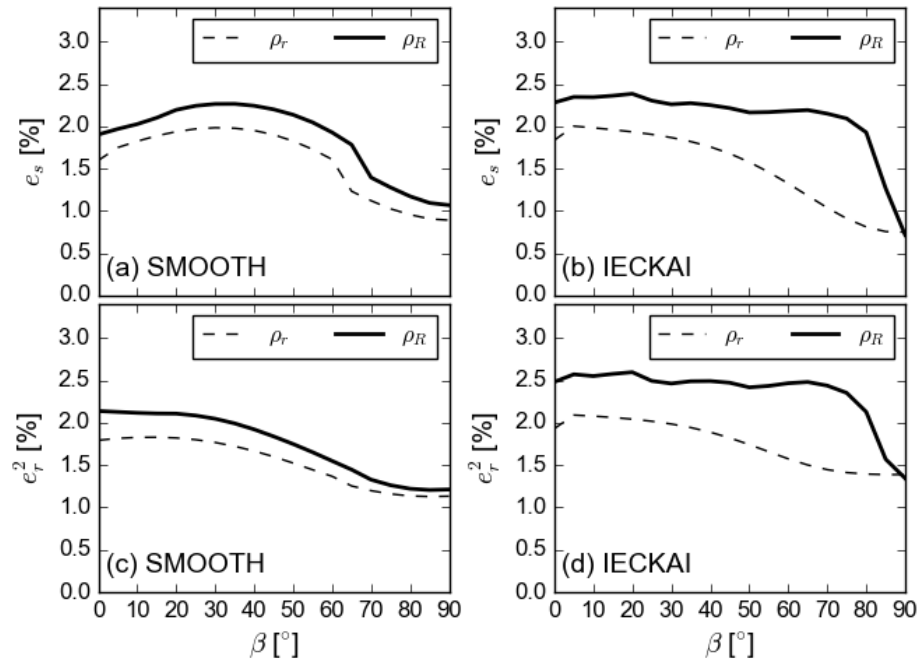


Figure 4-3 The relative systematic error ( $e_s$ ) and random error variance ( $e_r^2$ ) derived from the autocorrelation functions of the simulated point radial velocity ( $\rho_r$ ) and averaged radial velocity ( $\rho_R$ ) from the SMOOTH model in (a) and (c) and from the IECKAI model in (b) and (d) (TurbSim 2016) as functions of the angle between the LOS and mean wind direction ( $\beta$ ). The sampling duration is  $100\tau_0$  where  $\tau_0$  is the first time when the point radial velocity autocorrelation crosses  $1/e$  at  $\beta = 0^\circ$ .

#### 4.4 Errors from observations

##### 4.4.1 Experiment setup

Measurements presented herein were obtained during the Prince Edward Island Wind Energy Experiment (PEIWEE) conducted at the Wind Energy Institute of Canada (WEICan) site on the North Cape of PEI (Barthelmie et al. 2016). During the experiment a Galion lidar was configured with 20 kHz pulse repetition frequency and 1.0 sec dwell time to scan at four elevation angles ( $4.8^\circ$ ,  $10.0^\circ$ ,  $15.2^\circ$  and  $20.6^\circ$ ) and a single azimuth angle ( $349^\circ$ ) such that the 7<sup>th</sup> range gate of the lidar sampled at 20 m, 40 m, 60 m (and

80 m) above the ground where three Gill Windmaster Pro sonic anemometers were installed on a slender meteorological mast and sampled at 10 Hz. The measurements from the sonic anemometers are used to provide the atmospheric turbulence conditions and evaluate the accuracy of the lidar measurements. Hourly time series from the sonic anemometers were excluded if missing data is more than 10%. The sampling interval of the lidar at each elevation angle is about 7.5 seconds, which is similar to the sampling interval of the 6-beam technique used for turbulence measurement in Sathe et al. (2015).

The lidar conducted automatic cleaning at the beginning of each hour, resulting in a 60-second gap in the measurements; thus analysis presented here use a sample period of one hour. Comparison of the hourly mean and variance of the radial velocities from both the lidar and those derived from the sonic anemometers using the relationship in Eq. (4.3) indicates good agreement (the correlation coefficient = 0.998) with the exception of the periods when the measurements were in the wake of a wind turbine located 60 m southwest of the Galion (Figure 4-4). The variance is consistently higher (on average by 19%) for the sonic radial velocity than the lidar radial velocity because of the expected attenuation in variance caused by volumetric averaging.

Stationarity is the fundamental assumption required to obtain theoretical estimates of the errors (as in section 4.3). Thus, the lidar radial velocity data are evaluated for stationarity using the approach of Foken and Wichura (1996). Each hourly time series is evenly divided into 12 subsets. If the mean of the variance of the subsets deviates by less than 30% from the variance of the hourly time series, the time series is considered to be stationary. Among all the hourly time series obtained at the three heights, 33 pass the stationarity test and have concurrent sonic data (Figure 4-4); therefore, they are used

to derive empirical estimate of error.

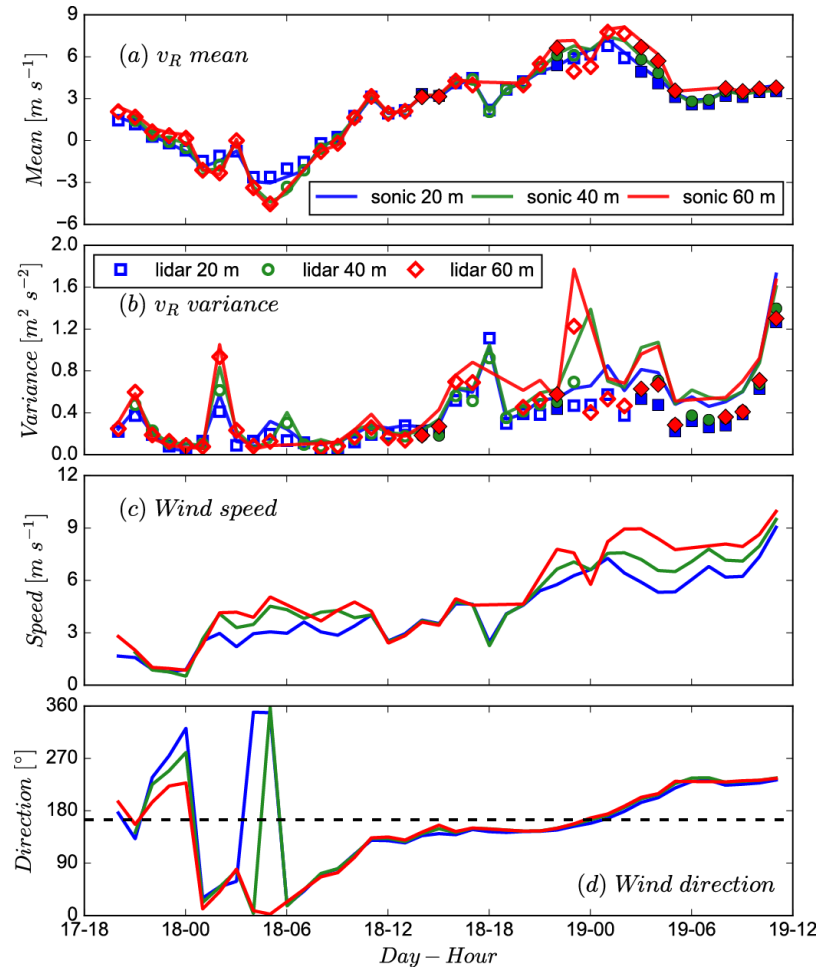


Figure 4-4 The Time series of **(a)** hourly mean and **(b)** variance of radial velocity ( $v_R$ ) from the lidar (markers) and the sonic anemometers (lines) and time series of **(c)** hourly mean wind speed and **(d)** direction from the sonic anemometers at three different heights. The mean and variance of radial velocity from the hourly time series classified as stationary using the method of Foken and Wichura (1996) are shown by the filled markers. The dash line in **(d)** gives the wind direction under which the sonic anemometers are in the center of the wind turbine wake.

#### 4.4.2 Error estimation method

The systematic errors  $e_s(T_n, T)$  and random error variance  $e_r^2(T_n, T)$ , in the observed time series associated with the sampling duration  $T_n$  estimated from a time series of length  $T$  are estimated using the stationary bootstrap method (Politis and Romano

1994) as follows where the sample numbers associated with  $T$  and  $T_n$  are denoted as  $N_T$  and  $N_{T_n}$ , respectively:

- A new time series of size of  $N_T$  is constructed by resampling blocks of the original time series. To keep the new time series stationary, the sizes of the blocks are randomly drawn from a geometric distribution and the locations (the start of each block) are randomly drawn from a discrete uniform distribution on  $(1, 2, \dots, N)$  with the stationary bootstrap method. The only parameter for the geometric distribution  $p = 1/B_{opt}$ , where  $B_{opt}$  is the optimal block size which can be found by minimizing the mean square error of the estimate of the sample mean variance (Politis and White 2004).
- A subset of size of  $N_{T_n}$  is randomly selected from the new time series and its mean and variance, denoted as  $\mu_1(T_{n,i})$  and  $\mu_2(T_{n,i})$ , respectively, are recorded. The subscript  $i$  denotes that it is the  $i^{th}$  resampling.
- Sequences of  $\mu_1(T_{n,i})$  and  $\mu_2(T_{n,i})$  are acquired after repeating the two steps above for  $N_b$  times. The variance of the sample mean  $\langle \mu_1^2(T_n, T) \rangle$  is approximated as:

$$\langle \mu_1^2(T_n, T) \rangle = \frac{1}{N_b} \sum_{i=1}^{N_b} \mu_1^2(T_{n,i}) \quad (4.20)$$

- Per the definition in Eq. (4.12) the systematic error  $e_s(T_n, T)$  can be calculated as:

$$e_s(T_n, T) = \frac{\langle \mu_1^2(T_n, T) \rangle}{\mu_2(T)} \quad (4.21)$$

- To calculate the random error variance, the expected value  $\langle \mu_2(T_n, T) \rangle$  is first estimated by adding the systematic error to  $\mu_2$  which is approximated by  $\mu_2(T)$ , i.e.,

$$\langle \mu_2(T_n, T) \rangle = \mu_2(T) - \langle \mu_1^2(T_n, T) \rangle \quad (4.22)$$

Then the random error variance is derived with the following equation:

$$e_r^2(T_n, T) = \frac{\frac{1}{N_b} \sum_{i=1}^{N_b} [\mu_2(T_{n,i}) - \langle \mu_2(T_n, T) \rangle]^2}{\mu_2^2(T)} \quad (4.23)$$

#### 4.4.3 Observed errors

Two methods are used to estimate the errors associated with different sampling durations after the means are removed from the hourly time series of the point radial velocity from sonic anemometers ( $v_{r,sonic}$ ) and the lidar-measured averaged radial velocity ( $v_{R,lidar}$ ). The first method, denoted as the  $M_\rho$  method, is based on Eqs. (4.13) and (4.16) and the autocorrelation derived from measurements (Figure 4-5a). The observed autocorrelation functions show the postulated effect of volumetric averaging on the autocorrelation function. For all the hourly time series studied here, the autocorrelation of  $v_{R,lidar}$  at time lag one ( $\tau = 7.5$  sec) is significantly higher than that of  $v_{r,sonic}$  (Figure 4-6). At time lag two ( $\tau = 15$  sec), the autocorrelation of  $v_{R,lidar}$  is still larger than that of  $v_{r,sonic}$  but the difference is not always statistically significant. Beyond time lag two ( $\tau > 15$  sec), the difference between the autocorrelation of  $v_{R,lidar}$  and  $v_{r,sonic}$  vanishes, because as discussed above, volumetric averaging has little effect on turbulence eddies of large sizes that determine the velocity correlations at large time lags relative to the integral time scale.

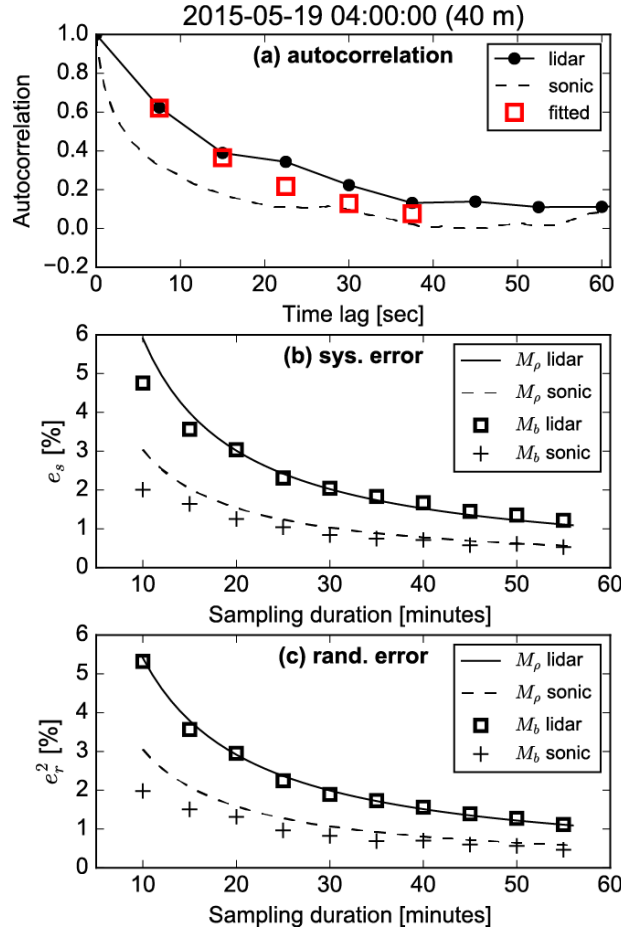


Figure 4-5 An example of the autocorrelation and errors in radial velocity variance estimate using data from the hour starting at 2015-05-19 04:00 at 40 m height. The autocorrelation functions derived from the lidar and sonic measurements are presented in (a). Systematic errors ( $e_s$ ) and random errors ( $e_r^2$ ) are presented in (b) and (c), respectively. Errors associated with both lidar and sonic anemometer data are estimated using the autocorrelation function from measurements (denoted by  $M_\rho$ ) and the stationary bootstrap method (denote by  $M_b$ ) described in section 4.4.2. The red squares in (a) denote the autocorrelation function fitted with the isotropic turbulence model from Pope (2000).

Because integral time scales of streamwise velocity (from the sonic data) are all below 30 sec, we assume that the autocorrelation function values of both  $v_{r,sonic}$  and  $v_{R,lidar}$  are zero for time lags larger than 60 sec. The autocorrelation-based systematic error and random error will be denoted as  $e_{s,\rho}$  and  $e_{r,\rho}^2$ , respectively. The second

method, denoted as  $M_b$  method, uses the stationary bootstrap method described in section 4.4.2 and the resultant systematic error and random error will be denoted as  $e_{s,b}$  and  $e_{r,b}^2$ , respectively (see the example given in Figure 4-5).

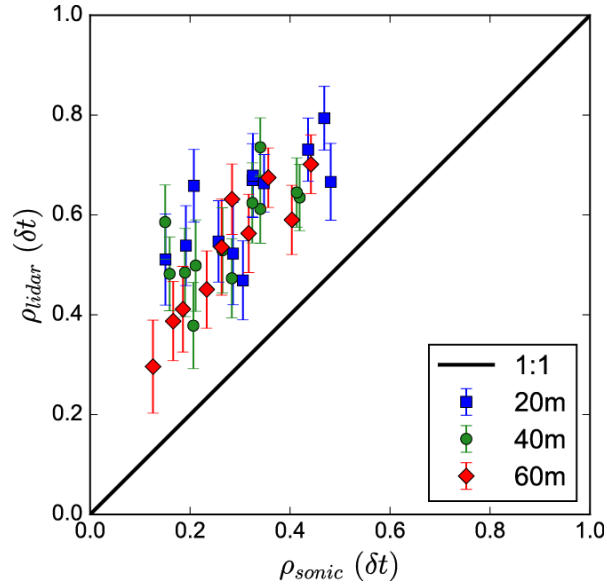


Figure 4-6 Comparison of the values of radial velocity autocorrelation function from the sonic data ( $\rho_{sonic}$ ) and the lidar data ( $\rho_{lidar}$ ) at the first time lag  $\delta t = 7.5$  sec. The 95% confidence interval of  $\rho_{lidar}$  is indicated by the error bar.

Consistent with the expectation, error estimates from both  $M_\rho$  and  $M_b$  method are higher for  $v_{R,lidar}$  than  $v_{r,lidar}$  (Figure 4-7) due to the autocorrelation function differences. Both methods give very similar estimates of the systematic error, although there are a few cases for which the  $M_\rho$  method produces higher systematic errors than the  $M_b$  method (Figure 4-8). The median of  $e_s$  from  $v_{R,lidar}$  is 1.5%/0.9% for  $T = 30/55$  minutes. For the random error, errors from the  $M_\rho$  method are always higher than the  $M_b$  method due in part to negative bias in the  $M_b$  method (Politis and White 2004) (Figure 4-8). The median of  $e_r^2$  from  $v_{R,lidar}$  is 1.6%/0.9% (12.7%/9.5% in terms of standard deviation) for  $T = 30/55$  minutes, respectively. Despite the expected

difference between the errors from the two methods, both methods consistently confirm the trend of decreasing error with increasing sampling duration (Figure 4-9), and the relatively close agreement of the results from the two approaches offers empirical support for the relationships between the errors and the autocorrelation function of radial velocity as described by Eqs. (4.13) and (4.16) for ergodic and stationary time series.

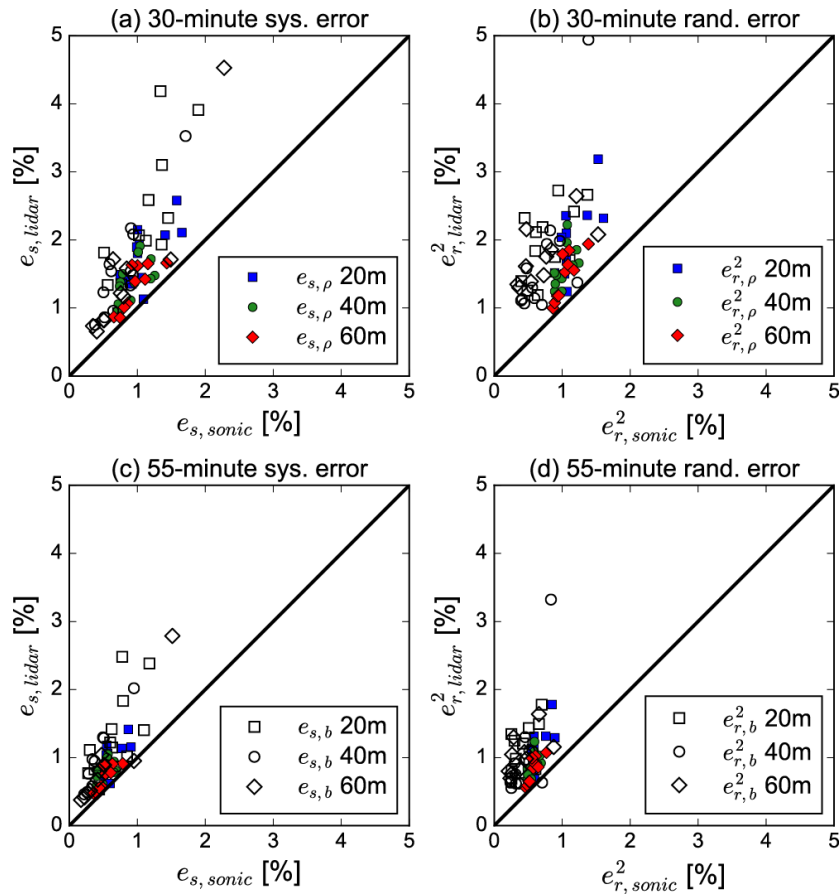


Figure 4-7 Comparison of the systematic error estimated from the sonic data ( $e_{s,sonic}$ ) and from the lidar data ( $e_{s,lidar}$ ) in (a) for a sampling duration of 30 minutes and (c) a sampling duration of 55 minutes, and comparison of the random error estimated from the sonic data ( $e_{r,sonic}^2$ ) and from the lidar data ( $e_{r,lidar}^2$ ) in (b) for a sampling duration of 30 minutes and (d) a sampling duration of 55 minutes. The method used to estimate the errors is indicated by the subscript in the legend where  $\rho$  denotes the  $M_\rho$  method using the autocorrelation function and  $b$  denotes the  $M_b$  method using the stationary bootstrap method. The dark lines are the 1:1 lines.

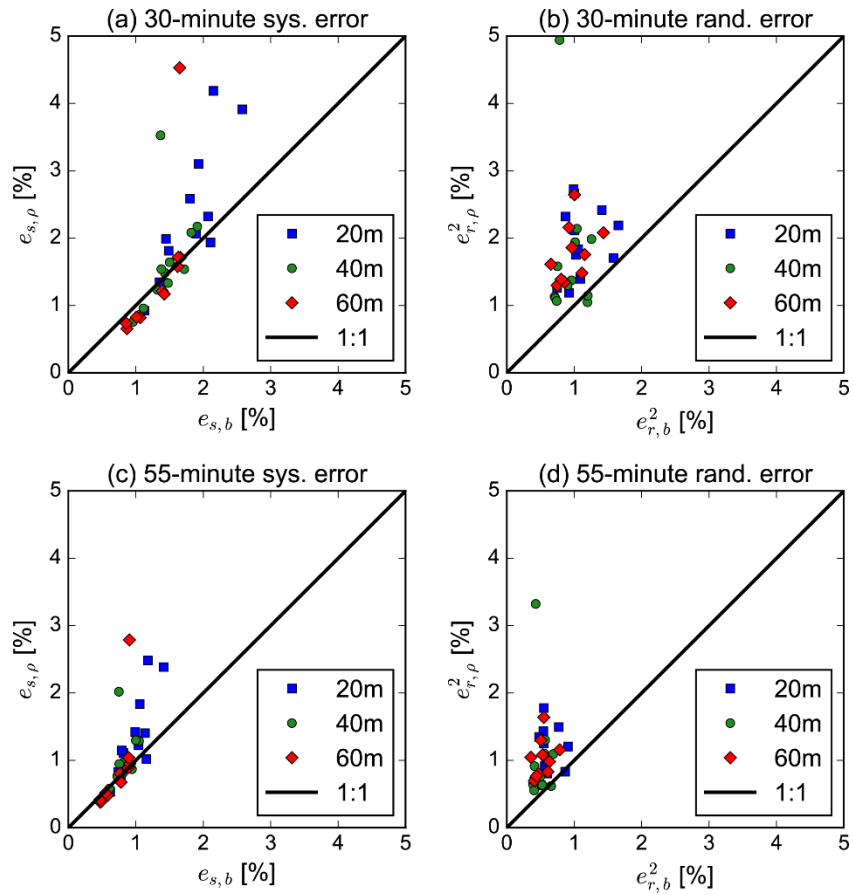


Figure 4-8 Comparison of the lidar radial velocity systematic errors  $e_{s,\rho}$  and  $e_{s,b}$  estimated using the autocorrelation ( $M_\rho$ ) method and the stationary bootstrap ( $M_b$ ) method, respectively, for (a) a sampling duration of 30 minutes and (c) a sampling duration of 55 minutes, and comparison of the lidar radial velocity random errors  $e_{r,\rho}^2$  and  $e_{r,b}^2$  estimated using the  $M_\rho$  method and the  $M_b$  method, respectively, for (b) a sampling duration of 30 minutes and (d) a sampling duration of 55 minutes. The measurement heights can be found in the legend.

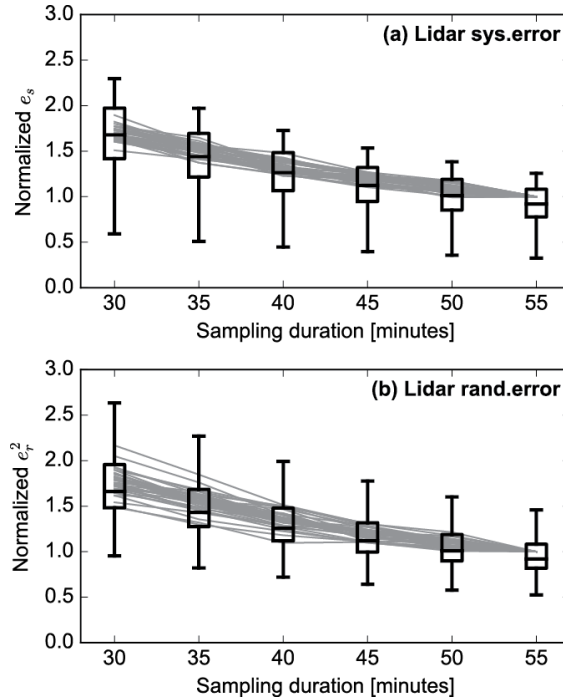


Figure 4-9 Relationships between **(a)** the systematic error ( $e_s$ ) and the sampling duration and **(b)** the random error ( $e_r^2$ ) and the sampling duration for radial velocity variance estimated from the lidar data using the autocorrelation method (gray lines) and the stationary bootstrap method (boxplots). The errors are normalized by the respective errors estimated from the autocorrelation method with the sampling duration of 55 minutes.

#### 4.5 Discussions

On the basis of the empirical evidence presented in section 4.4, in the following we use the theoretical framework presented in section 3 to describe how the error in estimating radial velocity variance from lidar measurement which results from the (1) autocorrelation function, (2) sampling duration and (3) sampling interval can be minimized. The first factor (autocorrelation) is determined by the underlying wind field, the lidar LOS orientation and the size of volumetric averaging (i.e.  $\sigma_Q$  in Eq. (4.5)). The autocorrelation function is determined by the underlying turbulence field and therefore not controllable. Therefore, in practice, error reduction can only be achieved

by adjusting the other two factors: sampling duration ( $T$ ) and sampling interval ( $\delta t$ ), with the knowledge of autocorrelation function  $\rho(\tau)$  estimated from measurements or approximated by turbulence models.

Here we use the isotropic turbulence model to model the autocorrelation function. Note that the atmospheric turbulence is rarely isotropic. During all the hours presented in section 4, turbulence was not isotropic because the three wind components had non-equal variance. However, it is always possible to find an integral length scale to reproduce the observed autocorrelation of radial velocity variance from lidar measurements with the isotropic turbulence model (e.g. Figure 4-5). Therefore, we argue that with a proper length scale the isotropic turbulence model can generate an autocorrelation function that can be used to approximate non-isotropic turbulence conditions, justifying the use of the isotropic turbulence model here.

Based on the isotropic turbulence model, the relative systematic error ( $e_s$ ) is negligible in comparison to the random errors. Hence, only the analysis of random errors ( $e_r^2$ ) is given below. The magnitude of  $e_r^2$  is not sensitive to the sampling interval ( $\delta t$ ). Because the integral time scale ( $\tau_0$ ) has the order of magnitude of 10 sec and  $\delta t = 1-10$  sec, it is likely that  $\delta t/\tau_0 < 1$ , implying that in practice sampling interval is a minor factor on error reduction (Figure 4-10). Increasing the size of volumetric averaging (in terms of  $\sigma_Q$ ) can cause  $e_r^2$  to increase with a rate that decreases to nearly zero when the LOS moves from parallel to perpendicular to the wind direction (i.e.  $\beta$  from  $0^\circ$  to  $90^\circ$ ) and the sampling duration increases (Figure 4-11); therefore, it is also a minor factor on error reduction when the sampling duration is long. The orientation of the LOS relative to the wind direction ( $\beta$ ) naturally affect the properties of random errors because

it determines the time scale of radial velocity. For example, for the isotropic turbulence model used here, streamwise velocity has the largest time scale. Therefore, errors are large when the LOS is aligned with the wind direction (i.e.,  $\beta = 0^\circ$ ) (Figure 4-10 and Figure 4-11). However, in general  $e_r^2$  is not sensitive to  $\beta$ . Note that the effect of  $\beta$  on  $e_r^2$  will change when different turbulence model is applied. The factor that has the most significant effect on error reduction is the sampling duration (Figure 4-10 and Figure 4-11). Thus optimization of lidar operation of retrieval of radial velocity variance can be considered through the lens of ‘how long is long enough?’ (Lenschow et al. 1994). Provided that the optimum six beam configuration proposed in Sathe et al. (2015) (i.e.  $\phi = 45^\circ$ ) is applied to the Galion lidar for which  $\sigma_Q = 15.6$  m under neutral atmospheric conditions over flat terrain, both the systematic and random errors are almost independent of LOS orientation and surface roughness length which is used to predict the integral length scale and turbulence intensity (Figure 4-12). The systematic error is lower than 1.0 % when  $T > 30$  minutes (Figure 4-12) The random error in terms of its standard deviation can be reduced from 12% to 9.0% by increasing the sampling duration from 30 minutes to 55 minutes (Figure 4-12), which is consistent with the observed range 12.7% – 9.5% in section 4.3. The value of  $e_r$  remains to be higher than 6% when  $T$  increases to 120 minutes (Figure 4-12). Note that the volumetric averaging causes a small amount of increase in random errors because of the relative small size of volumetric averaging (i.e.  $\sigma_Q/L_1 < 0.1$ ). The implication of the analysis above is that, given that 0.5~1.0 hour is usually the length over which stationarity assumption is valid in the ABL (Larsén et al. 2016), radial velocity variance estimate will likely to have around 10% uncertainty and it will be hard to reduce the uncertainty to a level lower

than 5%.

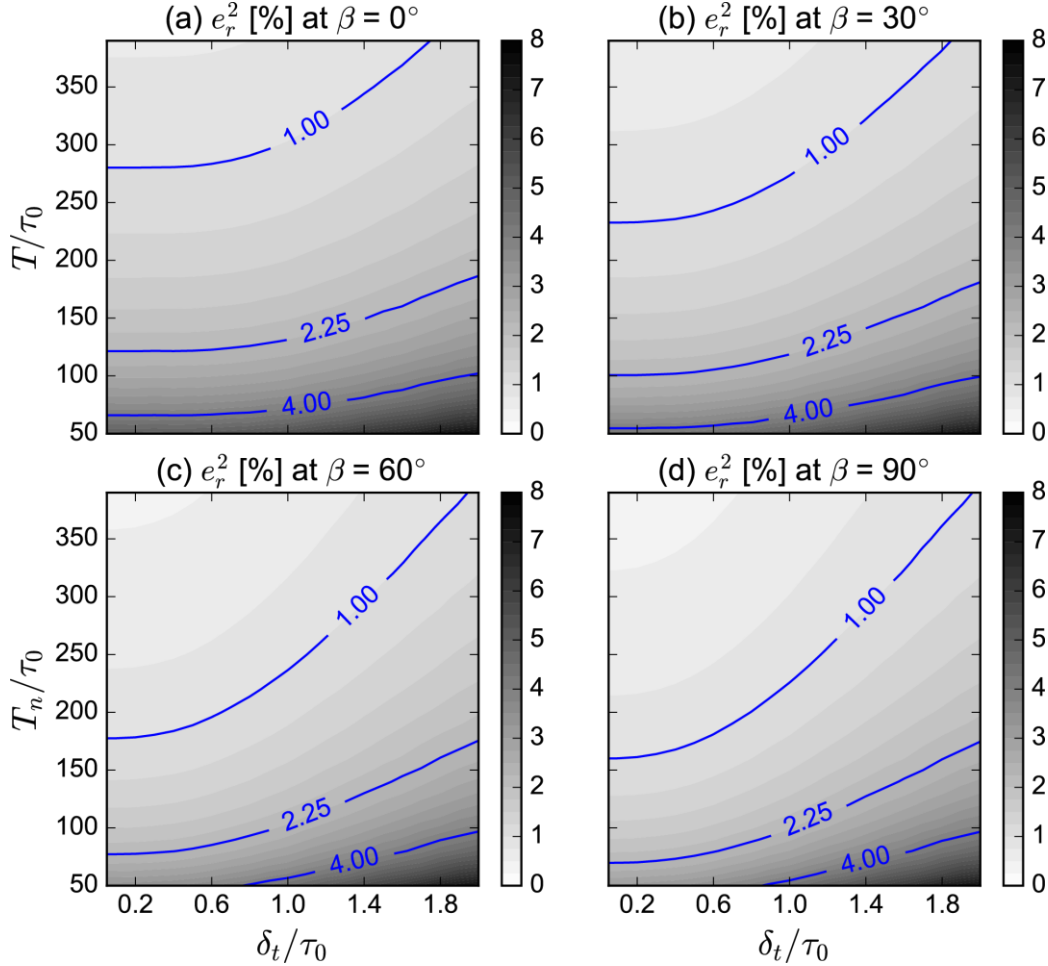


Figure 4-10 Contours of the relative variance ( $e_r^2$ ) of random errors of radial velocity variance from lidar measurements estimated from the isotropic turbulence model (Pope 2000) and the von Kármán spectrum model (Burton et al. 2011) as a function of the sampling duration ( $T$ ) and the sampling interval ( $\delta t$ ) normalized by the integral time scale ( $\tau_0$ ) for four different  $\beta$  values where  $\beta$  is the angle between the LOS and the wind direction. The weighting function (Eq. (4.5)) representing the volumetric averaging has a standard deviation  $\sigma_Q = 0.2L_1$  where  $L_1$  is the streamwise integral length scale. The other input parameters include the elevation angle  $\phi = 10^\circ$  and the mean wind speed  $U_1 = 8 \text{ m s}^{-1}$ .

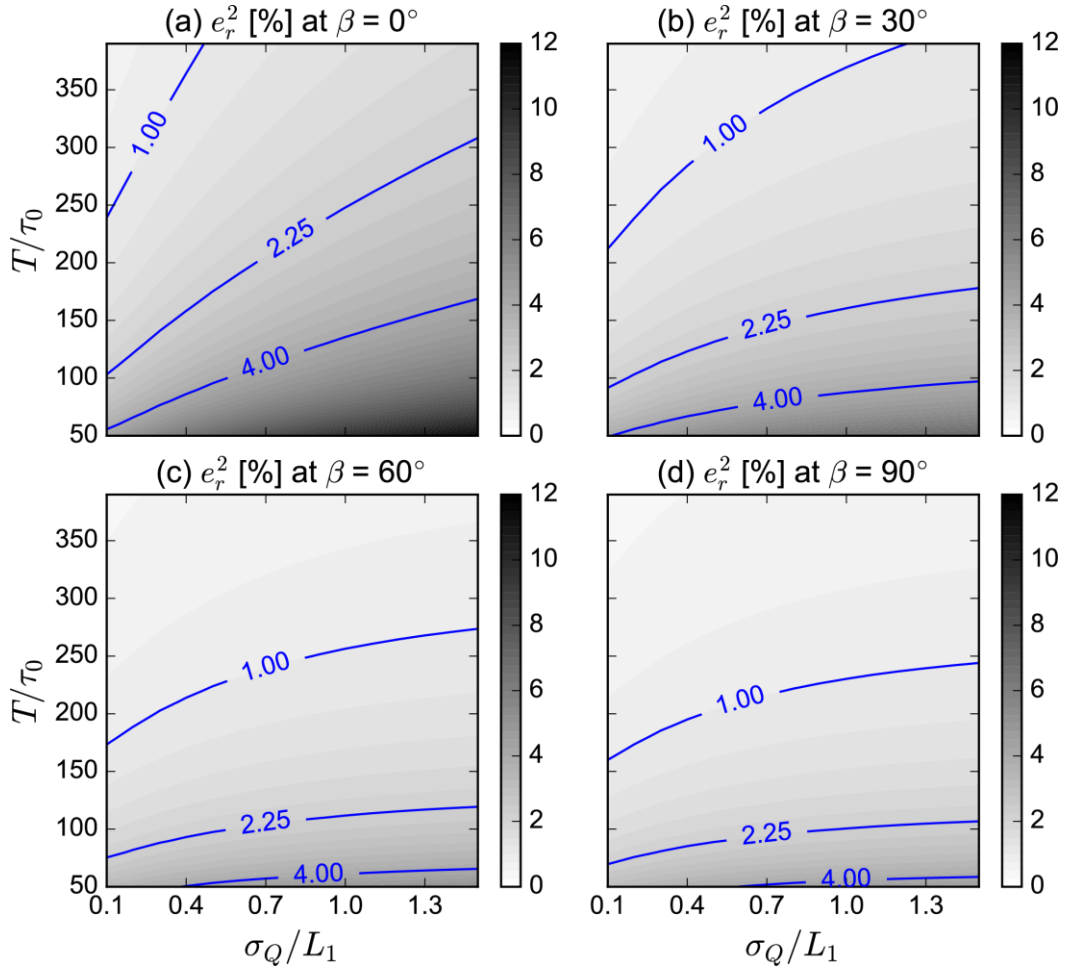


Figure 4-11 Contours of the relative variance ( $e_r^2$ ) of random errors of radial velocity variance from lidar measurements estimated from the isotropic turbulence model (Pope 2000) and the von Kármán spectrum model (Burton et al. 2011) as a function of the sampling duration ( $T$ ) normalized by the integral time scale ( $\tau_0$ ) and the volumetric averaging size ( $\sigma_Q$ ) normalized by the streamwise integral length scale ( $L_1$ ) for four different  $\beta$  values in where  $\beta$  is the angle between the LOS and the wind direction. The other input parameters include the sampling interval  $\delta t = 0.5\tau_0$ , the elevation angle  $\phi = 10^\circ$  and the mean wind speed  $U_1 = 8 \text{ m s}^{-1}$ .

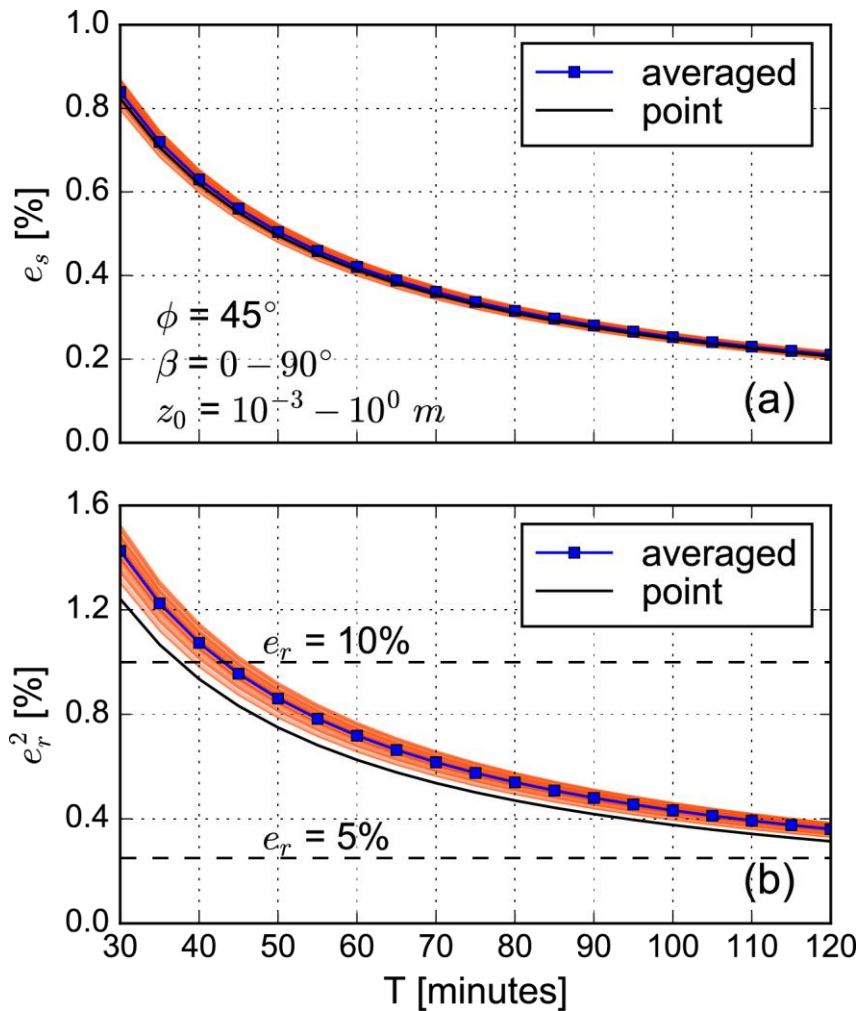


Figure 4-12 Variation of the relative systematic error ( $e_s$ ) and variance of random error ( $e_r^2$ ) with respect to the sampling duration ( $T$ ) in (a) and (b), respectively, predicted from the isotropic turbulence model (Pope 2000) and the von Kármán spectrum model (Burton et al. 2011) at 80 m height under neutral conditions for surface roughness lengths ( $z_0$ ) from  $10^{-3}$  m to  $10^0$  m and LOS orientations  $\beta$  from  $0^\circ$  to  $90^\circ$  where  $\beta$  is the angle between the LOS and the wind direction. The blue lines with squares and the dark lines are the mean error values from the entire range of  $z_0$  and  $\beta$  for the averaged and point radial velocity variance, respectively. The red shaded areas denote the range of errors of the averaged radial variance. The equation used to estimate the integral length scale can be found in Wang et al. (2015b) with the mean wind speed  $7 \text{ m s}^{-1}$  and the Coriolis parameter  $10^{-4} \text{ s}^{-1}$ . The elevation angle  $\phi = 45^\circ$ .

#### 4.6 Conclusion remarks

Use of lidar for estimation of turbulence fields if realized could revolutionize atmospheric boundary layer characterization studies and has applications to many fields. Accurate radial velocity variance estimates are necessary (but not sufficient) to obtaining robust turbulence statistics from lidar. The accuracy of radial velocity variance estimates and their relationship to pseudo-point measurements from sonic anemometers are determined by (i) the applicability of the stationarity assumption, (ii) the effect of volumetric averaging on radial velocity autocorrelation function, (iii) the sampling interval, and (iv) the sampling duration. Of these factors (i) the stationarity assumption is determined only by atmospheric conditions but is most likely to be achieved within the period of one hour in environments where the surface conditions are homogeneous. The second factor (ii) the volumetric averaging is dictated by the probe length that is determined by the lidar properties; it causes the radial velocity autocorrelation function to increase and thus increases errors in radial velocity variance estimates. Large probe length can result in high errors. The third factor (iii) the sampling interval is determined partly by the scan geometry which is needed to sample radial velocities with different LOS orientations to reconstruct the wind field, and partly by the lidar configurations of e.g. the dwell time of each measurement and the scanning speed. Errors are not sensitive to the sampling interval provided that the sampling interval for lidar turbulence measurement is commonly smaller than the turbulence integral time scale. The last factor (iv) the sampling duration, which together with the sampling interval determines the number of samples available for radial velocity estimates, can only be chosen within the limit implied by the stationarity assumption.

Errors decrease with increasing sampling duration.

Given these constraints on radial velocity variance estimates, this paper shows theoretically and using empirical observations that for sample periods for which stationarity can reasonably be asserted (approximately one hour), the systematic error can be reduced to a level lower than 1% and the random error in terms of its standard deviation will be around 10%. These errors will propagate through to estimation of turbulence statistics from lidar measurements and thus provide a fundamental limit on the likely accuracy of those estimates.

## CHAPTER 5 WIND TURBINE WAKE DETECTION WITH A SINGLE DOPPLER WIND LIDAR<sup>4</sup>

### 5.1 Introduction

Wind turbine wakes are characterized by low wind speed and high turbulence intensity relative to the freestream. As a result, wind turbines in the wake of operating wind turbines can experience reduced power output and enhanced fatigue load (Barthelmie et al. 2009). To reduce the adverse effects of wind turbine wakes, accurate wake modelling plays a critical role in wind farm layout and operation optimization, and the accuracy of the wake models needs to be verified with observations (Barthelmie et al. 2006). While verification can be performed with in-situ measurements and downscaled experiments in wind tunnels, remote sensing technologies have shown potential in studying wake characteristics and testing wake models in full-scale wind farms. For example, a single coherent Doppler wind lidar (hereafter called lidar) can be used to study the wake recovery and expansion along the downwind distance from the wind turbine under various atmospheric conditions (Aitken et al. 2014). With two lidars it has been shown that wake has a fast recovery rate in convective atmospheric conditions (Iungo and Porté-Agel 2014). Measurements from dual Doppler radars have been used to characterize the complex flow features such as wake merging in a large wind farm (Hirth et al. 2015). To further explore the potential of lidar for wind turbine wake characterization, this paper presents an experiment designed to test the performance of a single lidar for measuring the wake of a continuously yawing wind turbine. This paper

---

<sup>4</sup> Wang, H., and R. J. Barthelmie, 2015: Wind turbine wake detection with a single Doppler wind lidar, *Journal of Physics: Conference Series*, **625**, 012017. doi: 10.1088/1742-6596/625/1/012017

is organized as follows: A brief description of lidar operation principle is given in Section 2, and then followed by the description of the experiment setup in section 5.3. The wake profile estimation algorithm is described in section 5.4. Section 5.5 presents the wake characteristics, such as wake deficit and wake width, derived from the lidar measurements. Conclusions are drawn in section 5.6.

## 5.2 Lidar basics

A lidar only measures the radial velocity at each range gate. The radial velocity ( $v_R$ ) is the projection of the wind velocity ( $\mathbf{v} = [u, v, w]$ ) on the line-of-sight (LOS) which is the path of the light wave emitted by the lidar (Figure 5-1).

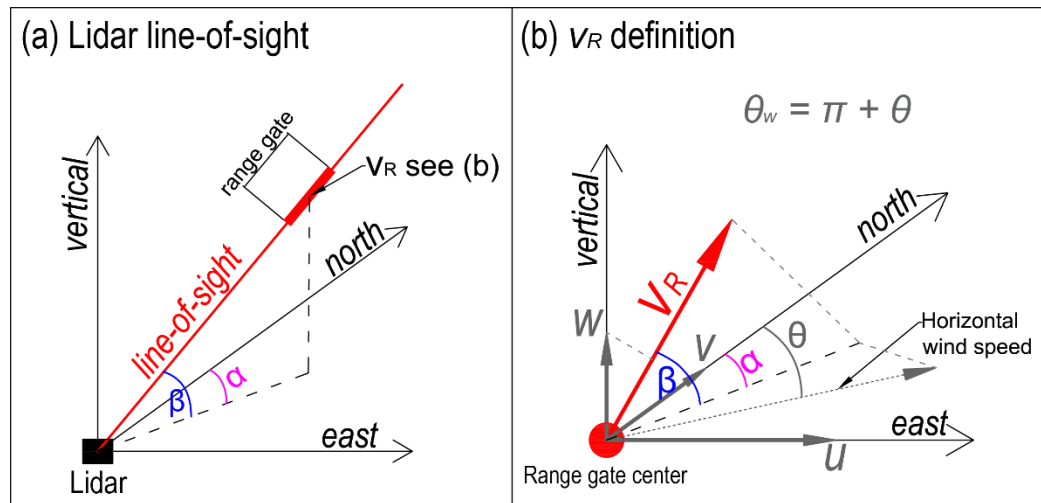


Figure 5-1 Schematics of (a) the orientation of the lidar line of sight in terms of the elevation angle ( $\beta$ ) and the azimuth angle ( $\alpha$ ), and (b) the relationship between the radial velocity ( $v_R$ ) and the wind velocity ( $\mathbf{v} = [u, v, w]$ ), and the relationship between the radial velocity and the horizontal wind speed and wind direction ( $\theta_w$ ).

Mathematically, the radial velocity can be expressed as:

$$v_R = u \cos \beta \sin \alpha + v \cos \beta \cos \alpha + w \sin \beta \quad (5.1)$$

where  $\alpha$  and  $\beta$  are the azimuth angle and the elevation angle of the LOS, respectively, and  $u$ ,  $v$  and  $w$  are the west-east, south-north and vertical components

of the wind velocity. The radial velocity can also be defined in terms of the horizontal wind speed ( $V$ ) and wind direction ( $\theta_w$ ):

$$v_R = -V \cos \beta \cos(\alpha - \theta_w) + w \sin \beta \quad (5.2)$$

where  $V = \sqrt{u^2 + v^2}$  and  $\theta_w = \pi + \arctan(u/v)$ . The range gate is the area over which the echo samples are used to estimate the radial velocity, and therefore the measured  $v_R$  represents the mean wind condition over the range gate.

### 5.3 Experiment setup

This experiment was conducted in a large wind farm in Indiana from 7-20 May 2012 (Barthelmie et al. 2014). Results are presented here from a case study on May 16 and 17, 2012 when the wind direction was from the northeast and southeast. A Galion lidar (denoted as Galion hereafter) was deployed on the southwest edge of the wind farm. To probe the wake of the wind turbine denoted as WT2 in Figure 5-2, the Galion was configured to perform 3-stack Plan Position Indicator (PPI) scans. Each stack of PPI scans has a fixed elevation angle and varying azimuth angles. The elevation angles were set to 8.0°, 8.5° and 9.0° for the three stacks, respectively. For each PPI stack, the azimuth angle changed from 60° to 90° with 1° increment. The range gate size was 30 m. The wind turbine WT2 has a hub height of 80 m and a rotor diameter of 77 m, and hence it was located between the range gate 17 and 18 of the three PPI stacks (Figure 5-2). The Galion's measurement height decreases with decreasing range gate, but it can still detect the wake of WT2 at the range gate 10 which is about 44 m above the ground and higher than the bottom tip of the rotor (41.5 m). An 80-m tall meteorological mast was collocated with the Galion, and the wind direction measured at 77 m height from the meteorological mast are used to estimate the wake profiles from the Galion

measurements. In addition, two ZephIR lidars were located about 10 m north of the Galion lidar measuring wind speeds at 40, 80, 120, 160 and 200 m height (Barthelmie et al. 2014).

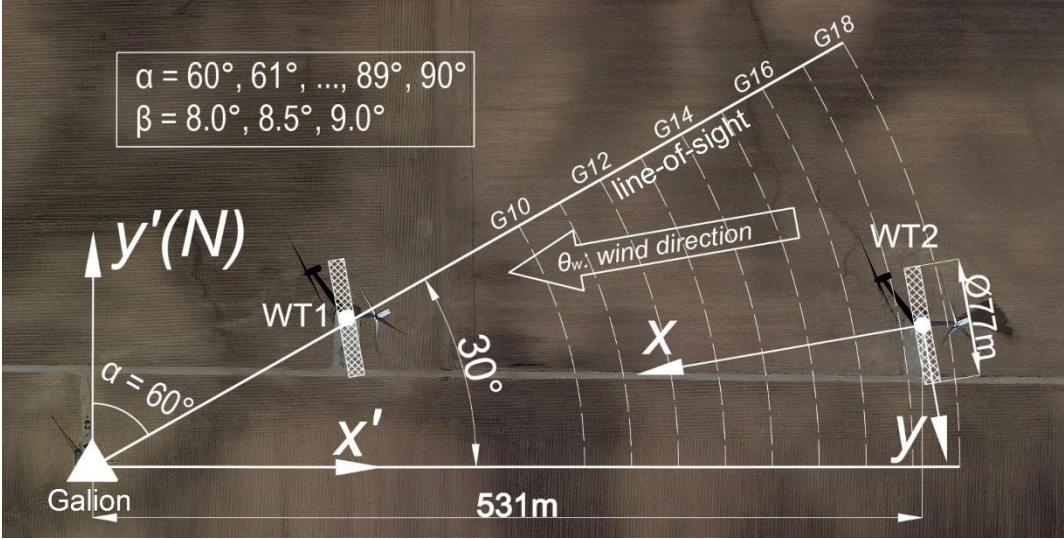


Figure 5-2 Top view of the locations of the Galion and the two wind turbines (WT1 and WT2), the scanning geometry used to probe the wake of WT2, and the two coordinate systems denoted as  $x'-y'$  and  $x-y$  (details see section 5.4.2). The azimuth angles ( $\alpha$ ) and elevation angles ( $\beta$ ) used are listed on the upper-left corner. The range gate locations are denoted by the dashed white lines. The underlying wind farm map is from the Google Earth.

### 5.4 Wake profile estimation algorithm

Wake characteristics are quantified by interpolating the wind speed estimated from the measured  $v_R$  to the locations of interest in the wake of WT2 using the Gaussian kernel smoother. Wake profiles are estimated for lines parallel to the rotor plane of WT2 at every  $0.2D$  distance downwind of WT2, where  $D$  is the rotor diameter. The first line is located at  $1.0D$  downwind of WT2. The conical surface formed by each PPI stack is treated as a slanted flat surface by ignoring the small curvature on the conical surface. Because of the non-zero elevation angle, the height associated with the estimated wind

speed varies across one individual line and among multiple lines for one PPI stack. Wake profiles are estimated from the measured  $v_R$  of each PPI stack according to the flow chart shown in Figure 5-3. The estimation method requires the wind direction as an input and uses the Gaussian kernel smoother to estimate the wake profiles of WT2. The details of the algorithm are given below.

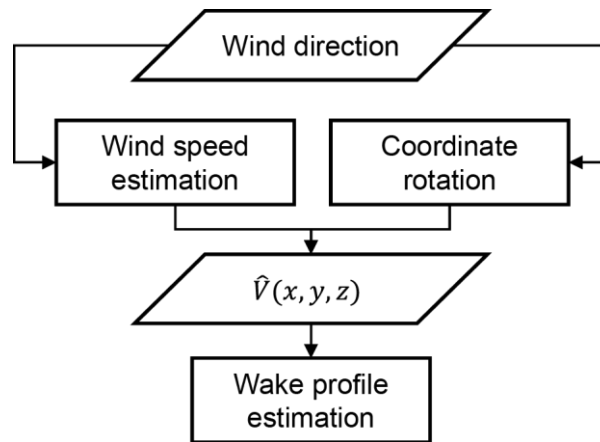


Figure 5-3 Wake profile estimation algorithm flow chart. The term  $\hat{V}$  is the wind speed estimated using the lidar data.

#### 5.4.1 Wind direction

The wake profile estimation algorithm requires *a priori* knowledge of the wind direction, which can be obtained from the wind direction measured at the nearby meteorological mast, or estimated from the Galion measurements in the freestream. For this project, the input wind direction is from the wind vane at 77 m height on the meteorological mast. Though wind directions are estimated from the measured radial velocities between the range gate 24 and 28, the estimated wind directions are not reliable because of the possible wind speed gradient at the edge of the wind farm. Thus, the wind direction estimated from the Galion measurements is not used.

### 5.4.2 Coordinate rotation

Two Cartesian coordinate systems are used in this algorithm. The first one is the conventional meteorological coordinate system  $(x', y')$  with its origin at the Galion location and x-coordinate and y-coordinate increasing eastward and northward, respectively (Figure 5-2). The second one is the streamwise coordinate system  $(x, y)$  with its origin at the location of WT2 (Figure 5-2). The relationship between the two coordinate systems is a function of the wind direction  $\theta_w$ :

$$x = x' \cos(1.5\pi - \theta_w) + y' \sin(1.5\pi - \theta_w) \quad (5.3)$$

$$y = y' \cos(1.5\pi - \theta_w) - x' \sin(1.5\pi - \theta_w) \quad (5.4)$$

Noting here we assume the rotor axis is parallel to the wind direction (i.e. no yaw error).

### 5.4.3 Wind speed estimation

When the vertical wind speed  $w$  is close to zero or the elevation angle  $\beta$  is small, the term  $w \sin \beta$  in Eq. (5.2) can be dropped. Then the horizontal wind speed ( $V$ ) can be calculated by rearranging Eq. (5.2) as:

$$V = -\frac{v_R}{\cos \beta \cos(\alpha - \theta_w)} \quad (5.5)$$

An incorrect  $\theta_w$  can introduce an error in the estimate of  $V$ , and the error is a function of both the wind direction error and the angle between the LOS and the wind direction, namely,  $\alpha - \theta_w$ . The error is small and insensitive to the wind direction error when  $(\alpha - \theta_w)$  is small (Figure 5-4). When  $(\alpha - \theta_w) = 60^\circ$ , the wind direction needs to be accurate within  $\pm 5^\circ$  in order to ensure that the relative error of the estimated wind speed  $< 10\%$ .

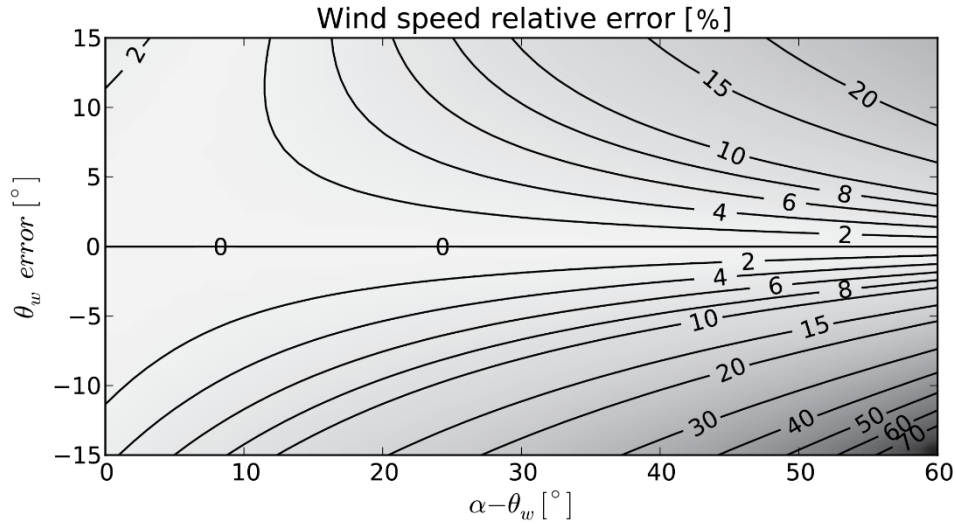


Figure 5-4 Contours of the wind speed relative error as a function of the wind direction ( $\theta_w$ ) error and the angle between the LOS and the wind direction ( $\alpha - \theta_w$ ), when Eq.(5.5) is used to estimate the wind speed.

#### 5.4.4 Wake profile estimation

For each PPI stack, wake profiles are estimated for lines that are parallel to the rotor plane of WT2 at every 0.2D downwind of WT2. The estimation starts at 1.0D and ends when the  $x$ -axis in Figure 5-2 is out of the scanning domain. The wind speed at a point of interest is estimated as the weighted average of all available wind speeds estimated with Eq. (4.5) from one PPI stack. The weight function is given by:

$$w_{gt}(x, y) = \exp\left(-\frac{l^2}{2L^2}\right) \quad (5.6)$$

where  $w_{gt}$  is the weight assigned to the wind speed at a range gate located at  $(x, y)$ ,  $l$  is the distance between the range gate and the point of interest (Daley 1993). The term  $L$  is a constant and it is set to 20 m considering that the Galion's spatial resolution is about 40 m. The distribution of the weight for a point at 2.0D downwind of WT2 is shown in Figure 5-5. An example of a wake profile estimated at 2.0D downwind of

WT2 is illustrated in Figure 5-6b. The wake center ( $y_{wc}$ ) is the location of the minimum wind speed or the wake center wind speed ( $V_{wc}$ ) on the line. The wake deficit ( $\delta$ ) is defined as:

$$\delta = \frac{V_0 - V_{wc}}{V_0} \quad (5.7)$$

where  $V_0$  is the freestream wind speed which is estimated as the mean of the five highest wind speeds from the wake profile. The Full Width at Half Maximum (FWHM, and denoted as  $S$ ) is used to characterize the wake width. The FWHM is estimated as the distance between the wake center and the location at which wind speed recovers by 50% (i.e. the deficit is  $0.5\delta$ ). As shown in Figure 5-6, the algorithm described above can detect the wake center and width up to  $3.8D$  downwind of WT2. The estimated wake deficit decreases with the downwind distance from  $\sim 60\%$  at  $1.0D$  to  $\sim 20\%$  at  $3.0D$  (Figure 5-6c). This is consistent with other observations (Aitken et al. 2014).

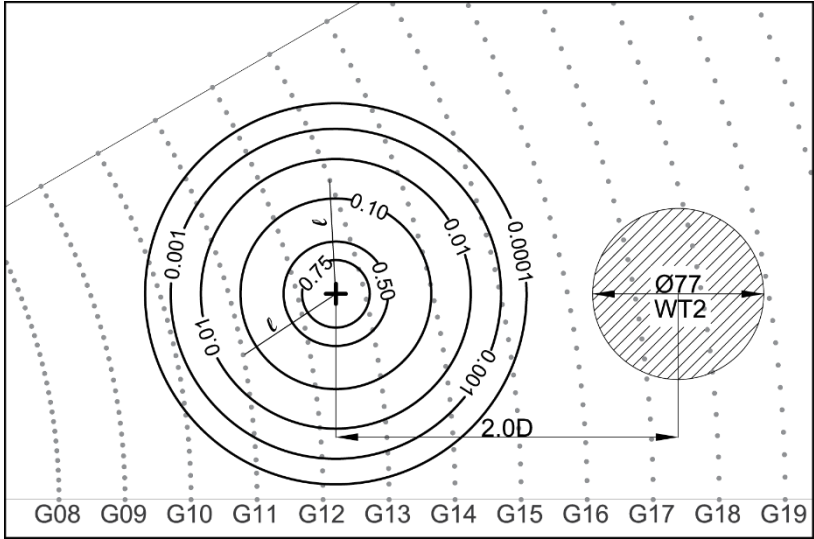


Figure 5-5 Contours of the weight used to calculate the wind speed at a point (dark cross) two rotor diameters ( $2.0D$ ) downwind of WT2 using Eq. (5.6). The gray circles are the Galion range gate locations, and the range gates are indexed by the numbers at the bottom.

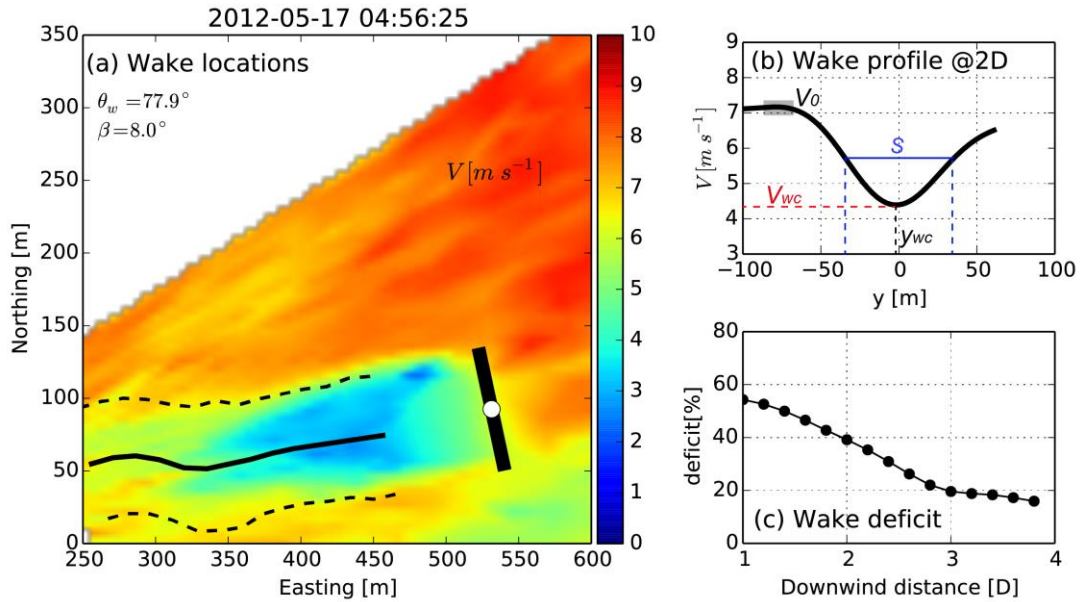


Figure 5-6 An example of wind speed retrieved for one stack of PPI scan. The wind speed over the entire scanned area is shown in (a). The wind turbine rotor orientation is denoted by the dark bar with a white circle indicating the location of WT2. The dark line is the wake center and the dashed lines denote the wake width. The estimated wind speed profile across the line that is parallel to the rotor plane at 2.0D downwind of WT2 is shown in (b). The definitions of wake center ( $y_{wc}$ ), the FWHM ( $S$ ), wake center wind speed ( $V_{wc}$ ) and freestream wind speed ( $V_0$ ) are also shown in (b). The wake deficit ( $\delta$  in Eq. (5.7)) as a function of the downwind distance normalized by the rotor diameter ( $D$ ) is shown in (c).

## 5.5 Results and discussions

Wakes of WT2 are observed during two periods marked as wake1 and wake2 in Figure 5-7, respectively, and their characteristics such as wake deficit and wake width will be presented hereafter. The wake1 period lasted for about 3 hours. WT2 was in the wake of the whole wind farm as the wind direction gradually changed from  $60^\circ$  to  $90^\circ$ . Measurements from both the cup anemometers on the meteorological mast and the ZephIR lidars were affected by the wakes of WT1 and WT2 (Figure 5-7). During the wake2 period, the wind veered from  $100^\circ$  to  $125^\circ$  as the wind speed ramped up to  $11 \text{ m s}^{-1}$ . Then the wind backed to  $115^\circ$  and the wind speed dropped to  $8 \text{ m s}^{-1}$ . Large wind

shear was also observed during this period (Figure 5-7). Wake profiles derived during the wake2 period represent single wakes from WT2 because WT2 is located in the first row of the wind farm. The freestream wind speed estimated from the wake profiles matches closely with measurements from the cup anemometer and the ZephIR lidar during the wake2 period (Figure 5-7).

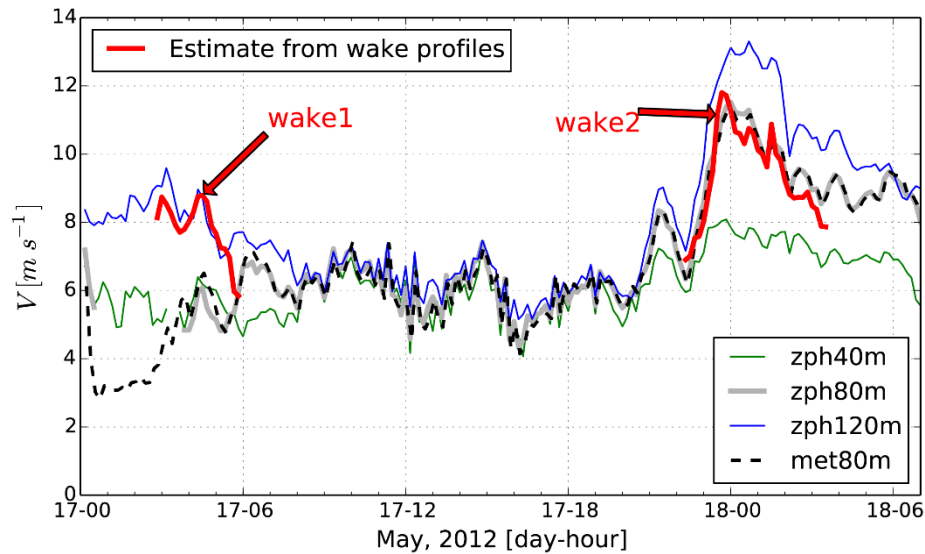


Figure 5-7 Time series for wind speed observed at 80 m on the meteorological mast and at 40 m, 80 m and 120 m heights by the ZephIR lidar. The two red lines are the time series of the freestream wind speed ( $V_0$  in Eq. (5.7)) derived from the estimated wake profiles.

### 5.5.1 Wake deficit

Wake deficits are presented as a function of the downwind distance normalized by the rotor diameter ( $D$ ) from WT2 in Figure 5-8 and Figure 5-9 for the wake1 and wake2 period, respectively. During the wake1 period, the lidar scanning geometry allows wake measurement up to  $3.8D$  downwind of WT2. The wake deficit decreases with increasing downwind distance from  $56\% \pm 4\%$  at  $1.0D$  to  $12\% \pm 6\%$  at  $3.8D$  (Figure 5-8). Note that

the height at which the wake deficit is evaluated also decreases with increasing downwind distance because of the non-zero elevation angle (Figure 5-8). Though the height is below the bottom tip of the rotor beyond 3.6D downwind of WT2, the wake deficit (~12%) still exists as the result of wake expansion. During the wake2 period, the lidar scanning geometry can only measure wake profiles up to 2.6D downwind of WT2. The height of the detected wake center remains almost the same along the downwind distance. The wake deficit has little variation between 1.0 D and 1.6D downwind of WT2 and gradually decreases with increasing downwind distance beyond 1.6D. Large variations in wake deficit are observed because WT2 was operating in a wide wind speed range ( $7.5\text{--}11.5\text{ m s}^{-1}$ ) during this period. The thrust coefficient of WT2 is low at high wind speeds, causing the low wake deficit for cases with wind speed  $> 10.5\text{ m s}^{-1}$ . However, the low wake deficits observed at high wind speeds are overestimated (i.e. the wake deficit is not low enough) because of the large height variation along each wake profile and the large vertical wind shear associated with these cases (Figure 5-10). For example, in the case shown in Figure 5-10, the wake center is located at 65 m height with wind speed  $7.1\text{ m s}^{-1}$ . The wake deficit is 35% based on the freestream wind speed ( $11\text{ m s}^{-1}$ ) estimated as the mean of the five highest wind speeds on the wake profile. However, the estimated freestream wind speed is from 80 m height. The actual freestream wind speed at 65 m height is about  $10\text{ m s}^{-1}$  according to the ZephIR measurement. Therefore, the actual wake deficit should be 29%, which is overestimated by 6% using the method presented in section 5.4.4.

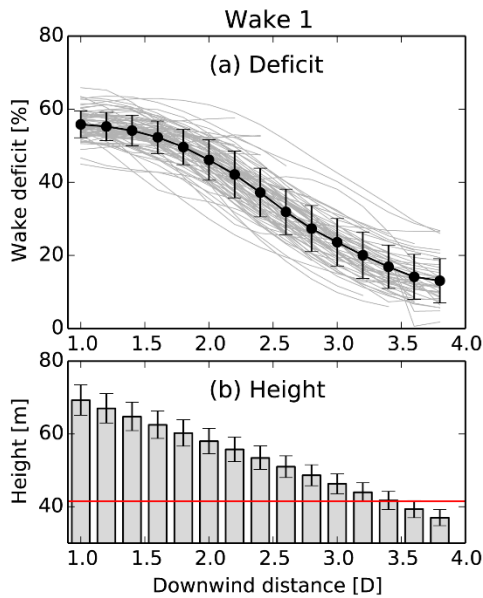


Figure 5-8 Wake deficit observed during the wake1 period as a function of the downwind distance in (a). The detected wake center height is given in (b) and the error bars denote the range. The red line in (b) denotes the rotor bottom tip.

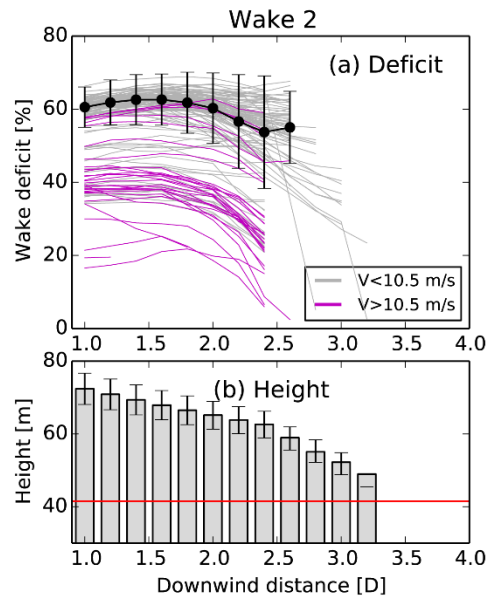


Figure 5-9 Wake deficit observed during the wake2 period as a function of the downwind distance in (a). The detected wake center height is given in (b) and the error bars denote the range. The red line in (b) denotes the rotor bottom tip.

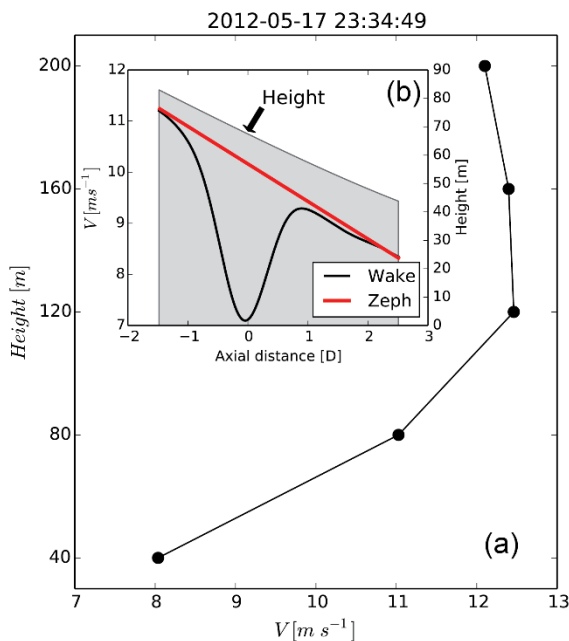


Figure 5-10 Wind shear measured by the ZephIR lidar in (a) and the wake profile derived from a PPI stack at 2D downwind of WT2 in (b) during the same 10-minute period. In (b), the dark line is the wake profile and the red line is the linearly interpolated from the ZephIR measurements at 40 m and 80 m in (a). The shaped area shows height variation across the wake profile.

### 5.5.2 Wake width

The wake width derived from the wake profile is the FWHM ( $S$ ) at a height that varies with the wind direction. Assuming that the wake deficit on the cross section parallel to the rotor plane of WT2 is axisymmetric about the rotor axis, the FWHM at the hub height ( $S_{hub}$ ) can be estimated by the following equation:

$$S_{hub} = \sqrt{S^2 + 4\Delta z^2} \quad (5.8)$$

Where  $\Delta z$  is the height difference between the hub height and the detected wake center. By further assuming the wake deficit follows a Gaussian profile, the hub height equivalent wake width, defined as four times the standard deviation of the Gaussian profile, is calculated as  $1.7S_{hub}$  and presented in Figure 5-11.

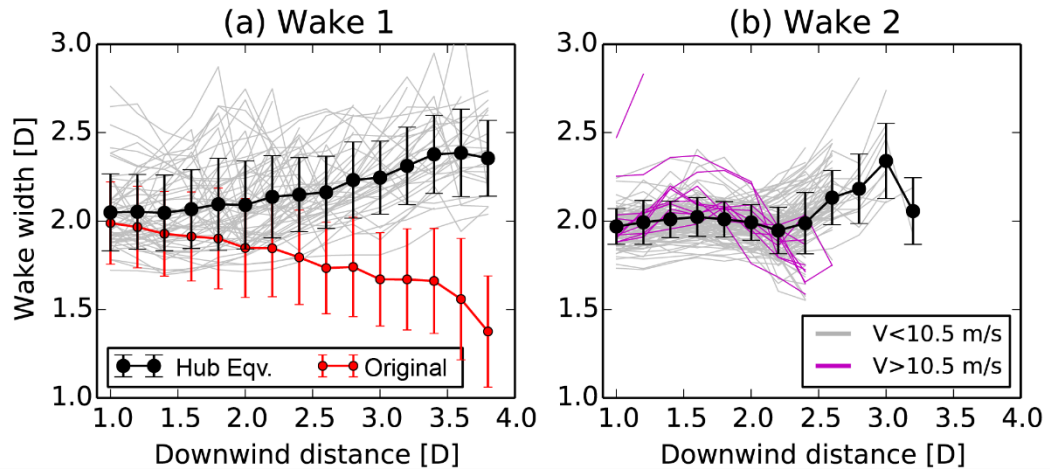


Figure 5-11 The equivalent hub height wake width as a function of the downwind distance normalized by the rotor diameter ( $D$ ) for (a) the wake1 period and (b) the wake2 period. The gray and purple lines represent wake width estimates from individual PPI stacks for low and high wind speed cases, respectively. Error bars show the mean with plus/minus one standard deviation. The dark error bars are based on the equivalent hub height wake width and the red error bars are derived from the original wake width estimated directly from the Galion measurements. The purple lines the wake2 period are not included in calculating the error bars.

During the wake1 period, the hub height equivalent wake width on average increases from 2.0D to 2.3D along the downwind distance of WT2. However, the wake widths from some individual PPI stacks show large variability with the downwind distance, and the variability is mainly caused by the inhomogeneous wind field on the edge of the wind farm (e.g. wind speed gradient seen in Figure 5-6a). The original wake width decreases with increasing downwind distance because the height of Galion measurements decreases as the wake moves away from WT2. During the wake2 period, the average wake width remains constant (about 2.0D) between 1.0D and 2.0D downwind of WT2. Note that wake widths during the wake2 period are derived from wake profiles on slanted lines (Figure 5-10). The wake profile on a slanted line is not symmetric when the vertical wind shear is high (Figure 5-10), causing difficulty in defining and detecting the wake width. The unexpected relationship between the wake width and the downwind distance for high wind speed cases (the purple lines in Figure 5-11) could be the result of asymmetric wake profiles on the slanted line, and hence, should not be used to characterize the wake expansion downwind of WT2.

### **5.5.3 Wake center**

The time series of the wake center at 2.0D downwind of WT2 is shown in Figure 5-12 for the wake2 period. The wake center deviates from the rotor axis by about 40 m or 0.5D at the beginning of this period when wind veers from 95° to 125°. Meanwhile the temporal variation of wake center is large. When the wind direction becomes more constant, the wake center becomes stationary with a constant 10 m deviation from the rotor axis for about 2 hours. Then the wake center starts to fluctuate again as a result of the changing wind direction. It is worth noting that the wake center locations shown in

Figure 5-12 are relative to the rotor axis of WT2 that is assumed to be parallel to the wind direction. If the wind direction is incorrect or there is a yaw error, the orientation of the rotor axis will be wrongly determined, and consequently the deviation of the wake center from the rotor axis shown in Figure 5-12 will be erroneous. The absolute wake center locations in the Galion-based coordinates system ( $x', y'$ ) are plotted in Figure 5-13 for the first two hours of the wake2 period. The wake center moves as the wind direction changes (shifting from left to right in Figure 5-13) and the wake center only varies within 10 m when the wind direction stabilizes (see upper right corner in Figure 5-13). There is always an offset between the wake center and the wind direction or the rotor axis, indicating possible wind direction errors or wind turbine yaw errors. However, neither of these errors can be verified without the operational data of WT2.

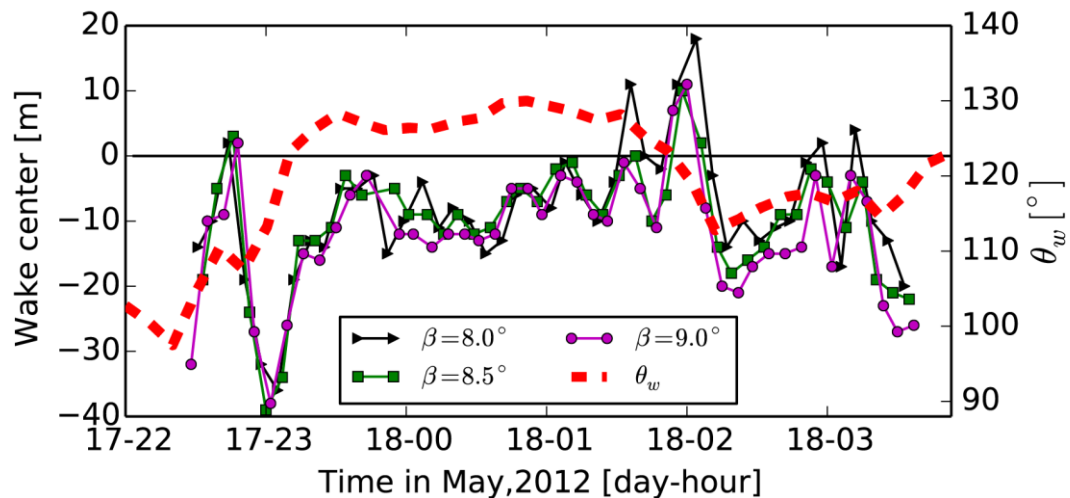


Figure 5-12 Time series of the estimated wake center during the wake2 period from PPI stacks with elevation angle  $8.0^\circ$ ,  $8.5^\circ$  and  $9.5^\circ$ , respectively. The dashed red line is the time series of wind direction.

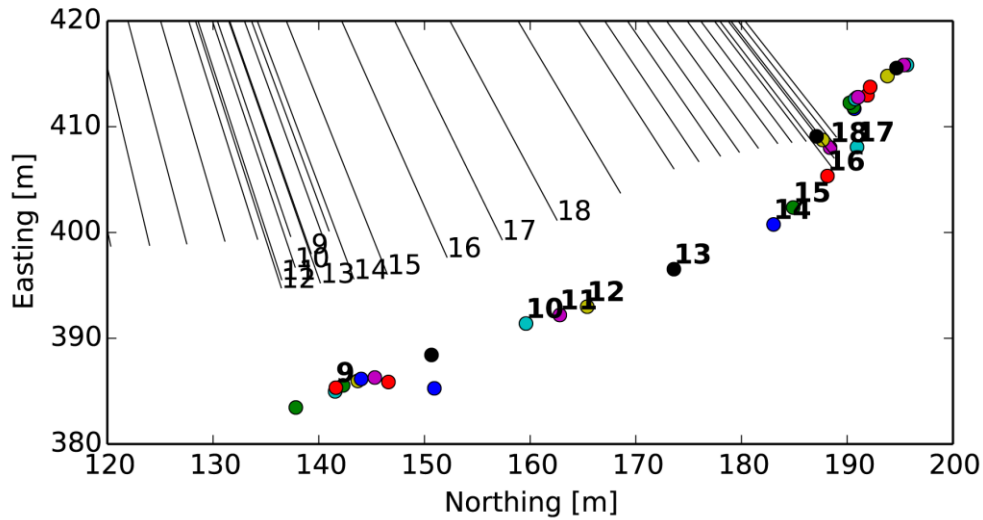


Figure 5-13 Locations of wake centers (circles) and wind directions (lines) observed between 22:40 and 23:59 on May 17, 2012 local time. The numbers denotes the time sequence of the wake centers and wind directions.

## 5.6 Conclusions

This paper presents the results from an experiment designed to measure wakes of a continuously yawing wind turbine with a ground-based coherent Doppler wind lidar in a large wind farm. Three-stack PPI scans are used. Radial velocities from the lidar are converted to wind speeds using the concurrent wind direction measurements from a meteorological mast. By assuming no yaw error of the wind turbine, wake profiles are estimated for every  $0.2D$  downwind of the wind turbine using a weighted averaging method. Wake statistics such as wake deficit, wake width and wake center are then automatically detected from the wake profiles. Consistent with previous observations, the wake deficit decreases and the wake width increases with increasing downwind distance. The location of the wake center shows no variation with downwind distance, but its movement with changing wind direction is observed.

While the lidar measurements from PPI scans can be used to automatically detect wakes from multiple directions, care must be taken with regards to the height variation over the conical surface. Depending on the wind direction or wind turbine orientation, the derived wake statistics can be contaminated by wind shear and become difficult to interpret. Hence, future work needs to seek the possibility of accounting for the height variation by incorporating three dimensional wake properties in wake profile estimate and provide practical guidelines for designing PPI scans for lidar wake measurements.

## CHAPTER 6 SUMMARY AND FUTURE WORK

### 6.1 Summary

Wind measurements with Doppler lidar are realized with measurement techniques consisting of scanning geometries and wind retrieval algorithms, both of which, in combination with atmospheric turbulence, cause errors in lidar-measured wind velocities. To facilitate the use of lidar for wind energy applications that require high accuracy and uncertainty quantification, this research consists of (i) using a field experiment to elaborate the strengths and limitations of lidar arc scans for mean wind speed measurements, (ii) developing a model to quantify and minimize the uncertainty of lidar arc scans through scanning geometry optimization, (iii) evaluating the dependence of errors of radial velocity variance estimates on sampling strategies, atmospheric turbulence properties and lidar design parameters, and (iv) conducting a field experiment to test the suitability of lidars for automatic wake detection and characterization of a continuously yawing wind turbine using PPI scans. The findings in this dissertation, while subject to limits and caveats, are consistent with theories and observations. Thus this work will have great utility for a priori optimization of lidar measurement strategies for wind energy applications.

The suitability of lidar arc scans for wind energy applications was studied using data collected from several field experiments. The retrieved wind velocities from arc scans generally agreed well with the concurrent sonic anemometer measurements, but had large errors when spatial gradients were present in the wind field. The results from the experiment suggest that (i) the uncertainty in the retrieved wind speed is related to

atmospheric turbulence, scanning geometries and retrieval algorithms, (ii) the uncertainty could be quantified using the weighted least squares method and the measured radial velocity variance, and (iii) a minimum  $30^\circ$  arc span is required to retrieve meaningful mean wind speed from the turbulent wind field. To stabilize the wind velocity retrieval algorithm, the vertical wind speed must be neglected. Thus, it is recommended that the mean radial velocity should be used to estimate the mean wind speed because the zero mean vertical wind speed is commonly a valid assumption.

A method was developed to quantify the dependence of the uncertainty of the wind speed retrieved from lidar arc scans on atmospheric turbulence properties and scanning geometries. The method is based on the isotropic turbulence model with the assumptions of frozen turbulence and horizontally homogeneous and stationary wind field. Error predictions from the method were verified with wind speeds retrieved from arc scans with different scanning geometries at three sites. Both the predictions and observations consistently showed that (i) the uncertainty was proportional to turbulence intensity, (ii) the uncertainty was reduced by aligning the line of sight with the wind direction, increasing arc span and decreasing beam number, (iii) the uncertainty was highest and most sensitive to the scanning geometry when the angle between the wind direction and the center line of sight of arc scan was  $45^\circ$ , and (iv) the lowest uncertainty was achieved with the full-azimuth conical scan. For wind resource assessment, the uncertainty in annual wind energy production prediction arising from the uncertainty in arc scan velocity retrieval is negligible.

Radial velocity variance estimates, which are necessary for obtaining accurate turbulence measurements from lidars, contain errors related to the autocorrelation

function of the volumetrically averaged radial velocity, sampling rate and sampling duration. Using both statistically simulated and observational data, it was demonstrated that the volumetric averaging increased the autocorrelation of radial velocities and therefore increased the errors in radial velocity variance estimates. The sampling rate has little effect on the errors when it is lower than the integral time scale. The errors have weak dependence on the orientation of the line of sight. The most effective error reduction strategy is to increase the sampling duration. Given that the sampling duration for which stationarity can reasonably be asserted (0.5–1.0 hour) in the atmospheric boundary layer, it was shown both theoretically and empirically that the systematic error can be much lower than 1%, but reducing the standard deviation of random errors to less than 8% is difficult with current lidar designs. These errors will propagate through to estimation of turbulence statistics from lidar measurements and fundamentally limit the accuracy of turbulence statistics derived from radial velocity variance estimates.

The last part of this dissertation presented the suitability and uncertainty of using PPI scans for wind turbine wake characterization via a field experiment designed to measure wakes of a continuously yawing wind turbine. Wake characteristics such as wake center, deficit and width were successfully retrieved from the lidar measurements and consistent with the previous observations. However, because the orientation of the wake changed with wind direction and wind turbine orientation, the locations of lidar measurements relative to the wake were not fixed. As a result, large wind shear caused large errors in the derived wake characteristics. Wake characteristics cannot be retrieved when laser beams are orthogonal to the wind direction or when the wake moves out of the scan domain. These limitations need to be accounted for when designing PPI

scans for lidar wake measurements and suggest that there is a need to develop a three-dimensional wake-tracking scanning strategy for lidar wake measurements.

Through detailed assessment of uncertainties and limitations of using lidars in mean wind speed measurements, turbulence statistic retrieval and wind turbine wake characterization, this dissertation has added knowledge that can facilitate lidar applications in wind energy. The findings will be beneficial for experimental design and error quantification of lidar measurements and can be used as the basis for future lidar design improvement.

## **6.2 Future work**

While this dissertation has made contributions to three aspects of lidar applications in wind measurements, it only addresses a few of the issues related to lidar wind measurements and the methods developed for error reduction is limited to specific conditions (e.g., neutral conditions in the atmospheric boundary layer or conditions under which the frozen turbulence assumption is valid). Future work is needed to extend the current work and should focus on the following areas.

### **6.2.1 Lidar turbulence measurements**

Studies have shown that lidars can provide vertical profiles of turbulence statistics over a deep layer in the atmosphere by (i) estimating radial velocity variance from lidar measurements from conical scans, (ii) correcting the averaging effect of lidar measurements in the estimated radial velocity variance and (iii) retrieving the six components of the velocity covariance matrix. Errors are introduced in each of the three steps. While results from this dissertation (see CHAPTER 4) can be used to predict and reduce the error in the first step, they also suggest several lines that should be pursued

in the future to reduce the errors in the second and third step. Correcting for the averaging effect in the second step is the biggest challenge for lidar turbulence measurements because this requires knowledge of the 3-dimensional turbulence structure that depends on varying atmospheric conditions. In this dissertation, it was found that the autocorrelation function based on the isotropic turbulence model could approximate the observed autocorrelation function with a fitted turbulence integral length scale. If this finding can be justified and verified in future work, it can greatly improve the accuracy of lidar turbulence measurements, particularly if the turbulence length scale model can be extended to non-neutral stabilities. This dissertation also shows that the errors in the estimated radial velocity variance are not sensitive to the sampling interval. This suggests the use of a high number of the sample locations at each height (without increasing the errors in the estimated variance). For example, dual conical scans (with two different elevation angles) with each conical scan providing six samples can be tested in future work. This scanning geometry (estimated solutions considering errors in observations) is better than the six-beam method (exact solutions from noisy observations) in terms of the inverse process.

### **6.2.2 Wind turbine wake characterization**

Lidars have opened up an opportunity for full scale wake observations under realistic atmospheric conditions as demonstrated in this dissertation (CHAPTER 5) as well as in the other studies. However, there is no consensus on lidar wake characterizations and there is a need for extensive research on scanning geometry optimization, wake characteristic retrieval and uncertainty quantification. Priority should be given to uncertainty quantification because it is needed to determine the goodness of a scanning

geometry or a retrieval algorithm. Uncertainty quantification in general is an established discipline with a large number of methods. Future work can test the applicability of these methods to quantify uncertainties in the wake characteristics retrieved from lidar measurements.

## BIBLIOGRAPHY

- Ahn, S., and J. A. Fessler, 2003: Standard errors of mean, variance, and standard deviation estimators. Last accessed: February 17, 2016. [URL: <http://ai.eecs.umich.edu/~fessler/papers/files/tr/stderr.pdf>.]
- Aitken, M. L., R. M. Banta, Y. L. Pichugina, and J. K. Lundquist, 2014: Quantifying Wind Turbine Wake Characteristics from Scanning Remote Sensor Data, *Journal of Atmospheric and Oceanic Technology*, **31**, 765-787. doi: 10.1175/JTECH-D-13-00104.1
- Aitken, M. L., and J. K. Lundquist, 2014: Utility-Scale Wind Turbine Wake Characterization Using Nacelle-Based Long-Range Scanning Lidar, *Journal of Atmospheric and Oceanic Technology*, **31**, 1529-1539. doi: 10.1175/JTECH-D-13-00218.1
- Banakh, V. A., I. N. Smalikho, F. Köpp, and C. Werner, 1995: Representativeness of wind measurements with a cw Doppler lidar in the atmospheric boundary layer, *Applied Optics*, **34**, 2055-2067. doi: 10.1364/AO.34.002055
- Banta, R. M., R. K. Newsom, J. K. Lundquist, Y. L. Pichugina, R. L. Coulter, and L. Mahrt, 2002: Nocturnal Low-Level Jet Characteristics Over Kansas During Cases-99, *Boundary-Layer Meteorology*, **105**, 221-252. doi: 10.1023/A:1019992330866
- Banta, R. M., L. S. Darby, J. D. Fast, J. O. Pinto, C. D. Whiteman, W. J. Shaw, and B. W. Orr, 2004: Nocturnal Low-Level Jet in a Mountain Basin Complex. Part I: Evolution and Effects on Local Flows, *Journal of Applied Meteorology and Climatology*, **43**, 1348-1365. doi: 10.1175/JAM2142.1
- Banta, R. M., Y. L. Pichugina, and W. A. Brewer, 2006: Turbulent velocity-variance profiles in the stable boundary layer generated by a nocturnal low-level jet, *Journal of the Atmospheric Sciences*, **63**, 2700-2719. doi: 10.1175/JAS3776.1
- Banta, R. M., Y. L. Pichugina, N. D. Kelley, B. Jonkman, and W. A. Brewer, 2008: Doppler lidar measurements of the great plains low-level jet: applications to wind energy, *IOP Conference Series: Earth and Environmental Science*, **1**, 12-20. doi: 10.1088/1755-1315/1/1/012020.
- Banta, R. M., Y. L. Pichugina, N. D. Kelley, R. M. Hardesty, and W. A. Brewer, 2013: Wind energy meteorology: insight into wind properties in the turbine-rotor layer of the atmosphere from high-resolution Doppler Lidar, *Bulletin of the American Meteorological Society*, **94**, 883-902. doi: 10.1175/Bams-D-11-00057.1
- Barthelmie, R. J., and Coauthors, 2005: Ten Years of Meteorological Measurements for Offshore Wind Farms, *Journal of Solar Energy Engineering*, **127**, 170-176. doi: 10.1115/1.1850489
- Barthelmie, R. J., and Coauthors, 2006: Comparison of wake model simulations with offshore wind turbine wake profiles measured by sodar, *Journal of Atmospheric and Oceanic Technology*, **23(7)**, 888-901. doi:
- Barthelmie, R. J., and Coauthors, 2009: Modelling and measuring flow and wind turbine wakes in large wind farms offshore, *Wind Energy*, **12**, 431-444. doi: 10.1002/we.348
- Barthelmie, R. J., and Coauthors, 2014: 3D wind and turbulence characteristics of the

- atmospheric boundary-layer, *Bulletin of the American Meteorological Society*, **95**, 743–756. doi: 10.1175/bams-d-12-00111.1
- Barthelmie, R. J., and S. C. Pryor, 2014: Potential contribution of wind energy to climate change mitigation, *Nature Climate Change*, **4**, 684-688. doi: 10.1038/nclimate2269
- Barthelmie, R. J., H. Wang, P. Doubrawa, G. Giroux, and S. C. Pryor, 2016: Effects of an escarpment on flow parameters of relevance to wind turbines, *Wind Energy*. doi: 10.1002/we.1980
- Bilbro, J. W., 1980: Atmospheric Laser Doppler Velocimetry: An Overview, *Optical Engineering*, **19**, 194533-194533-. doi: 10.1117/12.7972554
- Bingöl, F., J. Mann, and D. Foussekis, 2009: Conically scanning lidar error in complex terrain, *Meteorologische Zeitschrift*, **18**, 189-195. doi: 10.1127/0941-2948/2009/0368
- Bingöl, F., J. Mann, and G. C. Larsen, 2010: Light detection and ranging measurements of wake dynamics part I: one-dimensional scanning, *Wind Energy*, **13**, 51-61. doi: 10.1002/we.352
- Blackadar, A. K., 1962: The vertical distribution of wind and turbulent exchange in a neutral atmosphere, *Journal of Geophysical Research*, **67**, 3095-3102. doi: 10.1029/JZ067i008p03095
- Box, G. E. P., G. M. Jenkins, and G. C. Reinsel, 2008: *Time series analysis : forecasting and control*. John Wiley & Sons, pp. 746. ISBN: 9781118619193
- Bradley, S., 2007: *Atmospheric acoustic remote sensing: principles and applications*. CRC Press, pp. 296. ISBN: 1-4200-0528-6
- Branlard, E., and Coauthors, 2013: Retrieving wind statistics from average spectrum of continuous-wave lidar, *Atmospheric Measurement Techniques*, **6**, 1673-1683. doi: 10.5194/amt-6-1673-2013
- Browning, K. A., and R. Wexler, 1968: The Determination of Kinematic Properties of a Wind Field Using Doppler Radar, *Journal of Applied Meteorology and Climatology*, **7**, 105-113. doi: 10.1175/1520-0450(1968)007<0105:TDOKPO>2.0.CO;2
- Burton, T., D. Sharpe, N. Jenkins, and E. Bossanyi, 2011: *Wind energy handbook*. John Wiley & Sons, pp. 20. ISBN: 978-0-470-69975-1
- Calhoun, R., R. Heap, M. Princevac, R. Newsom, H. Fernando, and D. Ligon, 2006: Virtual Towers Using Coherent Doppler Lidar during the Joint Urban 2003 Dispersion Experiment, *Journal of Applied Meteorology and Climatology*, **45**, 1116-1126. doi: 10.1175/JAM2391.1
- Chai, T., C.-L. Lin, and R. K. Newsom, 2004: Retrieval of Microscale Flow Structures from High-Resolution Doppler Lidar Data Using an Adjoint Model, *Journal of the Atmospheric Sciences*, **61**, 1500-1520. doi: 10.1175/1520-0469(2004)061<1500:ROMFSF>2.0.CO;2
- Choukulkar, A., R. Calhoun, B. Billings, and J. Doyle, 2012: Investigation of a complex nocturnal flow in Owens valley, California using coherent Doppler lidar, *Boundary-Layer Meteorology*, **144**, 359-378. doi:
- Clifton, A., D. Elliott, and M. Coutney, 2013a: Ground-Based Vertically Profiling Remote Sensing for Wind Resource Assessment, 43 pp. Last accessed: February

- 17, 2016. [URL: [https://www.ieawind.org/index\\_page\\_postings/RP/RP%2015\\_RemoteSensing\\_1stEd\\_8March2013.pdf](https://www.ieawind.org/index_page_postings/RP/RP%2015_RemoteSensing_1stEd_8March2013.pdf).]
- Clifton, A., S. Schreck, G. Scott, N. Kelley, and J. K. Lundquist, 2013b: Turbine Inflow Characterization at the National Wind Technology Center, *Journal of Solar Energy Engineering*, **135**, 031017-031017. doi: 10.1115/1.4024068
- Collier, C. G., and Coauthors, 2005: Dual-Doppler Lidar Measurements for Improving Dispersion Models, *Bulletin of the American Meteorological Society*, **86**, 825-838. doi: 10.1175/BAMS-86-6-825
- Courtney, M., and Coauthors, 2014: D4.06 Data Reports and Databases: Data on coastal and offshore wind measurements, 42 pp. Last accessed: [URL: <http://www.fp7-marinet.eu/public/docs/D4.06%20Data%20reports%20and%20databases.pdf>.]
- Daley, R., 1993: *Atmospheric data analysis*. Cambridge university press, pp. 472. ISBN: 0-521-45825-0
- Demmel, J., 1997: *Applied Numerical Linear Algebra*. pp. 416. ISBN: 978-0-89871-389-3
- Draxl, C., A. N. Hahmann, A. Peña, and G. Giebel, 2014: Evaluating winds and vertical wind shear from Weather Research and Forecasting model forecasts using seven planetary boundary layer schemes, *Wind Energy*, **17**, 39-55. doi: 10.1002/we.1555
- Drechsel, S., G. J. Mayr, M. Chong, M. Weissmann, A. Dörnbrack, and R. Calhoun, 2009: Three-Dimensional Wind Retrieval: Application of MUSCAT to Dual-Doppler Lidar, *Journal of Atmospheric and Oceanic Technology*, **26**, 635-646. doi: 10.1175/2008JTECHA1115.1
- Eberhard, W. L., R. E. Cupp, and K. R. Healy, 1989: Doppler Lidar Measurement of Profiles of Turbulence and Momentum Flux, *Journal of Atmospheric and Oceanic Technology*, **6**, 809-819. doi: 10.1175/1520-0426(1989)006<0809:DLMOPO>2.0.CO;2
- Emeis, S., K. Schäfer, and C. Münkel, 2008: Surface-based remote sensing of the mixing-layer height – a review, *Meteorologische Zeitschrift*, **17**, 621-630. doi: 10.1127/0941-2948/2008/0312
- Floors, R., C. L. Vincent, S. E. Gryning, A. Peña, and E. Batchvarova, 2013: The Wind Profile in the Coastal Boundary Layer: Wind Lidar Measurements and Numerical Modelling, *Boundary-Layer Meteorology*, **147**, 469-491. doi: 10.1007/s10546-012-9791-9
- Foken, T., and B. Wichura, 1996: Tools for quality assessment of surface-based flux measurements, *Agricultural and Forest Meteorology*, **78**, 83-105. doi: 10.1016/0168-1923(95)02248-1
- Forbes, C., M. Evans, N. Hastings, and B. Peacock, 2011: *Statistical distributions*. John Wiley & Sons, pp. ISBN: 978-0-470-39063-4
- Frehlich, R., and M. Yadlowsky, 1994: Performance of mean-frequency estimators for Doppler radar and lidar, *Journal of Atmospheric and Oceanic Technology*, **11**, 1217-1230. doi: 10.1175/1520-0426(1994)011<1217:POMFEF>2.0.CO;2
- Frehlich, R., 1997: Effects of wind turbulence on coherent Doppler lidar performance,

- Journal of Atmospheric and Oceanic Technology*, **14**, 54-75. doi:
- Frehlich, R., S. Hannon, and S. Henderson, 1998: Coherent Doppler Lidar Measurements of Wind Field Statistics, *Boundary-Layer Meteorology*, **86**, 233-256. doi: 10.1023/A:1000676021745
- Frehlich, R., 2001: Estimation of velocity error for Doppler lidar measurements, *Journal of Atmospheric and Oceanic Technology*, **18**, 1628-1639. doi: dx.doi.org/10.1175/1520-0426(2001)018<1628:EOVEFD>2.0.CO;2
- Frehlich, R., and L. Cornman, 2002: Estimating Spatial Velocity Statistics with Coherent Doppler Lidar, *Journal of Atmospheric and Oceanic Technology*, **19**, 355-366. doi: 10.1175/1520-0426-19.3.355
- Frehlich, R., Y. Meillier, M. L. Jensen, B. Balsley, and R. Sharman, 2006: Measurements of Boundary Layer Profiles in an Urban Environment, *Journal of Applied Meteorology and Climatology*, **45**, 821-837. doi: 10.1175/JAM2368.1
- Gal-Chen, T., M. Xu, and W. L. Eberhard, 1992: Estimations of atmospheric boundary layer fluxes and other turbulence parameters from Doppler lidar data, *Journal of Geophysical Research: Atmospheres*, **97**, 18409-18423. doi: 10.1029/91JD03174
- Gottschall, J., M. S. Courtney, R. Wagner, H. E. Jørgensen, and I. Antoniou, 2012: Lidar profilers in the context of wind energy—a verification procedure for traceable measurements, *Wind Energy*, **15**, 147-159. doi: 10.1002/we.518
- Gottschall, J., G. Wolken-Möhlmann, T. Viergutz, and B. Lange, 2014: Results and Conclusions of a Floating-lidar Offshore Test, *Energy Procedia*, **53**, 156-161. doi: <http://dx.doi.org/10.1016/j.egypro.2014.07.224>
- Hardesty, R. M., W. A. Brewer, and B. J. Rye, 1997: Estimation of wind velocity and backscatter signal intensity from Doppler lidar returns. *Conference Record of the Thirty-First Asilomar Conference on Signals, Systems & Computers, 1997*, 269-273 vol.261.
- Hasager, C. B., D. Stein, M. Courtney, A. Peña, T. Mikkelsen, M. Stickland, and A. Oldroyd, 2013: Hub Height Ocean Winds over the North Sea Observed by the NORSEWinD Lidar Array: Measuring Techniques, Quality Control and Data Management, *Remote Sensing*, **5**, 4280-4303. doi: 10.3390/rs5094280
- Henke, M., and P. Clive, 2015: Robust low cost offshore power curve tests with LiDAR. *EWEA Offshore 2015*, Copenhagen, Denmark.
- Hirth, B. D., J. L. Schroeder, W. S. Gunter, and J. G. Guynes, 2015: Coupling Doppler radar-derived wind maps with operational turbine data to document wind farm complex flows, *Wind Energy*, **18**, 529-540. doi: 10.1002/we.1701
- Hoaglin, D. C., F. Mosteller, and J. W. Tukey, 1983: *Understanding robust and exploratory data analysis*. Vol. 3, New York [etc.] : Wiley, pp. 477. ISBN: 0471097772
- Horányi, A., C. Cardinali, M. Rennie, and L. Isaksen, 2015: The assimilation of horizontal line-of-sight wind information into the ECMWF data assimilation and forecasting system. Part I: The assessment of wind impact, *Quarterly Journal of the Royal Meteorological Society*, **141**, 1223-1232. doi: 10.1002/qj.2430
- IEC, 2005a: IEC 61400-12-1: 2005 Wind turbines - Part 12-1: Power performance measurements of electricity producing wind turbines. 90.

- , 2005b: IEC 61400-1: Wind turbines part 1: Design requirements. *International Electrotechnical Commission*, 177.
- Iungo, G. V., Y.-T. Wu, and F. Porté-Agel, 2013: Field Measurements of Wind Turbine Wakes with Lidars, *Journal of Atmospheric and Oceanic Technology*, **30**, 274-287. doi: 10.1175/JTECH-D-12-00051.1
- Iungo, G. V., and F. Porté-Agel, 2014: Volumetric Lidar Scanning of Wind Turbine Wakes under Convective and Neutral Atmospheric Stability Regimes, *Journal of Atmospheric and Oceanic Technology*, **31**, 2035-2048. doi: 10.1175/JTECH-D-13-00252.1
- Kelley, N. D., B. J. Jonkman, G. N. Scott, and Y. L. Pichugina, 2007: Comparing pulsed doppler LIDAR with SODAR and direct measurements for wind assessment. *AWEA WindPower Conference*, Los Angeles, California.
- Kettle, A. J., 2014: Unexpected vertical wind speed profiles in the boundary layer over the southern North Sea, *Journal of Wind Engineering and Industrial Aerodynamics*, **134**, 149-162. doi: 10.1016/j.jweia.2014.07.012
- Köpp, F., S. Rahm, and I. Smalikho, 2004: Characterization of Aircraft Wake Vortices by 2- $\mu$ m Pulsed Doppler Lidar, *Journal of Atmospheric and Oceanic Technology*, **21**, 194-206. doi: 10.1175/1520-0426(2004)021<0194:COAWVB>2.0.CO;2
- Krishnamurthy, R., R. Calhoun, B. Billings, and J. Doyle, 2011: Wind turbulence estimates in a valley by coherent Doppler lidar, *Meteorological Applications*, **18**, 361-371. doi: 10.1002/met.263
- Krishnamurthy, R., A. Choukulkar, R. Calhoun, J. Fine, A. Oliver, and K. S. Barr, 2013: Coherent Doppler lidar for wind farm characterization, *Wind Energy*, **16**, 189-206. doi: 10.1002/we.539
- Kristensen, L., P. Kirkegaard, and T. Mikkelsen, 2011: Determining the Velocity Fine Structure by a Laser Anemometer with Fixed Orientation Risø-R-1762(EN). Last accessed: February 17, 2016. [URL: <http://orbit.dtu.dk/files/5712483/ris-r-1762.pdf>.]
- Larsén, X. G., S. E. Larsen, and E. L. Petersen, 2016: Full-Scale Spectrum of Boundary-Layer Winds, *Boundary-Layer Meteorology*, 1-23. doi: 10.1007/s10546-016-0129-x
- Lenschow, D. H., J. Mann, and L. Kristensen, 1994: How Long Is Long Enough When Measuring Fluxes and Other Turbulence Statistics?, *Journal of Atmospheric and Oceanic Technology*, **11**, 661-673. doi: 10.1175/1520-0426(1994)011<0661:HLILEW>2.0.CO;2
- Lindelöw, P., M. Courtney, R. Parmentier, and J. P. Cariou, 2008: Wind shear proportional errors in the horizontal wind speed sensed by focused, range gated lidars, *IOP Conference Series: Earth and Environmental Science*, **1**, 012023. doi:
- Lindelöw, P. J. P., 2009: UpWind D1. Uncertainties in wind assessment with LIDAR Risø-R-1681. Last accessed: January 24, 2015. [URL: [http://orbit.dtu.dk/fedora/objects/orbit:82842/datastreams/file\\_5113517/content](http://orbit.dtu.dk/fedora/objects/orbit:82842/datastreams/file_5113517/content).]
- Lothon, M., D. Lenschow, and S. Mayor, 2006: Coherence and Scale of Vertical

- Velocity in the Convective Boundary Layer from a Doppler Lidar, *Boundary-Layer Meteorology*, **121**, 521-536. doi: 10.1007/s10546-006-9077-1
- Lyons, L., 1991: *A Practical Guide to Data Analysis for Physical Science Students*. Cambridge University Press, pp. ISBN: 9781139170321
- Mann, J., S. Ott, B. H. Jørgensen, and H. P. Frank, 2002: WAsP engineering 2000. Report 87-550-3094-7. Last accessed: [URL:
- Mann, J., and Coauthors, 2008: Comparison of 3D turbulence measurements using three staring wind lidars and a sonic anemometer. *IOP Conference Series: Earth and Environmental Science*, IOP Publishing, 012012.
- Mann, J., A. Peña, F. Bingöl, R. Wagner, and M. S. Courtney, 2010: Lidar Scanning of Momentum Flux in and above the Atmospheric Surface Layer, *Journal of Atmospheric and Oceanic Technology*, **27**, 959-976. doi: 10.1175/2010JTECHA1389.1
- Menzies, R. T., and R. M. Hardesty, 1989: Coherent Doppler lidar for measurements of wind fields, *Proceedings of the IEEE*, **77**, 449-462. doi:
- Monin, A. S., and A. M. Yaglom, 1965: *Statistical hydromechanics*. Nauka, pp. ISBN:
- Myers, R. H., 1990: Classical and modern regression with applications, *Duxbury advanced series in statistics and decision sciences Show all parts in this series*, 488. doi:
- Neiman, P. J., R. M. Hardesty, M. A. Shapiro, and R. E. Cupp, 1988: Doppler Lidar Observations of a Downslope Windstorm, *Mon. Wea. Rev.*, **116**, 2265-2275. doi: 10.1175/1520-0493(1988)116<2265:DLOAD>2.0.CO;2
- Newman, J. F., P. M. Klein, S. Wharton, A. Sathe, T. A. Bonin, P. B. Chilson, and A. Muschinski, 2015: Evaluation of three lidar scanning strategies for turbulence measurements, *Atmospheric Measurement Techniques Discussion*, **8**, 12329-12381. doi: 10.5194/amtd-8-12329-2015
- Newsom, R. K., and R. M. Banta, 2003: Shear-Flow Instability in the Stable Nocturnal Boundary Layer as Observed by Doppler Lidar during CASES-99, *Journal of the Atmospheric Sciences*, **60**, 16-33. doi: 10.1175/1520-0469(2003)060<0016:SFIITS>2.0.CO;2
- Panofsky, H. A., and J. A. Dutton, 1984: *Atmospheric turbulence: models and methods for engineering applications*. John Wiley & Sons, pp. 389. ISBN: 0471057142
- Pearson, G. N., and C. G. Collier, 1999: A pulsed coherent CO<sub>2</sub> lidar for boundary-layer meteorology, *Quarterly Journal of the Royal Meteorological Society*, **125**, 2703-2721. doi: 10.1002/qj.49712555918
- Pedersen, F. T., J. Å. Dahlberg, and P. Busche, 2006: ACCUWIND-Classification of five cup anemometers according to IEC 61400-12-1No. 1556(EN), 2006. Last accessed: February 27, 2016. [URL: [http://orbit.dtu.dk/fedora/objects/orbit:88359/datastreams/file\\_7703253/content](http://orbit.dtu.dk/fedora/objects/orbit:88359/datastreams/file_7703253/content).]
- Peña, A., S.-E. Gryning, and C. B. Hasager, 2009a: Comparing mixing-length models of the diabatic wind profile over homogeneous terrain, *Theoretical and Applied Climatology*, **100**, 325-335. doi: 10.1007/s00704-009-0196-8
- Peña, A., C. B. Hasager, S. E. Gryning, M. Courtney, I. Antoniou, and T. Mikkelsen, 2009b: Offshore wind profiling using light detection and ranging measurements,

- Wind Energy*, **12**, 105-124. doi: 10.1002/we.283
- Peña, A., and Coauthors, 2015: Ten Years of Boundary-Layer and Wind-Power Meteorology at Høvsøre, Denmark, *Boundary-Layer Meteorology*, **158**, 1-26. doi: 10.1007/s10546-015-0079-8
- Pichugina, Y. L., and R. M. Banta, 2010: Stable Boundary Layer Depth from High-Resolution Measurements of the Mean Wind Profile, *Journal of Applied Meteorology and Climatology*, **49**, 20-35. doi: 10.1175/2009JAMC2168.1
- Pichugina, Y. L., R. M. Banta, W. A. Brewer, S. P. Sandberg, and R. M. Hardesty, 2012: Doppler lidar-based wind-profile measurement system for offshore wind-energy and other marine boundary layer applications, *Journal of Applied Meteorology and Climatology*, **51**, 327-349. doi: 10.1175/JAMC-D-11-040.1
- Politis, D. N., and J. P. Romano, 1994: The Stationary Bootstrap, *Journal of the American Statistical Association*, **89**, 1303-1313. doi: 10.2307/2290993
- Politis, D. N., and H. White, 2004: Automatic Block-Length Selection for the Dependent Bootstrap, *Econometric Reviews*, **23**, 53-70. doi: 10.1081/ETC-120028836
- Pope, S. B., 2000: *Turbulent Flows*. Cambridge University Press, pp. 806. ISBN: 978-0-521-59125-6
- Ralph, F. M., and P. J. Neiman, 1997: Lidar observations of a breaking mountain wave, *Geophysical research letters*, **24**, 663-666. doi: 10.1029/97GL00349
- Rebmann, C., O. Kolle, B. Heinesch, R. Queck, A. Ibrom, and M. Aubinet, 2012: Data Acquisition and Flux Calculations. *Eddy covariance a practical guide to measurement and data analysis*, M. Aubinet, T. Vesala, and D. Papale, Eds., Springer, 59-83.
- Rye, B. J., and R. M. Hardesty, 1997: Detection techniques for validating Doppler estimates in heterodyne lidar, *Applied optics*, **36**, 1940-1951. doi: 10.1364/AO.36.001940
- Sanz Rodrigo, J., F. Borbón Guillén, P. Gómez Arranz, M. S. Courtney, R. Wagner, and E. Dupont, 2013: Multi-site testing and evaluation of remote sensing instruments for wind energy applications, *Renewable Energy*, **53**, 200-210. doi: 10.1016/j.renene.2012.11.020
- Sathe, A., and J. Mann, 2012a: Turbulence measurements using six lidar beams. *16th International Symposium for the Advancement of Boundary-Layer Remote Sensing*, 302-305.
- , 2012b: Measurement of turbulence spectra using scanning pulsed wind lidars, *Journal of Geophysical Research: Atmospheres*, **117**, D01201. doi: 10.1029/2011JD016786
- Sathe, A., and J. Mann, 2013: A review of turbulence measurements using ground-based wind lidars, *Atmospheric Measurement Techniques*, **6**, 3147-3167. doi: 10.5194/amt-6-3147-2013
- Sathe, A., J. Mann, N. Vasiljevic, and G. Lea, 2015: A six-beam method to measure turbulence statistics using ground-based wind lidars, *Atmospheric Measurement Techniques*, **8**, 729-740. doi: 10.5194/amt-8-729-2015
- Schwiesow, R., P. Köpp, and C. Werner, 1985: Comparison of CW-lidar-measured wind values obtained by full conical scan, conical sector scan and two-point

- techniques, *Journal of Atmospheric and Oceanic Technology*, **2**, 3-14. doi: 10.1175/1520-0426(1985)002<0003:COCLMW>2.0.CO;2
- Seibert, P., F. Beyrich, S.-E. Gryning, S. Joffre, A. Rasmussen, and P. Tercier, 2000: Review and intercomparison of operational methods for the determination of the mixing height, *Atmospheric environment*, **34**, 1001-1027. doi: 10.1016/S1352-2310(99)00349-0
- Sempreviva, A. M., R. J. Barthelmie, and S. C. Pryor, 2009: Review of Methodologies for Offshore Wind Resource Assessment in European Seas, *Surv Geophys*, **29**, 471-497. doi: 10.1007/s10712-008-9050-2
- Simley, E., L. Y. Pao, R. Frehlich, B. Jonkman, and N. Kelley, 2014: Analysis of light detection and ranging wind speed measurements for wind turbine control, *Wind Energy*, **17**, 413-433. doi: 10.1002/we.1584
- Simley, E., N. Angelou, T. Mikkelsen, M. Sjöholm, J. Mann, and L. Y. Pao, 2016: Characterization of wind velocities in the upstream induction zone of a wind turbine using scanning continuous-wave lidars, *Journal of Renewable and Sustainable Energy*, **8**, 013301. doi: 10.1063/1.4940025
- Smith, D. A., M. Harris, A. S. Coffey, T. Mikkelsen, H. E. Jørgensen, J. Mann, and R. Danielian, 2006: Wind lidar evaluation at the Danish wind test site in Høvsøre, *Wind Energy*, **9**, 87-93. doi: 10.1002/we.193
- Stawiarski, C., K. Träumner, C. Knigge, and R. Calhoun, 2013: Scopes and Challenges of Dual-Doppler Lidar Wind Measurements—An Error Analysis, *Journal of Atmospheric and Oceanic Technology*, **30**, 2044-2062. doi: 10.1175/JTECH-D-12-00244.1
- Stull, R. B., 1988: *An introduction to boundary layer meteorology*. Vol. 13, Springer Science & Business Media, pp. 670. ISBN: 9789027727695
- Taylor, G. I., 1938: The spectrum of turbulence, *Proceedings of the Royal Society*, **164**, 476-490. doi: 10.1098/rspa.1938.0032
- Towers, P., and B. L. Jones, 2016: Real-time wind field reconstruction from LiDAR measurements using a dynamic wind model and state estimation, *Wind Energy*, **19**, 133-150. doi: 10.1002/we.1824
- TurbSim: NWTC Information Portal (TurbSim). [URL: <https://nwtc.nrel.gov/TurbSim>.]
- Wagner, R., M. Courtney, J. Gottschall, and P. Lindelöw-Marsden, 2011: Accounting for the speed shear in wind turbine power performance measurement, *Wind Energy*, **14**, 993-1004. doi: 10.1002/we.509
- Wagner, R., T. F. Pedersen, M. Courtney, I. Antoniou, S. Davoust, and R. Rivera, 2014: Power curve measurement with a nacelle mounted lidar, *Wind Energy*, **17**, 1441-1453. doi: 10.1002/we.1643
- Wang, H., R. Barthelmie, P. Crippa, P. Doubrawa, and S. Pryor, 2014: Profiles of Wind and Turbulence in the Coastal Atmospheric Boundary Layer of Lake Erie. *Journal of Physics: Conference Series*, IOP Publishing, 012117.
- Wang, H., and R. J. Barthelmie, 2015: Wind turbine wake detection with a single Doppler wind lidar, *Journal of Physics: Conference Series*, **625**, 012017. doi: 10.1088/1742-6596/625/1/012017
- Wang, H., R. J. Barthelmie, A. Clifton, and S. C. Pryor, 2015a: Wind Measurements

- from Arc Scans with Doppler Wind Lidar, *Journal of Atmospheric and Oceanic Technology*, **32**, 2024-2040. doi: 10.1175/JTECH-D-14-00059.1
- Wang, H., R. J. Barthelmie, S. C. Pryor, and G. Brown, 2015b: Lidar arc scan uncertainty reduction through scanning geometry optimization, *Atmospheric Measurement Techniques Discussion*, **8**, 10429-10471. doi: 10.5194/amtd-8-10429-2015
- Weissmann, M., A. Dörnbrack, and J. D. Doyle, 2009: Vorticity from Line-of-Sight Lidar Velocity Scans, *Journal of Atmospheric and Oceanic Technology*, **26**, 2683-2690. doi: 10.1175/2009JTECHA1260.1
- Werner, C., and Coauthors, 2001: Wind infrared Doppler lidar instrument, *Optical Engineering*, **40**, 115-125. doi: 10.1117/1.1335530
- Werner, C., 2005: Doppler Wind Lidar. *Lidar: Range-Resolved Optical Remote Sensing of the Atmosphere*, C. Weitkamp, Ed., Springer New York, 325-354.
- Wyngaard, J. C., 2010: *Turbulence in the Atmosphere*. Cambridge University Press, pp. 393. ISBN: 9780521887694